Design for Selective Remote Control of Cellular Signaling Using Magnetic Nanoparticles

by

Junsang Moon

Submitted to the Department of Materials Science and Engineering
in partial fulfillment of the requirements for the degree of

Ph. D. in Materials Science and Engineering

at the

MASSACHUSETTS INSTITUTE OF TECHNOLOGY

February 2021

Author . . . .
Department of Materials Science and Engineering
February 18, 2021

Certified by . . . .
Polina Anikeeva
Associate Professor
Thesis Supervisor

Accepted by . . . .
Frances M. Ross
Chair, Departmental Committee on Graduate Studies

Design for Selective Remote Control of Cellular Signaling Using Magnetic Nanoparticles

by

Junsang Moon

Submitted to the Department of Materials Science and Engineering
on February 18, 2021, in partial fulfillment of the
requirements for the degree of
Ph. D. in Materials Science and Engineering

Abstract

Understanding the structure and dynamics of the mammalian cellular signaling and the nervous system opens up the chances to induce tissues, organs, or organisms to function in a coordinated way. Consequently, extensive research and efforts have rapidly developed strategies for rationally manipulating cellular and neuronal signaling. In this thesis, I pursued to develop a wirelessly modulating system that can selectively control a targeted biological circuit. Heat dissipating properties of magnetic nanoparticles have garnered sustained research interest in biomedical applications, including drug release, cancer hyperthermia, and neural stimulations. However, research has been mainly focused on improving the magnetic nanomaterials' heat dissipation efficiency. To introduce selective heat dissipation of magnetic nanoparticles, I have designed a custom AC magnetometer that can capture dynamic magnetization of magnetic particles suspended in solution. The collected magnetic response data fed to an equation called multiplexing factor to find optimized alternative magnetic field conditions that can selectively trigger heat dissipation on each particle ensemble. This approach was confirmed by direct temperature change observation using a thermographic camera. The selective heating system was later combined with genetic engineering and a drug delivery system for selective cellular modulation. This work culminates in a demonstration of selective remote control of cellular signaling in vitro. The theoretical background, systematic design, and precisely executed demonstration can be transplanted to any system using magnetic nanoparticles as a heat transducer. Therefore, this study will set a strong foundation and suggest new approaches for researches utilizing magnetic nanoparticle's heat dissipation for any applications.

Thesis Supervisor: Polina Anikeeva
Title: Associate Professor

Acknowledgments

When I look back on my Ph.D. life, I feel myself is more like a collection of supports, care, kindness, and assistance from people around me. It is fortunate to meet these great people working together to bring a multidisciplinary project to the world. My years at MIT was a fantastic journey, and it wouldn't be possible without them.

First and foremost, I would like to thank my advisor, professor Polina Anikeeva. Polina was a passionate, diligent, and insightful person who shed light on and gave guidance to my research. She always looked for the best for her students. She was a person who I could truly respect. I genuinely feel grateful for all the support she gave to me. I cannot imagine myself managing Ph. D. work without joining her group. From the way she showed us, I learned how I should go about my life. I am thankful to my thesis committee members, professor Caroline Ross and professor Robert Macfarlane. They provided valuable insights and suggestions for my projects through committee meetings and helped me see my research from a new perspective.

I don't think I could have accomplished my work without the help of my labmates and collaborators. I appreciate Michael for sharing his prototyping skills and his more profound understanding of magnetics. I also want to thank Ritchie for teaching me chemistry in my first year. Siyuan has been a great collaborator and a great teacher to me at the same time. I want to thank Seongjun for being a great supporter in many ways. Thanks to you, I could have survived throughout those 5 years. It was also a pleasure for me to work together with Dekel for her fantastic work. I also want to say thank you to Pohan for teaching me bio works. Jimin has been a great friend of mine since my college and also an amazing collaborator over the years. I really appreciate your help. I also want to say to Florian and Youngbin that it was a great pleasure to work together. Again, George, thank you for teaching me the Mathematica for my research. Thank you, Atharva, for teaching me fiber polishing. Also, thank you, Alice and Alex, for being great office mates. It was really a pleasure for me to spend time with you. I also want to thank David and Colin for helping me prototyping with PCB. I don't think the work could be done without you.

I want to give my gratitude to the people I met at SNU. Thanks to Prof. Kitae Nam, Prof. Eunsoo Park, and Prof. Kisuk Kang, I could get the opportunity to study at MIT, meeting the bigger world. I also want to thank Sim Uk for teaching me lots of stuff working together. Thank you Kyungsuk and Jinwoo. I learned a lot from you, and even after I came to MIT, it was a great pleasure to meet you here again.

Li-Chen, you were the best accomplishment that I earned in this Boston. We already spent more than 5 years together, and those 5 years were full of pleasant memories. I don't think I can find any other person better than you. Thank you for being with me throughout this Ph. D. life. I promise that I will make you happy throughout your life. Let's make more unforgettable and joyful memories together.

Finally, I want to give my biggest love and gratitude to my parents, my sister's couple, kong, and our newborn Lee Gun. I could have managed all this work because no matter what happens to me, I knew that my family will always be there for me and provide me unconditional support and love. Thank you for having me born in this family.

Contents

Abbreviations

MNP: Magnetic nano particles

FEMM: Finite Element Method Magnetics

AMF: Alternating magnetic field

ACM: Alternating current magnetometer

VSM: Vibrating sample magnetometry

OAc: Oleic acid

PMAO: poly(maleic anhydride-alt-1-octadecene)

mPEG: Poly(ethylene glycol) methyl ether

PEI: Polyethylenimine

SLP: Specific loss power

TEM: Transmission electron microscope/microscopy/micrograph

TRPV1: Transient receptor potential vanilloid member 1

XRD: X-ray diffraction

Chapter 1

Introduction

1.1 Introduction

Understanding the structure and dynamics of the mammalian cellular signaling and the nervous system opens up the chances to induce tissues, organs ,or organisms to function in a coordinated way. Consequently, extensive research and efforts have rapidly developed strategies for rationally manipulating cellular and neuronal signaling. [1, 2, 3, 4] Some technologies are based on implantable medical devices. Advances in microelectronics and fabrication technologies enabled hierarchical, complex, and multi-functional design of the implants. [2, 4, 5] The hierarchical and multi-channeled implants have shown promising results in handling biological responses that require multiple inputs. [6, 7] Unfortunately, this implant-based strategy can hardly avoid criticism, saying it's still invasive, in that the whole or parts of implants should go into the target. [8] On the other hand, Nanotechnology, which deals with materials in one billionth of a meter scale, can offer minimally invasive, hardware-free approaches to control targets. [8, 1] Still, modulation strategies employing nanotechnology have confronted difficulties in selective and multiple input control and demonstrated digitized single input manipulation over the target. [?] This thesis focuses on developing of selective and multiplexed modulation of cellular signaling and nervous system using magnetic nano materials and will go through materials physics and chemistry, polymer engineering, electronic apparatus, and bio-engineering.

1.2 Initiation of Cellular signaling through receptor

Cells receive and process signals originated outside their boundaries to respond to alterations in their immediate environment. There are typically three stages in cell signaling: reception of the signal, transduction of the message through the cell, and the cellular response that has been evoked by the signal. [9] Cells have proteins called receptors that sense the external stimuli and initiate a physiological response. The reception of the signal initiates most cell signaling processes via these receptors on the cell surface. For this reason, the majority of technologies triggering specific biological responses such as pharmacology, optogenetics, chemogenetics, sonogenetics and magnetogenetics, target receptors to initiate the cascade of the process. [10]

Most receptors are generally transmembrane proteins, which capture signaling molecules outside the cell and subsequently transmit the signal to internal signaling pathways via molecular switches in sequence. Membrane receptors can be categorized into three major classes: G-protein-coupled receptors, ion channel receptors, and enzyme-linked receptors. The classification is based on how the receptors translate external signals into internal cues - via protein action, ion channel opening, or enzyme activation, respectively. Through the receptors transform external signals into internal ones, signaling molecules do not enter the cell's plasma membrane. [9]

Cell surface receptors receive and transduce signals in several ways. The signals are typically chemicals that bind to a receptor and initiate a cellular response. [10, 9] Some receptors, however, detect different stimuli such as temperature[11], mechanical displacement (touch, pressure, vibration, etc.)[12], pH change [13, 14] and light [15, 16]. This thesis also employed genetic modification to introduce several receptors to cells and neurons, which will initiate switches for the cascading signaling process and demonstrated the initiation of cellular/neuronal signaling process cued by magnetic nano-materials.

When a receptor receives a signal, it goes through a conformational change, which triggers sequential biochemical reactions. This signal transduction cascades amplify the message in most cases and produce multiple intracellular signals for receptors embedded within the cellular membrane. [9]

The relayed signal reaches final target protein and causes cellular response. The molecules that relay this cascade are often proteins. However, non-protein molecules such as calcium ions and phospholipids also play critical roles. It's because these non-protein molecules function as secondary messengers in several signal transduction pathways.[17, 18] Cellular morphogenetic activities such as proliferation, differentiation, cell motility, and metamorphosis are representative examples of this pathway. [19, 20]

Unlike cellular signaling, however, the transmission of a signal within a neuron initiated by a receptor propagates in a different way. Neurons convey the signal in terms of electrical potential across the membrane. In the resting stage, the intracellular is negatively charged to around - 70mV comparing to the extracellular. When this electrical potential is decreased below around -50mV by any factor called depolarization, it triggers the sodium channels to be opened and allow the influx of sodium cation. This sodium cation influx drives electrical potential across the membrane to be opposite, and it opens neighboring sodium channels, causing neuron's signaling - action potential.[9] Action potential is defined as a sudden, fast, transitory, and propagating change of the resting membrane potential. The influx of calcium ions can trigger this depolarisation with an appropriate gene modification and stimulus by increasing membrane potential over the threshold.[15, 16, 12, 2, 4]

1.3 Application of magnetic nanoparticles in biomedical applications

Recent advances in nanochemistry have demonstrated that nanoscale imaging probes and therapeutic agents can overcome the shortcomings of traditional diagnosis and therapy while minimizing the lack of specificity and associated side effects. [21, 22, 23]

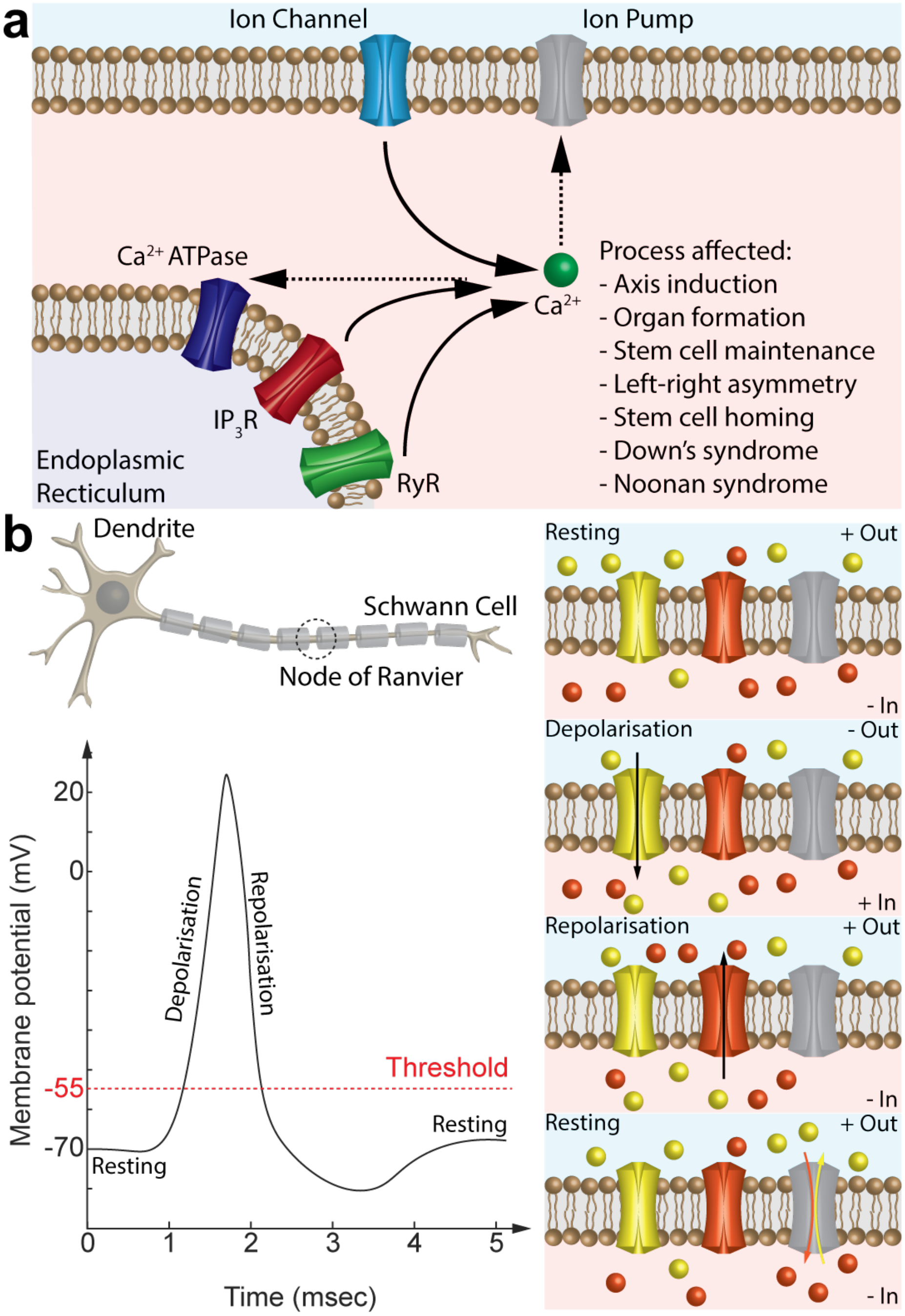

Figure 1-1: **Schematic explanation of cellular and neuronal signaling pathway through receptor** (a) An overview of calcium ion signaling pathways in non-excitable cells. (IP_3R: 1,4,5-trisphosphate sensitive Ca^2+ channel(Receptor), RyR: Ryanodine receptor) (b) Neurons transmit electrical signals called action potentials along the axial direction. It consists of 3 main phases; hyperpolarisation(resting), depolarisation, and repolarisation. (Right sub-figures) When the membrane potential within the cell goes higher than -55mV, an action potential initiates.

Among the many types of nano-materials, superparamagnetic iron oxide nanoparticles including ferrihydrite ($Fe_2O_3 \cdot 0.5H_2O$), magnetite (Fe_3O_4) and maghemite ($\gamma - Fe_2O_3$) have been extensively investigated for biomedical applications because of their benign, nontoxic and biodegradable nature. [23, 24] In addition to that, low magnetic susceptibility of biological matter allows that external magnetic fields can access magnetic composite hidden under arbitrarily deep tissues with little attenuation. In reverse, magnetic signals from magnetic nanoparticles can also penetrate the thick body and reach the detector. [25, 26] For these reasons, magnetic nanoparticles have garnered sustained research interest for their promise in biomedical applications, including diagnostic imaging, triggered drug release, cancer hyperthermia, and neural stimulation. [1, 2, 21, 22, 23, 27]

Researchers extensively studied iron oxides as a magnetic resonance imaging (MRI) agent. MRI detects magnetic resonance signals coming from the relaxation of protons inside tissues, and the relaxation time can be altered by the interaction with the nearby contrast agent. MRI contrast agents are paramagnetic materials that generate oscillating magnetic fields to provide the relaxation mechanisms to neighboring protons. Iron oxide nanoparticles are favored because they are expected to have low toxicity and subsequently incorporate into the body's iron pools and metabolic processes. Iron oxides also show enhanced MRI contrast performances when it's compared to conventional MRI agents.[22]

Iron oxide is also designed as stimuli-responsive magnetic nanoparticles. The stimuli-responsive MNP-based drug delivery system has been designed by introducing various surface ligands and polymeric coatings onto the iron oxide nanoparticles. These nano-composites can respond to several endogenous (e.g., pH, enzyme, and redox environments) stimuli and exogenous (e.g., light) stimuli through the incorporation of stimuli-responsive chemical or physical bonds.[22, 28, 29] However, some applications didn't stop at just relying on external stimuli to give the cue to the nano-composite. Magnetic nanoparticles intrinsically can generate mechanical forces or heat in the presence of magnetic fields, which can be a starting signal to stimuli-responsive nano-composite. These designs have been widely utilized for therapeutic researches, such as the precise release of drugs, gene delivery, and hyperthermic cancer treatment.[22, 29] In this thesis, I have focused on developing selective heat dissipation of iron oxide nanoparticles, which can potentially expand the design of stimuli-responsive nano-composites that make use of heat from magnetic nanoparticles as the cue.

1.4 Historical overview of approaches for multiple inputs

Cell signaling is a multifactorial system that is composed of signaling cascades. Therefore signaling interplay is inevitable, and the complexity in cellular signaling arises from the interaction or crosstalk between signaling pathways.[30] A human brain is composed of billions of neurons interwoven through trillions of connections, with each circuit having miscellaneous groups of firing properties, biochemical signals, and wiring patterns.[31] For these reasons, the biggest challenge in cellular signaling control and neuroscience was a specific control of circuits while leaving others untouched.

There was some progress made in the 20th century using pharmacological and electrophysiological approaches, but these methods couldn't isolate cellular signaling pathway or neural circuitry with sufficient precision.[32] However, starting from the late 1990s and early 2000s, genes that can specifically respond to specific stimuli were transferred into excitable animal cells in vitro, and eventually, neurons. In a pharmacological method, Designer Receptors Exclusively Activated by Designer Drugs (DREADD)-based chemogenetic tools enabled specificity in cellular signaling control and neuroscience. Engineered protein receptor was expressed on the cell/neuron via genetic transfection, and the receptor specifically responded only to certain chemicals.[33, 34] Likewise, the introduction of channelrhodopsin 2 (ChR2), a blue-light-activated cation channel, enabled cells/neurons to respond only to blue lights.[35] In addition to these, other multiple techniques have been developed to target specific cells/neurons using various stimuli, such as magnetic nanoparticles, magnetic nanodisks, ultrasound, ferritins e.t.c.[2, 4, 1]

1.5 Structure and Motivation of the Thesis

This thesis focuses on selective heating control of magnetic nanoparticles that are applicable to any other biomedical applications relying on magnetothermal stimuli from magnetic nanoparticles. To make the findings in this research understandable and accessible to people, chapters were written in the order of my research flow.

Chapter 1 intended to provide a general understanding and historical overview of topics that are closely related to the work presented in this thesis. Chapter 2 covers the contents of ferrite materials that have been used as heat transducers in the thesis. It includes theoretical and experimental details for understanding MNPs heat dissipation at given AMF environments and MNP's synthesis and phase transfer. Chapter 3 offers experimental techniques and electronic apparatus that are used to enable precise and selective heat dissipations of MNP ensembles. Chapter 4 introduced actual selective cellar signaling modulation using a multiplexed magnetothermal system and demonstrated using bulk heating. Chapter 5 also presents another selective cellular signaling system using a multiplexed magnetothermal system but by employing nano scale heating of MNPs and thermo-sensitive liposomes. Chapter 6 recapitulates the research results and concludes by offering a suggestion on magnetogenetics with the summaries of recent advances in magneto-neuromodulation techniques.

Recent advances in neuromodulation techniques have brought significant impacts on neuroscience and neurotheraphy as well. Voltage and current controlled electrical neural stimulation (ENS) have already been widely applied in both neuroscience and clinical practices for neuroprosthetics. Nevertheless, it has shown limited target specificity due to the spread of current from the electrodes.[36] However, recent studies combined with genetic engineering enabled the expression of ion channels and proteins to targeted cells/neurons, explicitly responding to certain types of stimuli. [35, 2, 4, 1] Optogenetics, which uses the light to control neurons that have been genetically engineered to express light-sensitive ion channels, have assisted neuroscience in turning on and off individual neurons. [15, 16] In the ENS field, a very recent research tried to minimized this spread of current to reduce the lack of specificity. Researchers approached this problem using in vivo polymerization of conductive polymers and achieved cell specificity through genetic engineering.[37] These are powerful technology but limited by the necessity to deliver light or electrical current to the cells of interests, which often requires invasive surgery and a tethered power source.

Magnetogenetics, which uses magnetic nano-materials such as magnetic nanoparticles, ferritin, or magnetic nano-composite, has become the spotlight. As magnetic fields driving the system can pass freely through organic tissue because of its negligible magnetic permeability, it requires minimally invasive surgery or tethering the target to the power source.[2, 4, 1] Additionally, recent publications showed demonstrations on how magnetothermal system can be adopted to withdraw biological responses from living organisms.[27, 38, 39]

However, as stated earlier in the introduction of biomedical applications using MNPs, these demonstrations also were limited to a digitized system - only heat on and off. This research and thesis intended to provide step-wise introduction for selective magnetothermal control. Also to affirm that this system is transferable to these wireless magnetic nanoparticle-mediated cellular/neuronal stimulation, biological applications have been demonstrated in two ways. The first way was that delivering heat directly to the TRPV1 channel expressed cells as a signaling cue. Its advantage is that it offers spatial and temporal selectivity to the target with few mm and few seconds precision. The second way was releasing drugs that trigger the activities of the hM3d(Gq) expressed cells. This approach does not just exhibit selective targeting of the tissue but also shows potential on/off modulation to the same target.

Chapter 2

Magnetic Nanoparticles as heat transducer

2.1 Structural and Magnetic Properties of Ferrite

Iron oxide magnetic nanoparticles have been employed due to their biocompatibility and manageable colloidal stability.[40] Spinel ferrites, which have the chemical composition $MO\dot{F}e_2O_3$, have a complex cubic unit cell composed of 2 different subunits. These subunits can be occupied by transition metal ions and sorted into two different subunits depending on their arrangement with oxygen ion. One population is tetrahedral (A) sites, and the other is octahedral (B) sites. There are 64 possible tetrahedral sites in one spinel unit cell, and among these, eight sites get occupied. Of the 32 possible octahedral sites, only 16 sites are occupied. This gives ferrite the formula unit $MO\dot{F}e_2O_3$.[41]

In ionic solids, 3d transition metal ions have super-exchange couplings through oxygen ions. This super-exchange interaction becomes more dominant as the bonding gets more collinear because the p orbitals of oxygen ions mediate the coupling. A-O-B bonding in the spinel structure has 125^o bonding angle and B-O-B has 90^o bonding angle. A-O-A bonding doesn't exist in the spinel structure. This oxygen mediated bonding drives transition metal ions in A and B sites to point to an antiparallel direction, giving ferrimagnetic properties to spinel ferrites..[41]

Spinel structures can be sorted into two different categories, normal spinel and inverse spinel structure. A sites are surrounded by 4 oxygen ions and B sites are surrounded by 6 oxygen ions. Considering charge neutrality, A sites should be occupied with 2+ cations, and B sites should be populated with 3+ cations. However each transition metal ion has its own site preference. For instance, Fe^{3+} has a stronger tendency to tetrahedral sites than the Fe^{2+} cation. This drives Fe^{3+} ions to go into A sites kicking out Fe^{2+} ions to B sites.[42] If 3+ cations occupy A sites then the structure is called inverse spinel, and if 2+ cations occupy A sites, then it is called normal spinel structure. This is also one of the factors which determines the intrinsic magnetic moment of the ferrite material.

Transition metal ions have certain site preference. This trend is determined by the factors like cation size, crystal field energy and valence. According to thermodynamic calculations and experimental observations, Zn^{2+} has the strong preference in

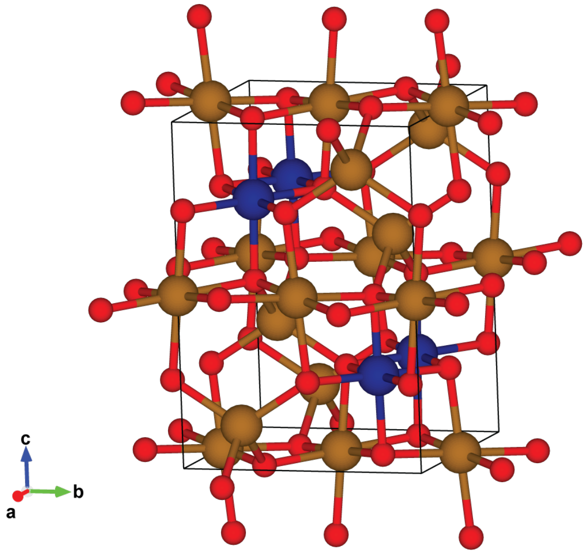

Figure 2-1: **Cobalt ferrite spinel crystal structure** tetrahedral sites (A - Yellow sphere, Iron) and octahedral sites (B - Navy sphere, Cobalt) for transition metal ions coordinated with oxygen (Red sphere)

tetrahedral sites (A sites) and Co^{2+} favors octahedral sites (B sites).[43, 42, 44] Zn^{2+} doesn't have any magnetic moment because its 3d orbitals are fully occupied. Thus Zn^{2+} in A sites of ferrite will reduce the magnetic moment from the A lattice that opposes the magnetic moment from B sites. Accordingly, doping magnetite with Zn^{2+} can be used to boost magnetic saturation of the material. On the other hand, Co^{2+} has 7 electrons in 3d-orbitals. The substitution of Fe^{2+} with Co^{2+} produces distortion of the lattice and breaks degeneracy resulting in a higher spin-orbit interaction. This, in turn, yields higher anisotropic energy to the Co-doped ferrite.[44]

Higher anistropic energy given by Co-doping can make wider coercive field, which enables larger hysteresis at its optimized field condition. Magnetic hyperthermia performance of magnetic ferrite nanoparticles is originated from the hysteric behavior during magnetization process and therefore, hyperthermic properties can be improved

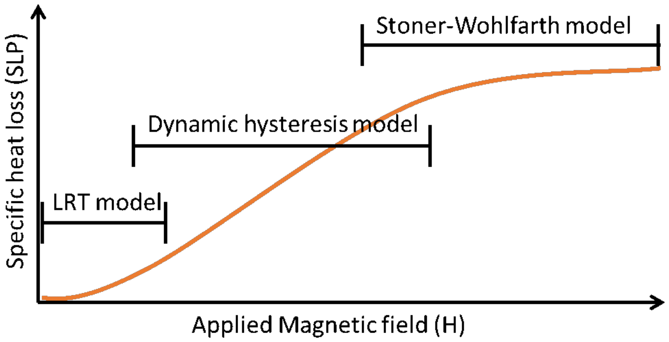

Figure 2-2: **A schematic graph of magnetic hyperthermia of single domain magnetic nanoparticles.** 3 different models are employed to explain hyperthermic behavior at different field conditions.

by Co incorporation into the lattice. This transition metal substitution (Iron to Cobalt) induced Jahn-Teller distortions to the lattice and this changed magnetocrystalline anisotropy in scale by an order.

2.2 Physical Theory for Specific Loss Powers(SLPs)

Specific loss power (SLP) is an intrinsic lost heat energy during magnetization process coming from hysteric characteristics of magnetic material. Heat dissipation (=magnetization process) of single domain magnetic nanoparticles cannot be understood only by using one theory. 3 different models - Linear response theory, the Stoner-Wohlfarth Model and dynamic hysteresis - explains magnetic nanoparticles behavior in different regime. These 3 models will be introduced in this section.

2.2.1 Linear Response Theory

Linear response theory (LRT) was first proposed by Rosensweig to explain theoretical power dissipation in magnetic fluids subjected to alternating magnetic fields.[45]

LRT tries to suggest dissipation relationships based on rotational relaxation of single domain magnetic particles dispersed in a liquid matrix. This model is more suitable for explaining magnetic particles with high coercive field, strongly anisotropic, single-domain state and superparamagnetism.[46] When the ferrofluid susceptibility is given as $\chi = \chi' - i\chi''$, this model approximates volumetric power dissipation per magnetization cycle as:

$$A = \Delta U = \mu_0 \pi \chi^{''} H_0^2 \qquad (H_0 - \text{applied field}) \tag{2.1}$$

which is equal to the area of the hysteresis loop. Specific loss powers (SLPs) of magnetic nanoparticles can be calculated by multiplying the energy loss per cycle of the magnetization process with the applied frequency. $(SLP = A * f)$ Magnetic susceptibility used in the above equation also changes along the frequency change of the magnetic field.

$$\chi^{''} = \frac{(\mu_0 M_s^2 V)}{(3k_B T)} \frac{(\omega \tau_R)}{((1 + \omega^2 \tau_R^2))} (\tau_R - \text{effective relaxation time, } \omega = 2\pi f) \tag{2.2}$$

The heat dissipation of magnetic nanoparticles for neuronal stimulation will be conducted in water, so Brownian and Néel processes will take place in parallel. The Néel process is the magnetization flip parallel to the field direction and Brownian process means physical rotation of magnetic particle toward the field direction. Neel and

Brownian mean transition times are

$$\tau_N = \tau_0 \exp(\frac{K_{eff}V}{k_B T}) \qquad (\tau_0 - \text{relaxation coefficient}) \tag{2.3}$$

$$(K_{eff} - \text{effective anisotropic energy, } V\text{-particle volume})$$

$$\tau_B = \frac{3\mu V_H}{k_B T} \quad (\mu - \text{viscosity, } V_H - \text{hydrodynamic volume}) \tag{2.4}$$

Therefore the effective relaxation time τ_R should be

$$\frac{1}{\tau_R} = \frac{1}{\tau_B} + \frac{1}{\tau_N} \tag{2.5}$$

Additionally, according to LRT, heat dissipation caused by eddy current is counted as negligible due to the small size of the particles (15nm).[45] LRT attempts to describe the response of the MNP ensemble using Néel-Brown relaxation under assumption that the magnetization of ferrofluid scales linearly with the amplitude of the applied field. LRT alone, however, cannot explain all hyperthermia experiments.[47, 48] If the applied field amplitude is higher than the coercivity of the MNPs, the number of MNPs aligned along the field will be saturated already, which means there will be no additional heat dissipation with increasing field amplitude. So in this case, LRT will overestimate SLP of the materials.

2.2.2 Stoner-Wolfarth Theory

When the applied field amplitude is higher than the coercive field of the MNPs, it exceeds the entire hysteresis loop and LRT is no longer valid. In this case, heat dissipation can be explained through the Stoner-Wohlfarth model. The original Stoner-Wohlfarth model does not take into account any thermal activation (T=0 K or when frequency f approaches infinity). Due to the ignorance of thermal activation, magnetization stays in one of the two minima of the energy. For MNPs aligned with their easy axis parallel to the field direction, the anisotropy barrier equals to $\mu_0 H_K$ and the hysteresis loop becomes a perfect square. In this case, the area of the hysteresis loop becomes maximum.

$$A = 4\mu_0 H_C M_s = 4\mu_0 H_K M_s = 8K_{eff}(\text{at } \Phi\text{=}0) \tag{2.6}$$

(Φ-angle between magnetic moment and easy axis)

(K_{eff}-effective anisotropic energy)

However, if all MNPs aligned with their easy axis orthogonal to the field direction, the magnetization process follows the hard axis and the hysteresis loop disappears, giving A=0. If the MNPs are arranged randomly distributed in 3D space, the corresponding coercivity is $0.482H_K$ and the area A reduces to $1.928K_{eff}$.[49]

There is also a model for when T is non-zero and field frequency is finite. The temperature dependence of coercivity varies depending on the angle between easy axis of the particles and the direction of applied field. For instance, if the field is parallel to easy axis, the coercivity drop is proportional to $\sqrt{T}$. Randomly distributed MNPs, however, show a decrease in coercivity with temperature, almost proportional to $T^{3/4}$.[50] Usov et al.[51] took another step on this. He proposed a new dimensionless parameter κ for the variation of the coercive field to take into account the field frequency. According to his model, the coercive field Hc is

$$\mu_0 H_C = \mu_0 H_K(1 - \kappa^{0.5}), \quad (\Phi{=}0) \tag{2.7}$$

$$\mu_0 H_C = 0.482\mu_0 H_K(1 - \kappa^{0.8\pm0.05}), \quad \text{(random orientation)} \tag{2.8}$$

With

$$\kappa = \frac{k_B T}{K_{eff} V} \ln\left(\frac{k_B T}{4\mu_0 H_{max} M_s V f \tau_0}\right) \quad (M_s\text{-magnetic saturation, } V\text{-particle volume}) \tag{2.9}$$

For random orientation case, Eq. (2.8) roughly matches up to κ=0.5.[46]

2.2.3 Dynamic Hysteresis

Dynamic hysteresis (DH) model treats the coherent reversal of single domain magnetic nano particles (SDMNP) as kinetic process which is limited by thermal activation. DH sets a time-varying energy barrier determined by the SDMNPs anisotropy energy and the Zeeman energy applied by external field. Therefore, DH defines unitless parameters (σ and ξ) for this kinetic process.[46]

$$\sigma \equiv \frac{KV}{k_B T}, \xi \equiv \frac{\mu_0 H_0 M_s V}{k_B T} \quad (K\text{-anisotropy energy, } V\text{-particle volume}) \tag{2.10}$$

The alignment of particle moment can be assumed that it follows Boltzmann distribution.21 According to the preceding research, DH model turned out to fit well to experimental results, connecting LRT model with the Stoner-Wohlfarth model.[52]

LRT model fits well when the field strength is low enough comparing to its coercive field, so that magnetization is determined by relaxation process. The Stoner-Wohlfarth model corresponds to experimental results well only when the field strength is large enough to neglect the relaxation process. In between these two models, however, there is a region which couldn't be explained without DH model. DH model simplified the question with the assumption saying that whichever path the magnetization process choose, it will be done through thermally activated kinetic process. These 3 different models together explain the behavior of SDMNPs in the entire field condition, which allow us to pick right design for multiplexing.

2.3 Magnetic nanoparticle synthesis

Synthetic routes for magnetic iron oxide nanoparticles are versatile. There are three different methods - physical, biological, and chemical. Physical methods are mainly a top-down approach and use mechanical forces, electron beam, or laser source.[53, 54] This is widely used in industrial fields but not favored in biomedical applications due to limited size and crystalline control. Biological methods use living organisms such as fungi, bacteria, plants to produce magnetic nanoparticles. This approach is getting attention as it can program a biological target to generate endogenous magnetic nanoparticles via gene modification. However, its low productivity, difficult size and phase control, unlike physical or chemical methods, prevent this method from being the mainstream in magnetic nanoparticle synthesis.[55, 56] For this reason, researchers have extensively studied chemical methods and developed multiple techniques for the synthesis. Coprecipitation, microemulsion, hydrothermal, sonochemical, and thermal decomposition techniques are all chemical methods.[57] Among these techniques, thermal decomposition, which uses the decomposition of organo-metallic precursors in organic solvents at elevated temperature, is known to be the best in size, crystallinity, and phase control.[58] As the size, crystallinity, and phase of the magnetic particles affects heat dissipating properties significantly, most of the particles in my thesis study have been prepared using this method.

2.3.1 Organo-metallic decomposition of Magnetite nanoparticles

LaMer first proposed theory for a typical precipitation reaction within a closed system.42 When the concentration of free monomer $[M]$ increases above a critical nucleation concentration $[M_C]$, the solution is supersaturated. As the free monomers get rapidly consumed through nucleation, the free monomer concentration drops below $[M_C]$ in the end and the nucleation events stop. Even though nucleation stopped, still $[M]$ is higher than the equilibrium between monomer and particles with radius $[M_a]$, and this results in particle growth. This separation between the nucleation and growth stages enables monodisperse nanoparticles synthesis. To explain this theory in a little more detail, we can derive thermodynamic equations from the aforementioned parameters. Given supersaturation S as $S = [M]/[M_\infty]$ ($[M_\infty]$ – equilibrium monomer concentration of a flat crystal), the total free energy of the system(ΔG_T) can be drawn by the sum of bulk (ΔG_B) and surface free energy(ΔG_S).

$$\Delta G_T = \Delta G_B + \Delta G_S \tag{2.11}$$

For particles with radius r,

$$\Delta G_B = 4/3\pi r^3 \Delta G_V, \Delta G_S = 4\pi r^2 \gamma \text{ (γ-surface energy)} \tag{2.12}$$

As intrinsic chemical potential ΔG_V is $\Delta G_V = -\frac{RT}{V_M} \ln S$, Eq. 2.11 can be re-written to

$$\Delta G_T = -\frac{4\pi r^3 RT \ln S}{3V_M} + 4\pi r^2 \gamma \text{ (R – gas constant, V_M – molar volume of M)} \tag{2.13}$$

The former bulk term drives precursors to form particles and the latter term prevents them from aggregating. Seeing this, we can deduce there will be an energetic barrier and critical radius of nuclei to overcome (at$\frac{\partial \Delta G_T}{\partial r} = 0$).

$$\Delta G_{nuclei} = \frac{16\pi r^3 V_M^2}{3r^2 T^2 (\ln S)^2}, \quad r_C = \frac{2\gamma V_M}{RT \ln S} \tag{2.14}$$

And by combining Eq. 2.13 and Eq. 2.14, we can tell how fast the nuclei will be formed depending on the supersaturation S.

$$\frac{dN}{dt} = Aexp(-\frac{\Delta G_T(r_C)}{k_B T}) \tag{2.15}$$

N is the number of nuclei, and A is the pre-exponential coefficient

$$A = Z\beta_C N,\ Z = \sqrt{\frac{\Delta G_T(r_C)}{3\pi N_C^2 k_B T}}\ (N_C - \#\text{ of monomers in the critical size nucleus}) \tag{2.16}$$

β_C is the deposition rate of monomers from the solution to the nuclei surface and Z is the Zeldovich factor.43 The growth of nanoparticle can be analyzed in two different way; Fick's first law and Fick's second law. Fick's first law assumes that the diffusive flux is under steady state, which means it's reaction limited case. D is the diffusion coefficient and r is particle radius. $[M]$ and $[M_i]$ represent monomer concentration in solution and particle interface each.

$$J = 4\pi r^2 D([M] - [M_i]) \tag{2.17}$$

This can be re-written using growth (k_r) and dissolution (k_d) rate constant.

$$J = 4\pi r^2 D(k_r[M_i] - k_d) \tag{2.18}$$

$$[M_i] = \frac{D[M] + k_d r}{k_r r + D} \tag{2.19}$$

The growth stage can also be viewed via Fick's second law, which means particle synthesis is a diffusion limited case. 44 Suppose the molar volume of M is V_M,

$$J = \frac{4\pi r^2}{V_M}\frac{dr}{dt} \tag{2.20}$$

$$\frac{dr}{dt} = \frac{DV_M([M] - \frac{k_d}{k_r})}{r + \frac{D}{k_r}}(\text{from}(2.18),\ (2.19)\ and\ (2.20)) \tag{2.21}$$

$K_e = k_r/k_d$ is the size dependent equilibrium constant of the reaction near the particle surface. According to Kelvin equation, which describes the change in concentration due to the curved interface between the particle and solution, equilibrium monomer concentration $[M_e]$ is

$$[M_e] = \frac{1}{K_e} \tag{2.22}$$

$$[M_e] = [M_\infty]exp(\frac{2\gamma V_M}{rRT}) \tag{2.23}$$

(R-gas constant, $[M_\infty]$-concentration of M away from the particle)

From Eq. 2.21, 2.22 and 2.23,

$$\frac{dr}{dt} = \frac{Q(S - \exp(\frac{2\gamma V_M}{rRT}))}{r + \xi} \quad (\xi = \frac{D}{k_r} \text{ and } Q = DV_M[M_\infty]) \tag{2.24}$$

From this model, we can get an idea over parameters for particle design. First, heat up rate (dT/dt) can be regulated by the machine and this give an idea control over the size of particles. From Eq. 2.15, we can expect how many nuclei will be formed in the nucleation stage.

$$N_{total} = \int_{t_{start}}^{t_{end}} \frac{dN}{dt}(T)dt = \int_{T_{start}}^{T_{end}} \frac{dN}{dt}(T)(\frac{dT}{dt})^{-1}dT = (\frac{dT}{dt})^{-1}\int_{T_{start}}^{T_{end}} \frac{dN}{dt}(T)dT \tag{2.25}$$

N_{total} represents number of particles in unit volume. From Eq. 2.25 we can tell if heat up rate is high, the total number of nuclei will decrease. It means monomer has been less consumed during nucleation stage. Therefore it will drive particles to grow larger. If the heat up rate is low, then the opposite will happen. N_{total} will be proportional to the integrated area in (Figure 4).

Growth stage is still undetermined whether it follows diffusion limited growth or reaction limited growth. Previous researches, however, so far show reaction limited growth more fits to the experimental results.45,46 According to these results, we can learn regulating growth speed using temperature is not that effective.

In the synthesis, solvents also have an important role. Functional groups in solvents can be used in regulating chemical potential of oxygen, and this changed chemical potential determines not just the size of the particle but also the phase of the particle.47 The supersaturation above takes an important role in nucleation and growth. It can be increased by adding more precursor, setting higher heat-up rate (monomers comes quickly than their consumption), and using easily decomposable precursors.

2.4 Phase transfer of Magnetite nanoparticles

Engineered nanomaterials demonstrated various biomedical applications in the last two decades. To ensure the safety of the nanomaterials usage in novel nanomedicines, researchers tried to identify the effect of physical and chemical properties of nanomaterials on biocompatibility. (such as size, surface chemistry, and surface charge). Biocompatibility refers to a biomaterial's ability to perform its desired function without eliciting any undesirable local or systemic effects within the host.[59]

There are multiple factors affecting the biocompatibility of nanomaterials. However, hydrophobicity is considered one of the most critical property since it determines how the nanomaterials will respond to various biological processes, such as protein adsorption[60], interaction with biological membranes[61], cellular uptake[62, 63], immune response[64], and hemolytic effect.[65] In general, the more hydrophobic particles aggregate proteins and other nanoparticles around, causing immune system activation. Unter healthy conditions, hydrophobic cellular materials are not exposed to the external environment. However, during necrotic cell disruption or protein denaturation, these hydrophobic materials get released and interacted with cellular membranes and specific cellular receptors, and an innate immune response initiates. For this reason, hydrophobicity is considered to be a potentially dangerous cellular materials.[64]

Magnetic nanoparticles synthesized using organo-metallic decomposition method uses organic solvents that can provide high enough temperature to induce the pre-

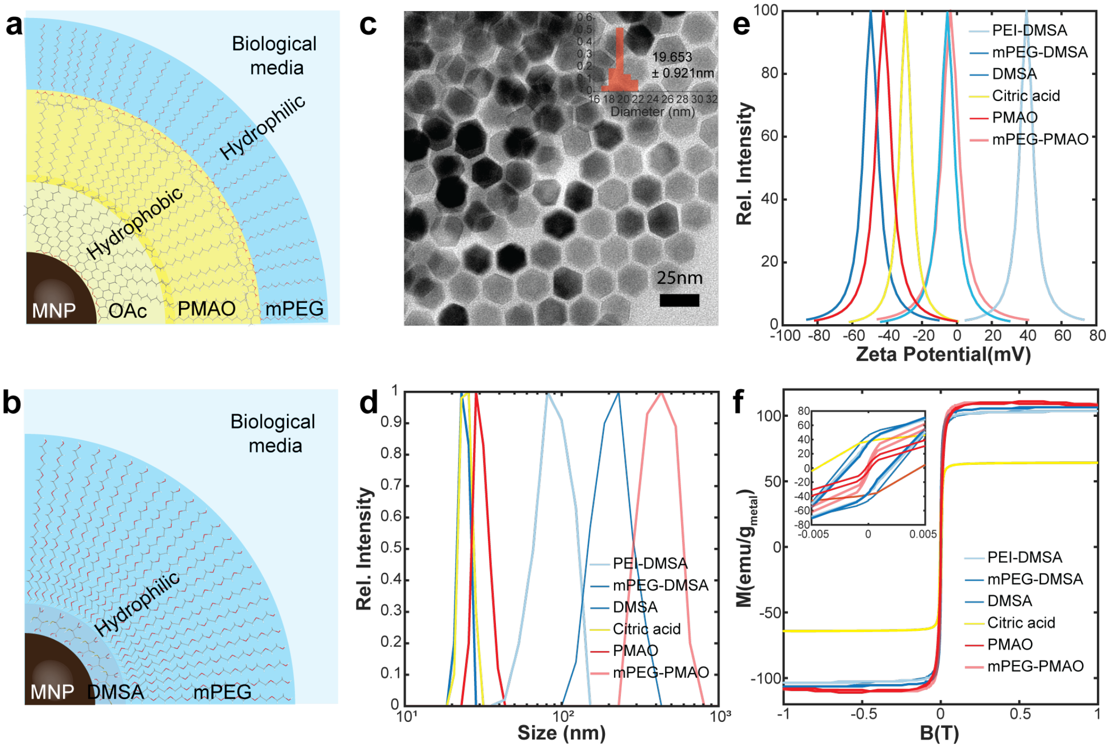

Figure 2-3: **Phase transfer of synthesized magnetic nanoparticles from organic phase to aqueous phase** Schematic overview of phase transfer using (a)amphiphilic polymer (PMAO-mPEG) and (b)ligands exchange and sequential polymer attachment (DMSA-mPEG). (c)TEM images of iron oxides(Fe_3O_4) and its size distribution before phase transfer. (d)The particle size distribution of Fe_3O_4 collected by Dynamic light scattering (DLS) intensity measurement

cursor decomposition. Hydrophobic ligands have been used to suspend and stabilize nanoparticles within organic solvents, which prevents nanoparticles' coagulation during synthesis. The undesirable toxicity coming from this hydrophobicity can be avoided by engineering the surface chemistry of nanoparticles become hydrophilic.

In this thesis work, two different surface modification techniques - polymer encapsulation and ligand exchange - have been applied to enhance the biocompatibility of magnetic nanoparticles. As shown in Figure 2-3 (a), polymeric coating of magnetic nanoparticle using amphiphilic polymer is similar to the biophysical processes in a

Table 2.1: Summary for properties of phase transferred magnetic nanoparticles

Method		Size distribution by DLS (nm)	Polydispersity Index (PDI)	Zeta Potential (mV)	Magnetic Saturation (M_S) (emu/g_{Metal})
Amphiphilic polymer	PMAO	30.914692 ± 4.2548612	0.080022047	-42.446	110.2741
	PMAO-mPEG	428.51531 ± 119.99377	0.078412393	-4.077	110.9548
Ligands exchange	Citric acid	24.636555 ± 2.6340977	0.018942659	-29.736	64.206225
	DMSA	23.783498 ± 2.2654651	0.009073259	-49.88	103.7546585
	DMSA-mPEG	218.17463 ± 68.723305	0.011431515	-6.235	106.54706
	PEI-DMSA	90.250767 ± 25.530289	0.099220081	39.089	103.545706

way that both conceal hydrophobic particle via encapsulation. This method leaves oleic acid attached to the particle surface intact. Ligands attached to the particle surface influence oxidation states of particle shells and influence magnetic properties. Thus there is no significant difference in magnetic properties between before and after phase transfer when using amphiphilic polymer. [66].

Amphiphilic polymer, poly(ethylene glycol) methyl ether grafted poly(maleic anhydride-alt-1-octadecene) (mPEG-PMAO) was prepared by a similar protocol to previous studies.[67] PMAO also forms hydrophilic succinic acid when its anhydride functional group meets water, therefore without any further treatment, PMAO also used as purchased. Magnetic nanoparticles (2 5mg) were dispersed in 1ml of mPEG-PMAO or PMAO dissolved chloroform (concentration 10 mg/ml). The mixture was sonicated for 15 minutes and then evaporated under a vacuum. 1ml of 1x Tris-acetate-EDTA (TAE) buffer was added and sonicated for re-dispersion. Magnetic nanoparticles were spun down and washed three times with ddH2O. For the in vitro experiment, MNPs were re-dispersed in Tyrode's solution in the final step.

On the other hand, the ligand exchange method can introduce a significant change in the properties of magnetic nanoparticles. Especially, ligand exchange using citric acid introduced substantial changes in magnetic properties of nanoparticles as shown in Figure 2-3 (f) and Table 2.4. Nanoparticles were modified using a previously reported method. [68] This method includes heating of the solvents mixture, which causes significant oxidation state changes. Citric acid-treated particles weren't stable enough to do sequential polymeric coating on the magnetic particle and precipitated during the chemical process. Unlike citric acid, 2,3-Dimercaptosuccinic acid (DMSA) makes disulfide bonds one another and gives higher stability. The protocol of phase transfer using DMSA has been slightly modified by changing DMSO solvent to methanol to facilitate the drying process and washing step. [68] Due to enhanced stability, additional polymers with amine groups could be attached to the carboxylic group of DMSA using carbodiimide crosslinker chemistry.

Chapter 3

Modeling, Characterization of MNPs and Electronic Apparatus for Selective Heating of MNPs

3.1 Characterization of magnetic material

The use of magnetic nanoparticles in biomedical fields has been the most representative examples of how nanotechnology can be applied to medical applications. These biomedical applications rely on nanoparticles' magnetic properties, including saturation magnetization, remanence and coercivity, magnetic diameter, magnetocrystalline anisotropy, and mechanism of magnetic relaxation. Therefore, accurately quantifying these properties is crucial to guarantee the system work as intended and to maximize the potential of iron oxide nanoparticles depending on their applications. Some of the magnetic properties can be analyzed through traditional characterization techniques using a vibrating sample magnetometer (VSM) or superconducting quantum interference device (SQUID) magnetometers. However, magnetic nanoparticles in several biomedical applications undergo different environments that cannot be covered with these traditional techniques, such as exposure to alternating magnetic fields of high amplitude (< 0.05 T) radio frequencies (10s 100s kHz) or freely suspended states within solutions. This section will introduce some of the characterization techniques that can apply to these conditions.

3.1.1 Magnetic diameter and physical diameter of magnetic nanoparticles

Iron oxides is a multi-phasic material. [69] For this reason, several parameters, such as solvent pH, oxygen chemical potential, temperature and synthesis method, can affect the phase of synthesized iron oxide nanoparticles and often result in different surface and core phases. X-ray powder diffraction (XRD) is a common techique for phase characterization requires extra steps for sample preparation. However, magnetic diameter measurements using ferrofluids and VSM can offer a fast and simple magnetic phase characterization for iron oxide nanoparticle.

Magnetic particles are freely suspended in water, enabling continuous alignment of their moments with the applied field via physical rotation. This allows the magnetic diameter of a reasonably monodisperse particle ensemble to be determined under the assumption that the ensemble exhibits ideal superparamagnetic behavior in the limit of low applied fields. (The fitting technique employed here in the limit of low fields works equally well for fixed particles exhibiting anisotropy, provided they are randomly oriented. [46])

$$M_{experiment}(\xi) = M_{S-experiment} L(\xi), \tag{3.1}$$

Where $L(\xi)$ is the Langevin function, and $\xi(\mu_m B)/(k_B T)$,

$$(\mu_m = M_{S-theoretical} V_m,\ V_m \text{ is the magnetic volume}) \tag{3.2}$$

For a magnetic field approaching B 0 mT ($\xi \sim 0$), the Langevin function is approximately linear

$$M_{experiment}(\xi) \approx M_{S-experiment} \times \frac{\mu_m B}{3 k_B T} \tag{3.3}$$

Therefore,

$$\frac{M_{experiment}(\xi)}{M_{S-experiment}} = \frac{V_m M_{S-theoretical}}{3 k_B T} B \tag{3.4}$$

$$\frac{d(\frac{M_{experiment}(\xi)}{M_{S-experiment}})}{dB} = \frac{V_m M_{S-theoretical}}{3 k_B T} = slope \tag{3.5}$$

The magnetic diameter d_m can then be determined from the magnetic volume:

$$V_m = \frac{4}{3}\pi(\frac{d}{2})^3 \tag{3.6}$$

$$d_m = \sqrt[3]{\frac{18k_BT \times slope}{\pi M_{S-theoretical}}} \tag{3.7}$$

3.1.2 Calorimetric measurement: Specific loss power

Magnetic nanoparticles have been utilized as heat transducer using their hysteric heat dissipation during magnetization process. The heating efficiencies are referred as specific loss powers (SLPs) having W/g_{Metal} as their unit. This can be directly measured by monitoring temperature change of thermally insulated ferrofluids exposed to alternative magnetic fields.

Phase transferred ferrofluid solutions were concentrated/diluted to $2mg_{Metal}/ml$. A custom made series resonant circuit powered by 200W amplifier (1020L, Electronics & Innovation) receiving a sinusoidal signal from a function generator (Keysight 33210A) produced an alternating magnetic field. Field strength was adjusted by monitoring voltage induced in a pickup coil connected to oscilloscope (Keysight DSO-2004A). Temperature profiles were collected by fiber optic IR thermometer (Omega HHTFO-101), which is insensitive to alternating magnetic fields.

3.1.3 Dynamic magnetization captured by AC magnetometer

Regarding SLP measurements, calorimetric methods are the most mainly used approach. In this manner, dissipated heat energy is obtained from the initial temperature derivative over time. However, as any other calorimetric methods do, it's also easy to get influenced by the temperature gradients of nearby environments, heat capacities of the system and the sample, and heat conductivity. Therefore, alternative methods have been proposed to acquire the hysteric loss of MNPs like the AC magnetometer. These methods showed more reliable SLP results with temperature variations, and they even captured additional information about the magnetic behavior of the system. [70, 71, 72, 73, 74]

They have selected a solenoid design for the magnetic field generating and detecting coils. This design is intuitive and facile to fabricate, but they also had some innate shortcomings. First, an air-cooled solenoid is not always the best choice to produce a strong magnetic field efficiently with minimal input power. Ferrite, which are often used as a transformer core, has about 1500 3000 relative permeability.[75] This core can work as a magnetic lens that focuses and traps magnetic flux within the magnetic core, and can produce stronger magnetic fields to targeted space with minimal energy.[76]

Also this design can give better uniformity if the field targets only a few cubic centimeter spaces. The less uniform magnetic field from the solenoid and the 3D design of the detecting coils inside AMF generating solenoid makes the detected signal easily disturbed by the slight change of the sample/detecting coils position.

3.2 Custom design of AC magnetometer

To overcome the aforementioned shortcomings, new designs were adopted to build magnetic field generator and detecting coils. Transformer ferrite E core has been shaped using diamond saw to have continuous magnetic flux within the magnetic core except the center open gap. Both magnetic core was then winded using litz wires to minimize resistance coming from skin depth effect. The core design was simulated using Finite element magnetics methods (FEMM) to ensure to have large enough area for uniform fields. (Figure3-1 a) The simulated results showed corresponding match to the actual measurements and the search coils were placed based on this simulation profile and the experimental data. (Figure3-1 b and c)

A custom designed AC magnetometer was built using 2 layer, 8mm thick printed circuit boards. Signals collected by the coil were also amplified by integrated circuit chips incorporated into the PCB. The sample holder, which contains a hollow sphere for ferrofluid injection was prepared by a 3D printer (Formlabs Form 2). After the cavity was filled with ferrofluid, it was sealed with a glue gun. The AC magnetometer was placed in the center of the gap of the electromagnet generating the AMF with the filled holder inside. The signal from a control sample (water) was subtracted from the signals measured from samples to isolate signal coming from dynamic magnetization of the MNPs.

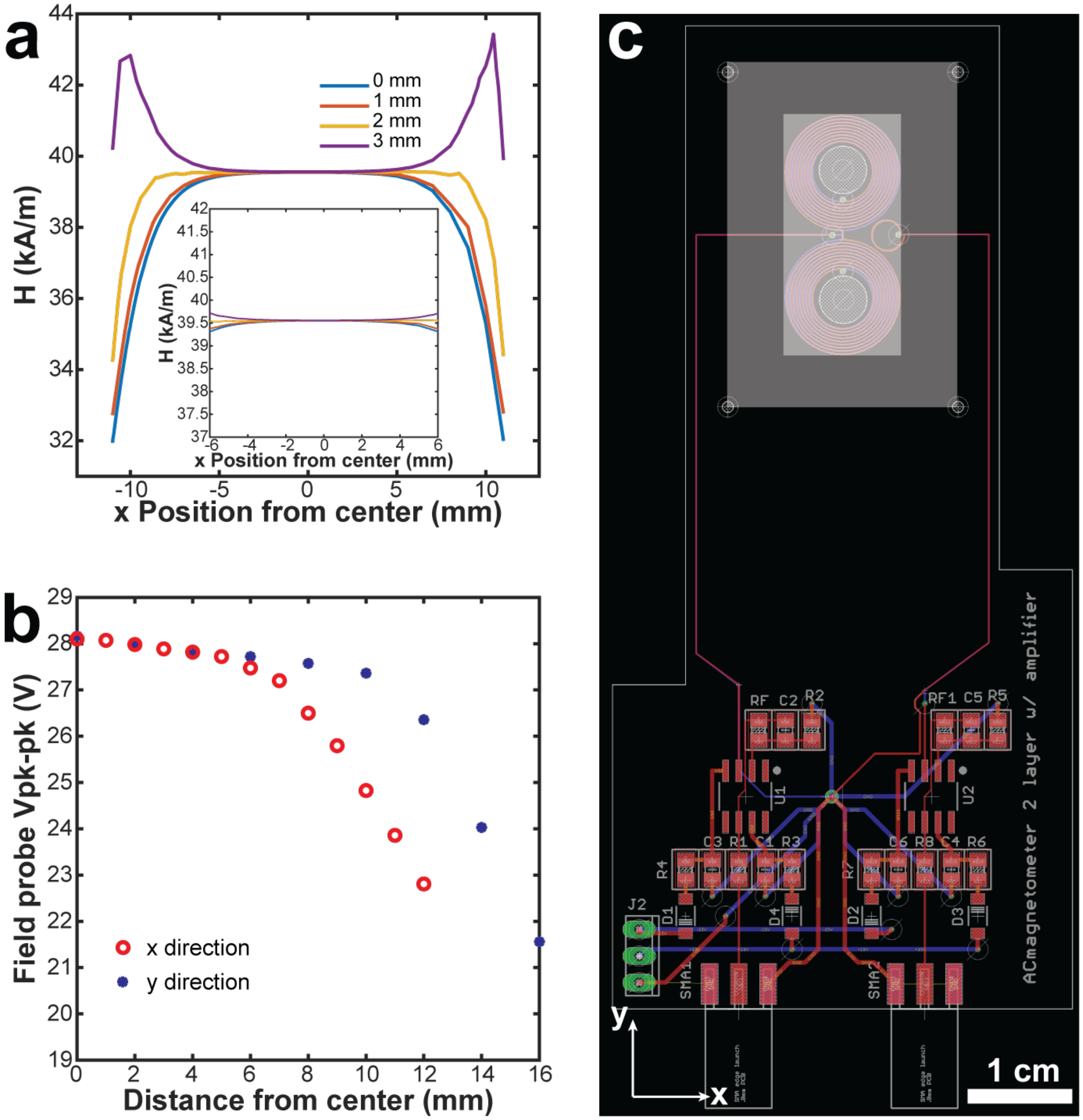

Figure 3-1: **Characterization of AC magnetometer** Magnetic field profile across the magnetic core of magnetic field generator.(a) Simulated magnetic field profile using Finite Element Magnetics Methods (FEMM). (b) Peak to peak voltage profile measured using pickup coil. (c) PCB layout of AC magnetometer. Bigger white box represents the physical magnetic core size, and inner white box means magnetic uniformity ensured area.

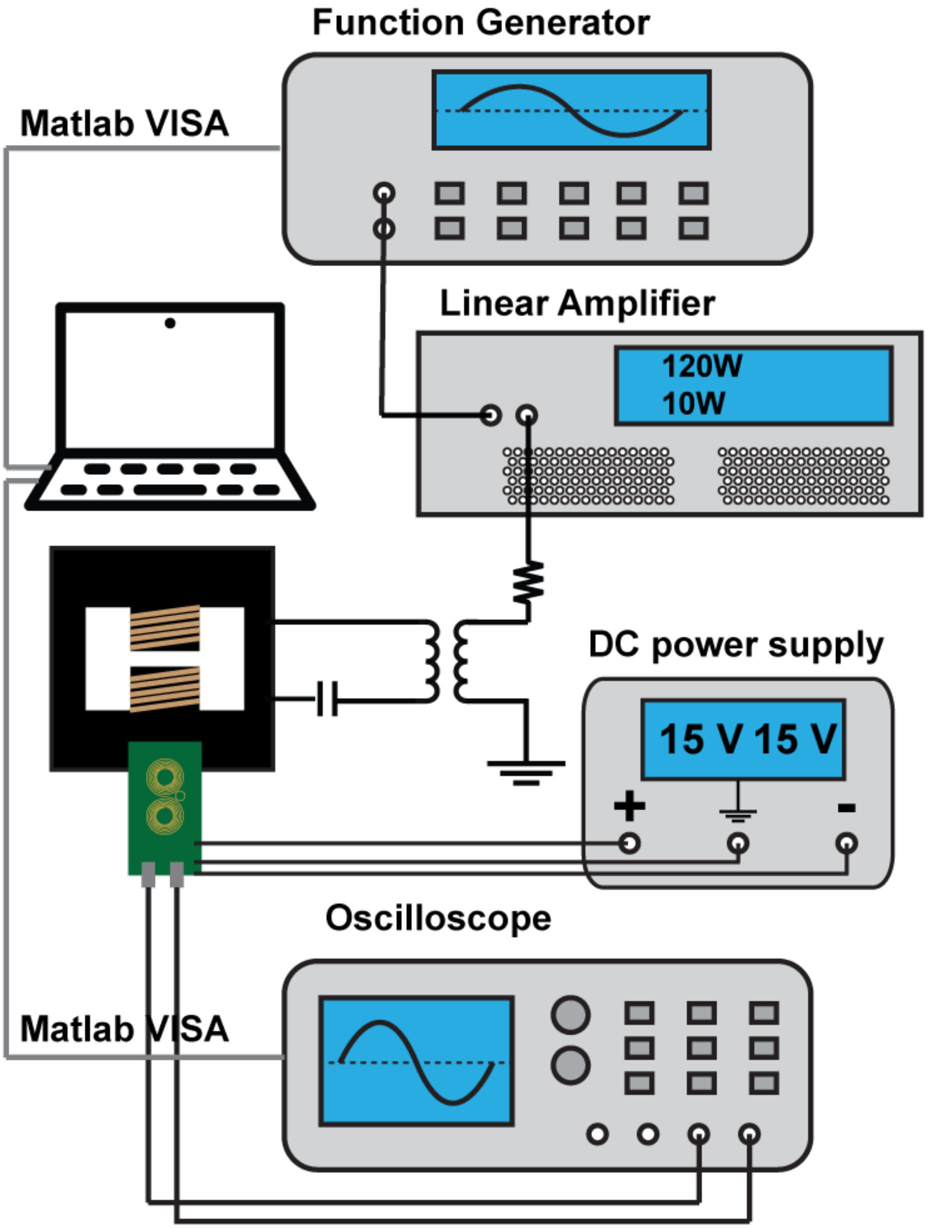

Figure 3-2: **Schematic overview of AC magnetometer and field generator setup**

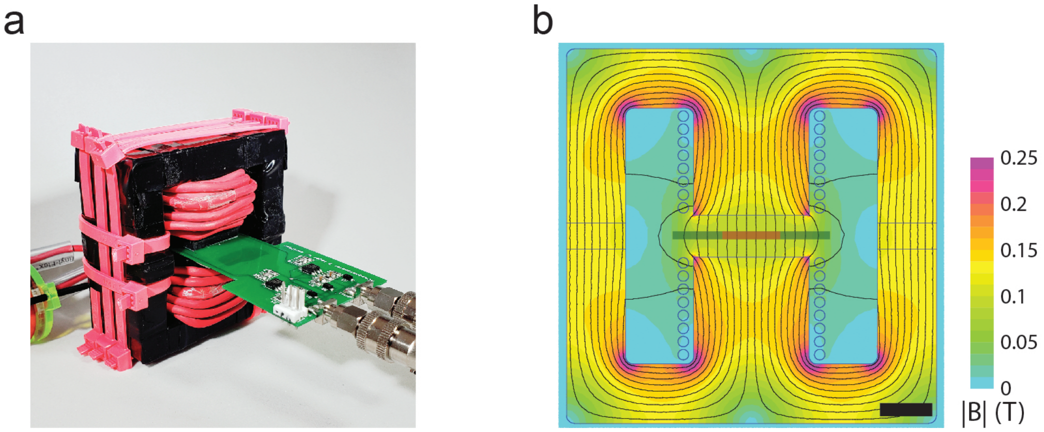

Figure 3-3: **AC magnetometer assembly and magnetic flux density plot.** (a) AC magnetometer assembly composed of AC magnetometer board and AMF generator. (b) Simulated magnetostatic flux density plot calculated via Finite Element Method for Magnetics (FEMM). Our 2D AC magnetometer is placed in the center of the magnetic core gap with 5 mm margin to every edge to ensure field uniformity. (Black line – scale bar = 1 cm, green line – PCB plate, red line – spiral coil sensor)

The system was operated by the computer through Matlab VISA. (Figure3-2) The collected voltage signal was saved and later integrated after subtracting blank signals. The net signal were integrated to get hysteresis data, and the sensitivity was calibrated using a fixed magnetic sample, VSM, and calorimetric measurements. Each hysteresis collection was again translated into SLPs and processed using Matlab and Mathematica codes to find the optimal multiplexing field conditions.

3.3 Modeling of Magnetic nanoparticles

3.3.1 Numerical Calculation of Dynamic magnetization of Magnetic nanoparticles

To investigate the dynamic magnetization response and hysteresis of single domain magnetic nanoparticles exposed to alternating magnetic fields, we conducted numerical calculations based on a dynamic hysteresis model implemented in Mathematica.[52, 46] Dynamic hysteresis models are most appropriate at frequencies well below the period of precession of magnetic moments described by the Landau Lifshitz Gilbert (LLG) equation. Rather than describing this precession, they instead treat coherent reversal of single domain MNPs (SDMNP) moments as a thermally activated kinetic process. A function describing the energy of possible orientations of individual particle moments accounts for two main contributions: the anisotropy of a SDMNP and its Zeeman energy in the external field. The resulting energy landscape has local minima that can be envisioned to each entrap a subpopulation of the moments in an ensemble, with some escaping to the other minimum at a rate determined by the energy barrier separating the minima. The net magnetization of this ensemble is thus determined by the fraction of moments residing in each energy minimum, typically neglecting the effect of local Boltzmann distributions within the minima. Since Zeeman energy depends on the external field, which varies in time, the energy landscape is also time-variant. Consequently, the switching rate from one energy minimum to another varies periodically with the applied field. To simplify the model, magnetic anisotropy was approximated with an easy-aligned, effective uniaxial anisotropy. The anisotropy of a SDMNP and its Zeeman energy can be expressed in a form normalized to ambient thermal energy by defining the quantities σ and ξ as follows.

$$\sigma = \frac{KV}{k_B T}, \quad \xi = \frac{M_S V B}{k_B T} \tag{3.8}$$

(K - magnetic anisotropy, V – magnetic nanoparticle volume, k_B – Boltzmann constant, T – 298 K room temperature, M_S – saturation magnetization, B – applied field)

Our dynamic hysteresis model followed previous work with some variations, and more detailed descriptions of this dynamic hysteresis model can be found there.[52, 46] Unlike the previous work,[52, 46] here the pre-exponential factor of relaxation time, τ_0, was not fixed to 10^{-9} s in order to reflect the fact that the pre-exponential factor is expected to vary with the anisotropy of SDMNP and the external field.[77, 78] From the LLG equation, neglecting stochastic thermal effects, characteristic relaxation time (τ_c) is shorter for higher applied field ($\tau_c \propto \xi^{-1}$).[78] By considering this correlation [78] and the dependency of pre-exponential factor of Néel relaxation on anisotropy of the SDMNP in the Fokker-Planck equation,[77] the pre-exponential factor τ_0 was made proportional to $\sigma^{-3/2}\ \xi^{-1}$. According to Leliaert at al., τ_0 is varies between 10^{-8} to 10^{-12} s for Fe_3O_4.[79] Consistent with this work, our τ_0 was multiplied by a suitable constant to place it within the same range:

$$\tau_0 = (2.04598210^{-7}s) \cdot \sigma^{-3/2}\xi^{-1} \tag{3.9}$$

Moreover, to account for the actual particle size distribution, each MNP ensemble's mean diameter and standard deviation were used to generate 100 random particles with a Gaussian distribution. The σ and ξ values corresponding to this statistical sample of particles were entered into our numerical model and the resulting magnetization responses were averaged to generate a population-averaged dynamic hysteresis loop. For side-by-side comparison, hysteresis loops calculated by the dynamic magnetization model and collected AC magnetometer have been drawn in Figure 3-4 and Figure 3-5.

3.3.2 Finite Element Analysis on heat transfer of ferrofluid droplets

To determine the minimal distance that prevents crosstalk between two adjacent ferrofluid droplets acting as heat sources inside a model system of a mouse brain, we applied a finite element model of heat transport.

Pennes' bio-heat equation was used to account for the influence of blood perfusion within the brain tissue:

$$\rho_B C_B \frac{\partial T}{\partial t} = K_B \bigtriangledown^2 T + \rho_b C_b w_b (T - T_b) + Q \tag{3.10}$$

Where ρ_B, ρ_b and C_B, C_b are densities and heat capacities of the brain and blood, respectively; K_B is the thermal conductivity of the brain; T_b is blood temperature; and w_b is the cerebral blood flow. Q is the power density of the heat source, and T – temperature. Two distinct ferrofluid injections (MNP1 and MNP2) inside the brain tissue were approximated as spheres acting as sources of constant power density Q due to the AMF. We calculated the temperature profile of the tissue as a function of

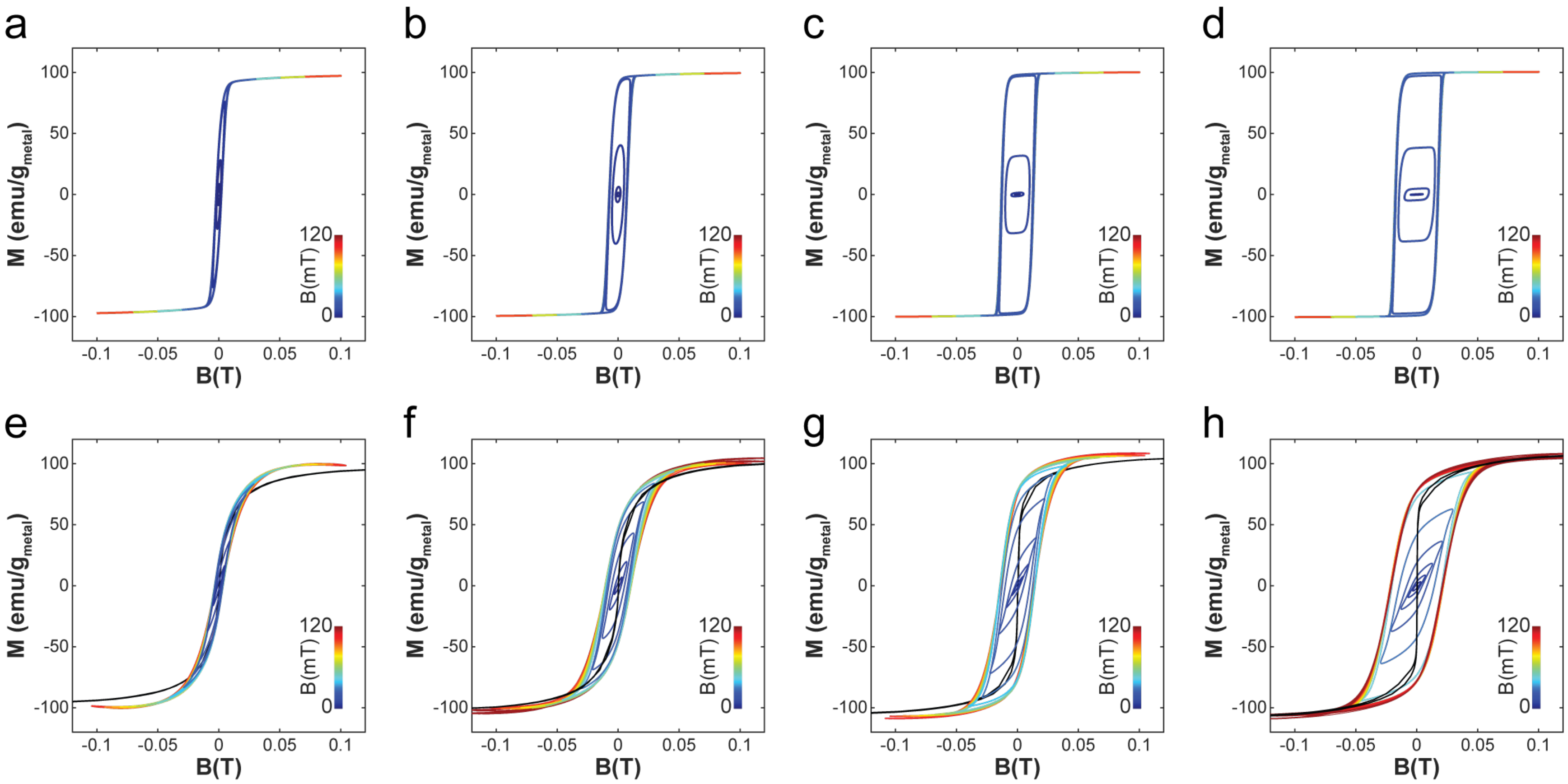

Figure 3-4: **Direct, side by side comparison of dynamic magnetization of** Fe_3O_4 from dynamic hysteresis model calculated using Mathematica (a-d) and direct AC magnetometer measurement.(e-f) (a and e, 16.3nm; b and f, 20.5nm; c and g, 25.2nm; d and h, 31.2nm) Black lines in (e-f) correspond to VSM data, rainbow colored loops correspond to custom-built AC magnetometer data. All data were collected at a frequency $f = 75$ kHz.

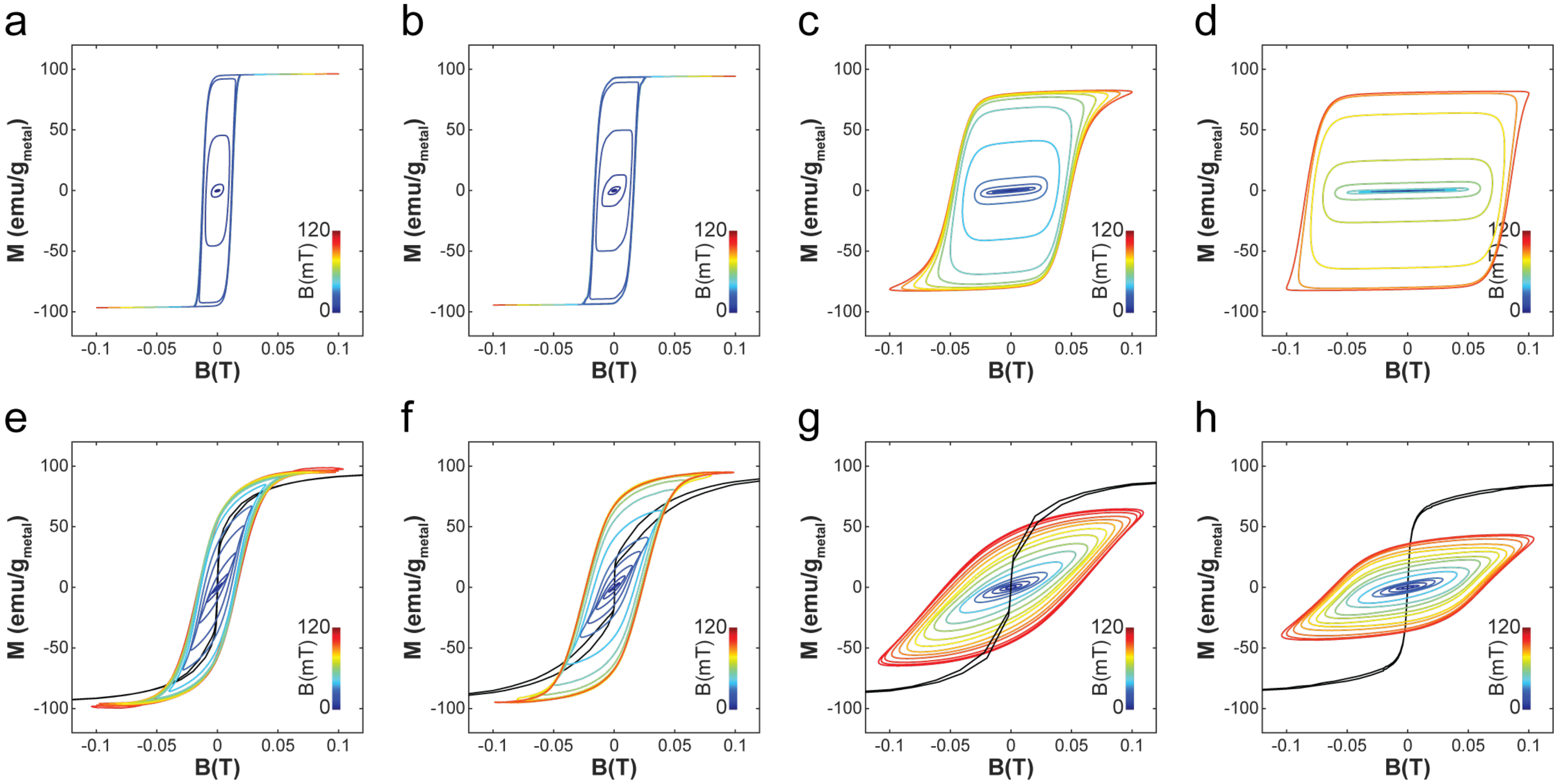

Figure 3-5: **Direct, side by side comparison of dynamic magnetization of** $Co_xFe_{3-x}O_4$ from dynamic hysteresis model calculated using Mathematica (a-d) and direct AC magnetometer measurement.(e-f) (a and e, x=0.01, 26.7nm; b and f, x=0.03 32.5nm; c and g, x=0.14 19.5nm; d and h, x=0.24 18.6nm) Black lines in (e-f) correspond to VSM data, rainbow colored loops correspond to custom-built AC magnetometer data. All data were collected at a frequency $f = 75$ kHz.

time. The physical parameters used in our model are summarized in the Table 3.1 Q was calculated as:

$$Q = V_{MNP} * SLP_{MNP} * \rho_{MNP} \tag{3.11}$$

where V_{MNP} is the total volume of MNPs in the droplet, ρ_{MNP} is the concentration of MNPs and SLP_{MNP} is the specific loss power for the MNPs in the examined AMF conditions of 1 = 522 kHz, H1 = 10 kA/m and 2 = 50 kHz or H2 = 70 kA/m. SLPs for MNP1 and MNP2 from the thermographic recording (Figure 4) were used in this model (Table S**??**). Prior research indicates that injected MNPs coated with mPEG-PMAO polymer stay mainly within injected area, even after a month. [13] Therefore, in our model, we also assumed that injected ferrofluids will maintain their shapes. To assess the minimal distance required for selective heat control, we ran multiple simulations at varying distances between ferrofluid droplets (d = 0, 1, 2, 3, 4 mm) (Supplementary Video S2 and Figure 3-6). In our model, an AMF with 1 = 522 kHz, H1 = 10 kA/m was applied for the first 20s, followed by a 60s rest epoch, then another AMF with 2 = 50 kHz, H2 = 70 kA/m was applied for 20s, followed by another 60s rest (Figure 3-6 (a)). As the distance between the droplets exceeds 2 mm, the regions of elevated temperature generated by two ferrofluid droplets are clearly separated (Supplementary Video S2 and Figure 3-6). This suggests that the multiplexed magnetothermal system can target nearby organ regions such as distinct areas of the brain even in small rodents (Figure 3-6(c)).

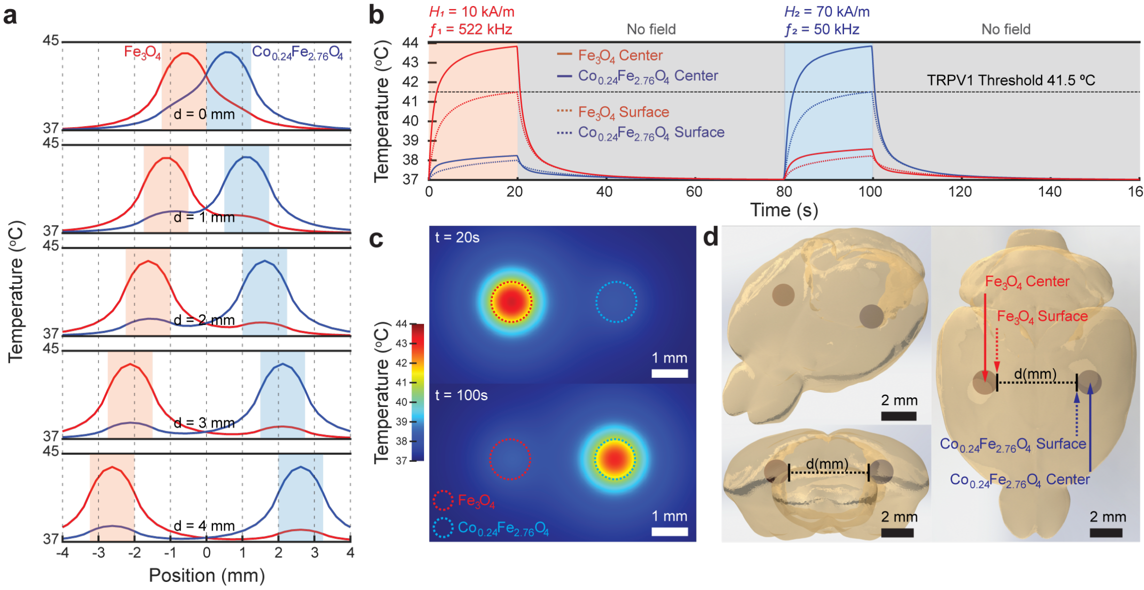

Figure 3-6: **Temperature distribution for the two multiplexed ferrofluid droplets injected within the brain tissue and exposed to the tailored AMF conditions.** (a) Temperature profiles for MNP1 (Fe_3O_4, red) and MNP2 ($Co_{0.24}Fe_{2.76}O_4$, blue) along centers of the ferrofluid droplets separated by distance d = 0, 1, 2, 3, 4 mm between their surfaces. Shaded areas mark the droplet positions (red - Fe_3O_4, blue – $Co_{0.24}Fe_{2.76}O_4$) (b) Temperature profile of each droplet at the center and on the surface over time (d = 2 mm). (c) Heat maps of the ferrofluid droplets within the brain tissue at t = 20 s and t = 100s (d = 2 mm). (d) Three-dimensional view of the ferrofluid droplets injected in the different hemispheres of the mouse brain.

Parameter	**Value**
Blood density ρ_b	1050 kg/m^3 [27]
Blood specific heat capacity $C_{p,b}$	3617 $J/(kg \cdot K)$ [27]
Cerebral blood flow ω_b	1.07 $ml/g/min$ [80]
Arterial blood temperature T_b	37 ^oC [27]
Initial and boundary temperature T_0	37 ^oC [27]
Brain specific heat capacity $C_{p,B}$	3630 $J/(kg \cdot K)$ [27]
Brain density rho_B	1065 kg/m^3 [27]
Brain thermal conductivity K_B	0.51 $W/(m \cdot K)$ [27]
Fe_3O_4 ferrofluid concentration	115.534 mg_{Metal}/ml
$Co_{0.24}Fe_{2.76}O_4$ ferrofluid concentration	64.674 mg_Metal/ml

Table 3.1: Physical parameters used in the FEA modeling

Chapter 4

Selective modulation on cellular signalling via multiplexed bulk heating of MNPs

4.1 Background and Motivation

Emerging biomedical applications of heat dissipation by magnetic nanoparticles (MNPs) in alternating magnetic fields (AMFs) include control of cell signaling, gene expression, and drug release.[81, 39, 27] Despite the unparalleled access to deep physiological targets offered by magnetic fields, independently addressing biological pathways via focused AMF application is typically infeasible. One recent solution borrows methodology from magnetic particle imaging, superimposing a magnetostatic field to restrict MNP heating to points of vanishing field magnitude.[52, 46] Although this approach can offer targeted heating with millimeter resolution, it is ill-suited to freely moving subjects or targets with spatial overlap. Here, we present a materials-based approach for independent magnetic control of multiple sites or processes based on "magnetothermal multiplexing," the independent heating of MNPs with differing coercivities upon exposure to paired AMF conditions.6 We report the model-driven development of a suitable materials system and use it to demonstrate selective actuation of intracellular calcium ion influx in vitro.

When MNPs are exposed to AMFs, they dissipate heat arising from thermodynamic irreversibility in the response of their magnetization. This irreversibility can be graphically represented by hysteresis loops, which enclose an area corresponding to the heat dissipated per magnetization cycle. While all models for heat dissipation by MNPs can be understood as methods for predicting hysteresis loops, the "dynamic hysteresis" model does this by describing magnetization response as a kinetic process determined by an energy landscape consisting of the effective anisotropy energy and the configurational energy of the MNP moment in the applied AMF.[82, 48] The relevant energy contributions depend on the MNP materials properties (effective magnetic anisotropy K_{eff}, saturation magnetization M_S, volume V), temperature T, and the applied AMF conditions (field amplitude H and frequency). According to the dynamic hysteresis model, the MNPs that produce large hysteresis loops combine high M_S with anisotropy barriers sufficient to prevent spontaneous reorientation of their magnetic moments in the absence of an applied AMF at the relevant timescale.

Major hysteresis loops are observed when AMF amplitude is sufficient to overcome the anisotropy barrier to magnetization reversal, whereas lower AMF amplitudes yield only minor loops with comparatively smaller areas.[82, 48] If effective magnetic anisotropy K_{eff} is increased while magnetization remains constant, the major hysteresis loops are expanded, and an increase in AMF amplitude is required to access them.

Provided that the AMF amplitude-frequency product is constrained to mitigate off-target heat dissipation,8 MNPs heat optimally in AMFs with the minimum amplitude required to access their major hysteresis loops and the highest permissible frequency. For MNPs composed of magnetic ferrites ($A_xFe_{3-x}O_4$, A=Fe, Co, Mn, Ni, x1) K_{eff} can be manipulated by introducing transition metals to iron oxide.[83] Cobalt substitution into Fe3O4 breaks d-orbital degeneracy, leading to stronger spin-orbit coupling, increased magnetic anisotropy, and expanded hysteresis loops (Figure **??**(a, b)).[84, 85, 86] Engineering magnetic anisotropy produces MNPs with sufficiently distinct optimal AMF conditions to enable selective heating. Based on this reasoning, we developed a materials-based system consisting of MNP ensembles with low- and high-K_{eff} (Figure **??**(a, b)). High-K_{eff} MNPs dissipate heat most efficiently in response to AMFs with high amplitude and low frequency (H high low, Figure **??**(c)), whereas low-K_{eff} MNPs dissipate heat most efficiently in response to AMFs with low amplitude and high frequency (H low high, Figure **??**(d)).

We then demonstrated multiplexed magnetothermal control over cellular signaling in vitro (Figure **??**(c and d)) using human embryonic kidney cells (HEK293FT) trans-

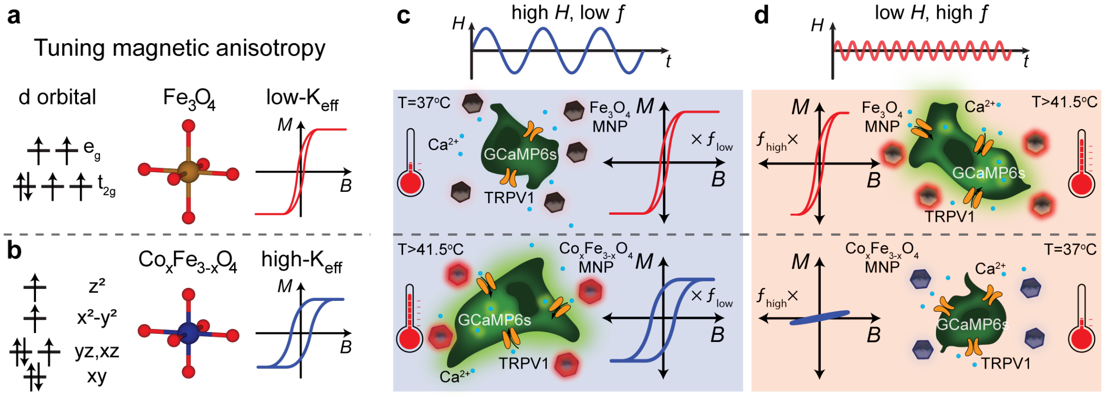

Figure 4-1: **Design of multiplexed control of cell signaling using selective magnetothermal stimulation.** (a and b), Doping of cobalt into Fe_3O_4 results in higher magnetic anisotropy, making cobalt ferrite MNPs magnetically harder compared to Fe_3O_4. c and d, Schematic representation of multiplexed magnetothermal control of cell signaling using two different MNP ensembles that respond selectively to paired AMF conditions. c, A high-amplitude, low-frequency AMF is sufficient to access major hysteresis loops for both MNPs, with the major hysteresis loops of $Co_xFe_{3-x}O_4$ MNPs inherently larger, causing them to heat preferentially. d, An AMF with low amplitude and high frequency results in major hysteresis loops only for less coercive MNPs (Fe_3O_4), and minor loops for $Co_xFe_{3-x}O_4$. The MNPs only dissipate heat effectively when they are exposed to their respectively paired AMF conditions, triggering the opening of the heat sensitive TRPV1 ion channels exogenously expressed in the HEK cells. Calcium ions flow into the cells through the activated TRPV1 channels and bind to GCaMP6s indicators, producing an increase in green fluorescence.

fected to express transient receptor potential vanilloid family member 1 (TRPV1). This cation channel is sensitive to heat and capsaicin, transporting divalent cations such as Ca^{2+} across the membrane at temperatures exceeding 41.5 ± 1.1^oC.13 Thermal activation of TRPV1 can be inferred from Ca^{2+} influx observed via increased fluorescence of a coexpressed calcium indicator GCaMP6s.[27, 87] Surrounding the heat-sensitized cells with solutions of either low-K_{eff} or high-K_{eff} MNPs enabled observation of a selective response to the AMF conditions paired with the surrounding ferrofluid.

4.2 Tuning of magnetic nanoparticles for multiplexed bulk heating

To identify two MNP ensembles suitable for magnetothermal multiplexing, we synthesized an array of magnetite (Fe_3O_4) and cobalt doped ferrite ($Co_xFe_{3-x}O_4, 0 < x < 1$) nanoparticles with varied dimensions and Co content (Figure 4-3 (a-h)). X-ray powder diffraction (XRPD) confirmed the inverse spinel crystal structure of the magnetite and cobalt ferrite MNPs (Figure 4-3 (i)). This finding was additionally consistent with a comparison of the effective MNP magnetic moments to the expected magnetic moments assuming bulk material M_S (Figure 4-3).[41, 87] An increase in the coercive field (H_C) for cobalt ferrite MNPs was observed for samples in which physical rotation of MNPs was prevented (Figure 4-3 (j)). Cobalt concentration in the MNPs was controlled stoichometrically during synthesis and corroborated by inductively coupled plasma atomic emission spectroscopy (ICP-AES) (Figure 4-3 (k)). To ensure colloidal stability in aqueous solutions, MNPs were coated with a biodegradable amphiphilic polymer poly(maleic anhydride-alt-1-octadecene) (PMAO) covalently linked to poly(ethylene glycol) methyl ether (mPEG).[67]

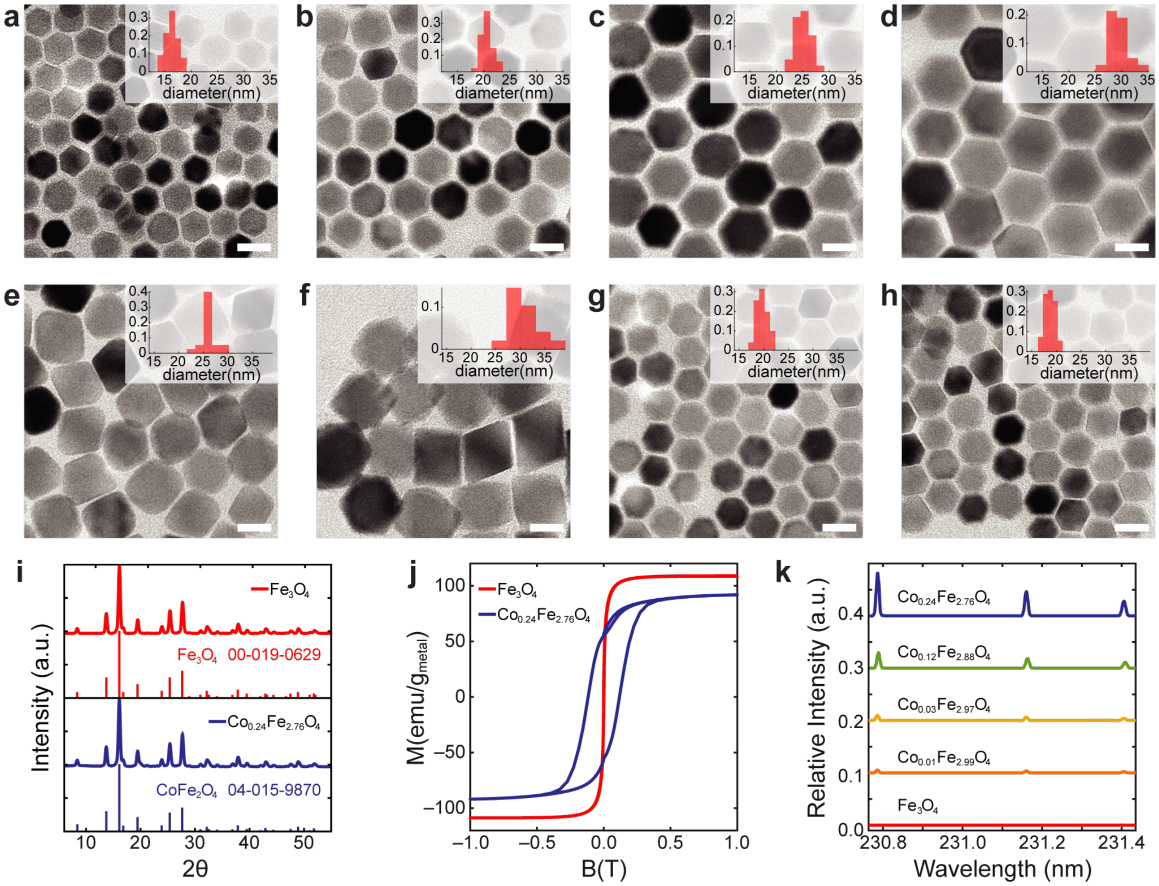

Figure 4-2: **Characterization of magnetic nanoparticles.** (a-h), TEM of Fe_3O_4 (a-d) and $Co_xFe_{3-x}O_4$ (e-h) magnetic nanoparticles and their size distributions from TEM (inset histograms). (i) Powder XRD of Fe_3O_4 and $Co_xFe_{3-x}O_4$ nanoparticles indicates single-crystal structure (inverse spinel). (j) Magnetization data were collected with a SQUID magnetometer to confirm the difference between hard and soft MNPs. To exclude physical rotation of suspended magnetic particles in water, the measurement was performed at 260K. (k) Incorporated cobalt concentration in each ensemble was analyzed by ICP-AES. Each line shows relative cobalt intensity to iron intensity at 234.830nm.

4.3 Characterization of magnetic nanoparticles

4.3.1 Magnetic diameter and physical diameter of magnetic nanoparticles

In order to enable selective heating of magnetic nanoparticles feasible, magnetic response to applied field should be strictly regulated. Iron oxide's multi-phasic properties hinder to withdraw designed magnetic response on each field conditions.[69] To prevent this, magnetic diameter and physical diameter of the synthesized particles have been compared to make sure that the particles are all having inverse spinel ferrite structure.

To maintain $\xi \sim 0$ condition, which is required for an accurate linear Taylor approximation of $L(\xi)$, the cutoff for the fitted region of magnetic field strength should be varied depending on the particle size since the magnetic moment μ_m changes dramatically depending on the particle size. Therefore, the slope of M/M_S vs. B was fitted within different magnetic field strength ranges (Fe_3O_4, 16.3 nm: –2 2 mT, 20.5 nm: –1 1 mT, 25.2 nm: –0.5 0.5 mT and 31.2 nm: –0.4 0.4 mT).

For cobalt doped ferrite ($Co_xFe_{3-x}O_4$) nanoparticles, M_S was determined from the Vegard's Law, which follows a linear regression line between $M_S^{Fe_3O_4}$ and $M_S^{CoFe_2O_4}$.[85] ($Co_xFe_{3-x}O_4$, x=0.01: -0.5 0.5mT, x=0.03: -0.4 0.4mT, x=0.12: -1.1mT 1.1mT, x=0.24: -2 2mT).

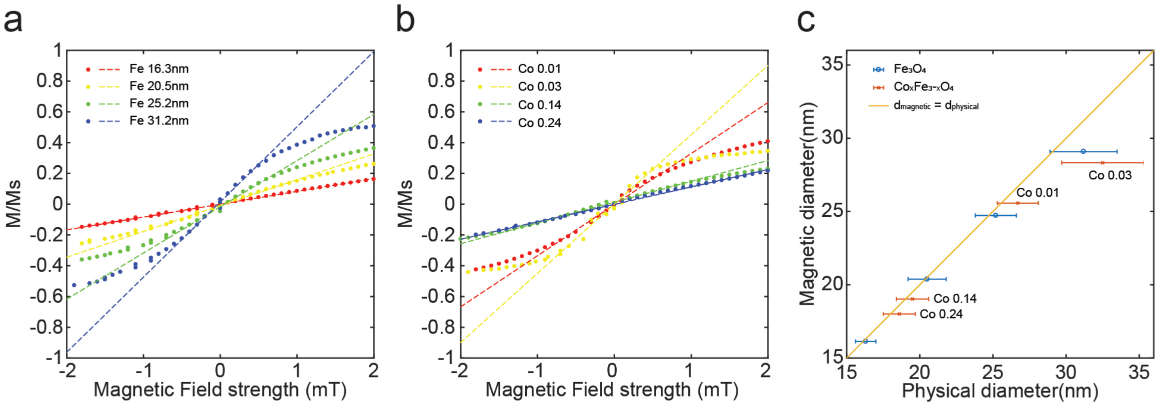

Figure 4-3: **Magnetic and physical diameter of MNP ensembles.** VSM profiles of magnetic moments vs. applied magnetic field for (a) Fe_3O_4 and (b) $Co_xFe_{3-x}O_4$. (c) Summary of MNP physical diameters obtained from TEM images and magnetic diameters calculated from VSM curves. Quantitative agreement between physical and magnetic diameters suggests that MNPs exhibit saturation magnetization values approaching those of bulk materials and therefore possess monocrystalline inverted spinel structure.

4.3.2 Dynamic hysteresis model for synthesized particles

For cobalt doped ferrite ($Co_xFe_{3-x}O_4$) nanoparticles, magnetic anisotropy does not vary linearly depending on Co^{2+} concentration.[85] In our dynamic hysteresis calculations, values of K of cobalt doped ferrite MNPs were estimated from literature.[85, 41] For particle distribution, 100 particles randomly produced along normal distribution with particle diameter average and standard deviation. The entered particle diameter average and standard deviation was from the histogram in Figure 4-3 (a-h) Specific loss power (SLP) and coercive field (H_C) of synthesized particles has been calculated with this dynamic hysteresis model and also again summarized in Figure 4-4 (f,h,i and l), next to measured SLP and H_C.

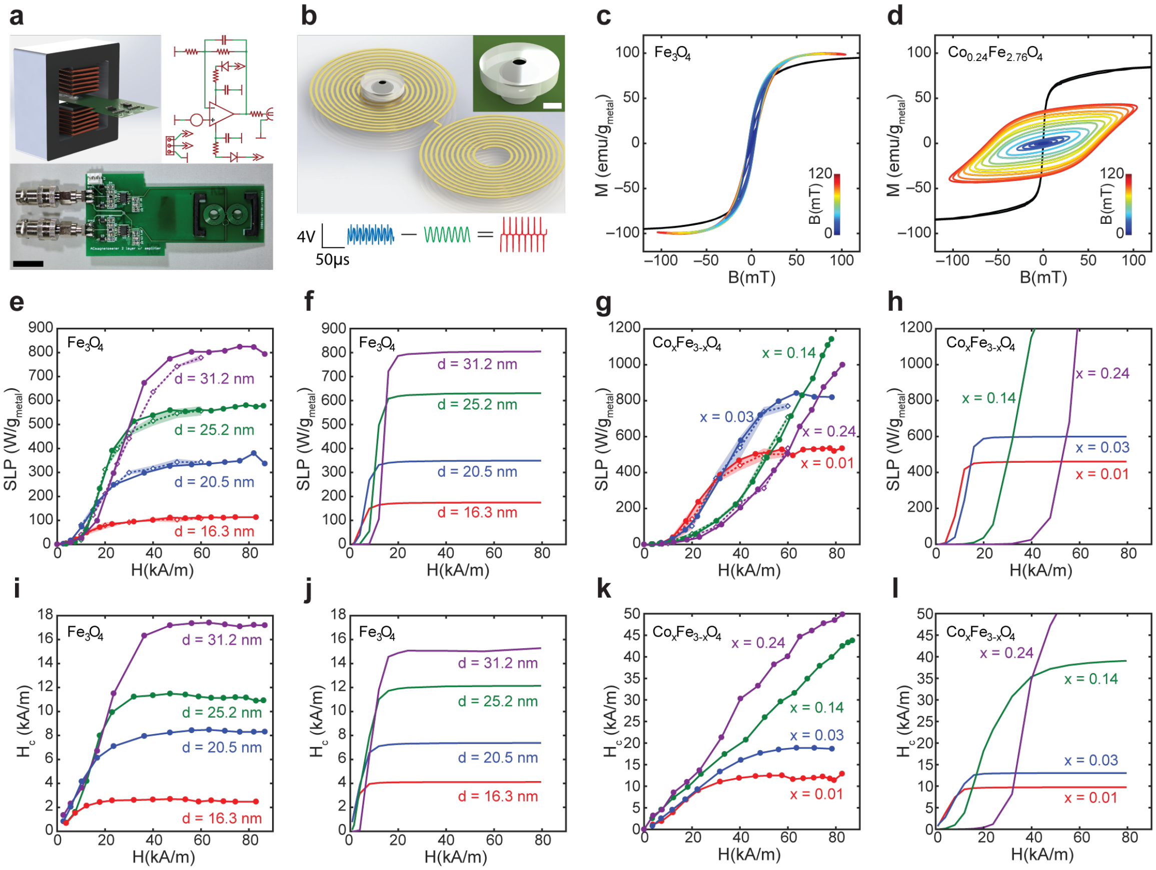

Figure 4-4: **Measurement of dynamic magnetization of MNP ensembles using custom high amplitude AC-magnetometer.** (a) Design, photograph, and circuit diagram of the custom AC-magnetometer (ACM) used to capture dynamic magnetization under AMF. (Scale bar = 1 cm). (b) 2D coil design to detect dynamic magnetization. The spiral design of the sense coil results in a voltage induced by the changing magnetization of the sample. The compensation coil wound in the opposite direction cancels the majority of the voltage induced by the driving AMF. Ferrofluid is loaded into the 3D printed hollow spherical chamber of the sample holder. (Scale bar: 1 mm) (Blue – raw sample signal, Green – water control sample signal, Red – net sample signal). (Scale bars: voltage = 4 V, time = 50 μs). (c, d) Dynamic hysteresis loops for ferrofluids of 16.2 nm Fe_3O_4 (c) and 16.3 nm $Co_{0.24}Fe_{2.76}O_4$ (d) were collected at room temperature under AMFs with $f = 75$ kHz and amplitudes ranging 0-120 mT. (Black line represents VSM data, jet color lines correspond to ACM data). (e-h), Specific loss power (SLP) of MNP ensembles measured empirically via ACM (e, g – solid lines, closed circle markers, measured at 75 kHz and linearly scaled by frequency to 101.2 kHz) and calorimetry (e, g - dashed lines, open diamond markers, shadowed areas represent standard deviation, measured at 101.2 kHz), and calculated via dynamic hysteresis model (f, h). (i-l) Coercive fields H_C for MNP ensembles calculated from ACM measurements (i, k) and simulated via the dynamic hysteresis model (j, l).

4.3.3 Biocompatibility of iron oxide nanoparticles

To evaluate the potential of magnetothermal multiplexing as a means to independently control cell signaling, we first corroborated the biocompatibility of our ferrofluids in cultures of HEK293FT cells (Figure S4-5). HEK293T cells were grown in 24-well plates in 10% Fetal bovine serum (FBS) + Dulbecco's modified eagle's medium (DMEM) up to 50% coverage. Cell medium was replaced on day1 and day2 with 1ml MNP solution (100ugMetal/ml in 10% FBS + DMEM) and 100μl alamarBlue assay. Cultures were incubated for 24 hr each, then medium was collected for spectrometry. Each condition had 4 wells.

4.3.4 Structural characterization

Powder x-ray diffraction data were collected using Bruker-AXS Smart Apex charged-coupled device (CCD) detector with graphite monochromated Mo K radiation (= 0.71073 Å) for the structure of Fe3O4 and Co-doped Fe3O4. TEM images were collected by FEI Tecnai on an amorphous carbon TEM grid. For hydrophobic ligand attached particles were diluted to 5 $\mu g/ml$ from its original solution using hexane. 7 μl of diluted solution dropped to TEM grid and dried. To remove any other residue from the grid, ethanol and hexane were repeatedly dropped three times and soaked the solution with Kim wipes.

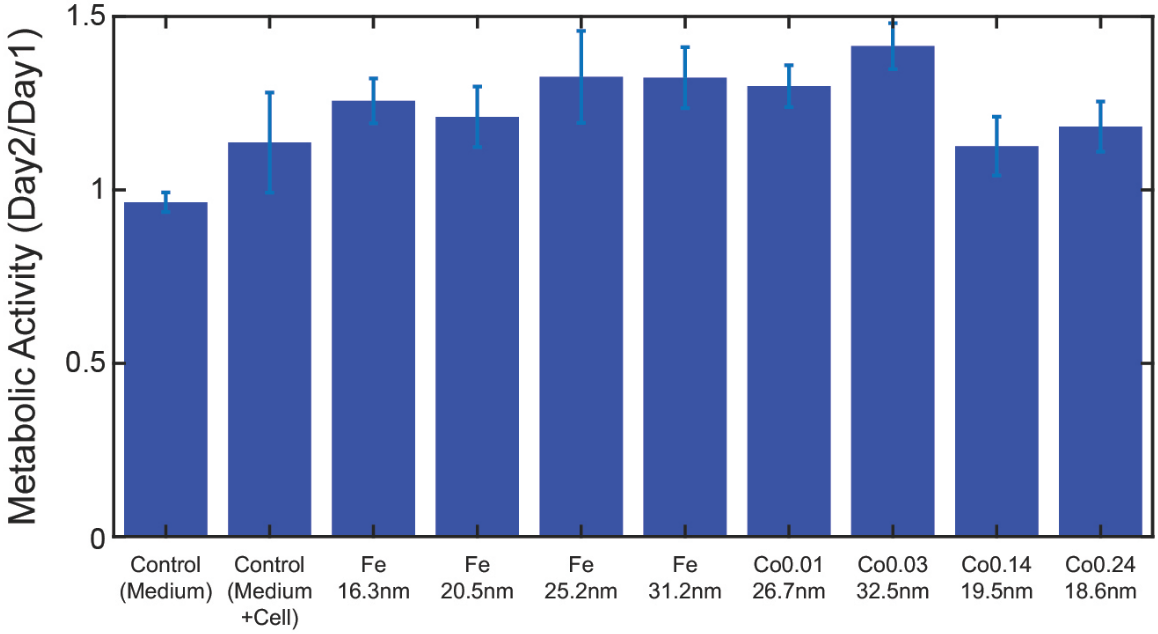

Figure 4-5: **Biocompatibility of magnetic nanoparticles in HEK239T cell cultures.** Proliferation of HEK293T in ferrofluid media was tested by Alamar Blue assay. Each well was tested without MNPs on day 1 and with MNPs on day 2. (Number of samples n=4, error bars represent standard deviation).

4.4 Optimization process of magnetothermal multiplexing

4.4.1 Multiplexing factor (MF) for selecting AMF conditions

We analyzed AC magnetometry data to identify the AMF conditions most suitable for magnetothermal multiplexing with the selected MNP ensembles. Multiplexing requires not only that each ferrofluid should heat up effectively in one AMF condition, but also that it dissipates minimal heat in the other AMF condition. To quantitatively evaluate selectivity, we defined the ratio of specific loss powers of a particular MNP ensemble at different AMF conditions as Selectivity (S). If MNP_1 is the low-K_{eff} MNP (less coercive), intended to dissipate more heat in AMF_1 with low amplitude

(H_1) and high frequency (f_1) than in AMF_2 with high amplitude (H_2) and low frequency (f_2), while high-K_{eff} MNP_2 (more coercive) will generate more heat when exposed to AMF_2, then S can be formulated as:

$$S_{MNP_1}(H_1, f_1, H_2, f_2) = \begin{cases} \dfrac{SLP_{MNP_1}(H_1, f_1)}{SLP_{MNP_1}(H_2, f_2)} & \text{for } H_2 > H_1 \text{ and } f_2 < f_1 \\ 0 & \text{Otherwise} \end{cases} \tag{4.1}$$

$$S_{MNP_2}(H_1, f_1, H_2, f_2) = \begin{cases} \dfrac{SLP_{MNP_2}(H_2, f_2)}{SLP_{MNP_2}(H_1, f_1)} & \text{for } H_2 > H_1 \text{ and } f_2 < f_1 \\ 0 & \text{Otherwise} \end{cases} \tag{4.2}$$

S is set to 0 for AMF pairs for which both amplitude and frequency of one condition exceed the other, because MNPs in the dominant AMF will always dissipate more heat than the other AMF, which runs contrary to the purpose of magnetothermal multiplexing. S of the ferrofluid of MNP_1 can be maximized under conditions in which low-amplitude, high-frequency AMF_1 allows access to the major hysteresis loops of the material and cycles rapidly enough to produce substantial heat dissipation. Conversely, the high-amplitude, low-frequency AMF_2, while also sufficient in magnitude to drive major hysteresis loops for MNP_1, cycles through these loops at a significantly lower rate and hence results in lower heat dissipation. In contrast, the ferrofluid of MNP_2, with its higher coercivity dissipates negligible heat in low-amplitude, high-frequency AMF_1, which is insufficient to access its major hysteresis loops, but exhibits large hysteresis loop area at high-amplitude, low-frequency AMF_2. Simply multiplying S_{MNP_1} and S_{MNP_2} may seem to be an expedient approach to define the overall multiplexing selectivity for this materials pair. However, this can misleadingly identify AMF_1 and AMF_2 conditions in which particularly high selectivity for one MNP ensemble veils the far less selective operation of the other MNP ensemble. To avoid such scenarios, we introduce Equity (E), defined as a ratio of the geometric and arithmetic means:

$$E = \frac{\sqrt{S_{MNP_1} \cdot S_{MNP_2}}}{\frac{S_{MNP_1} + S_{MNP_2}}{2}} \tag{4.3}$$

This quantity ranges between 0 and 1 and approaches 1 as S_{MNP_1} and S_{MNP_2} values approach each other, producing the exclusion of AMF conditions (H_1, f_1, H_2, f_2) that yield imbalanced S_{MNP_1} and S_{MNP_2}. An overall Multiplexing Factor (MF) is then defined as:

$$MF(H_1, f_1, H_2, f_2) = S_{MNP_1} \cdot S_{MNP_2} \cdot E = 2\frac{(S_{MNP_1} \cdot S_{MNP_2})^{3/2}}{S_{MNP_1} + S_{MNP_2}} \tag{4.4}$$

4.4.2 Finding Pairing AMF Condition

Since differing coercivity is the basis for multiplexing in this material system, we began by selecting the two batches of magnetic nanoparticles that showed the largest difference in coercivity. To find optimized multiplexed condition, we introduced a $multiplexingfactor(MF)$, which depends on four parameters $(H_1, f_1, H_2, f_2$, where H_x and f_x are amplitude and frequency of AMF_x, respectively). $MF(H_1,f_1,H_2,f_2)$ H_x-Field amplitude of AMF_x, f_x - frequency of AMF_x Since these four parameters can

	a	**b**	**c**	**R-square**	**RMSE**
MNP_1	1180	-0.08	62.19	0.9671	7.5426
MNP_2	112.4	-0.12	16.42	0.9980	16.8423

Table 4.1: Curve fitting results for SLP data of MNP1 and MNP2 collected using the AC magnetometer.

vary independently, in the most general case they define a four-dimensional parameter space over which varies. To find optimally paired AMF conditions, parameters that maximize should be identified. Hysteresis loops do not vary markedly with frequency for MNPs driven by AMFs in the frequency range of interest. [70, 71, 73, 88] This has two notable consequences: 1) A reduced three dimensional parameter space is possible in terms of H_1 , H_2 , and the ratio f_1/f_2. 2) It is feasible to determine SLP versus amplitude curves for MNP_1 and MNP_2 throughout this space based on characterization at one frequency. We took the further step of fitting these curves with analytical functions using a non-linear least square fit. (The logistic functions assumed for this fit do not have any physical meaning but converged well to the data and offered simple analytic expressions for scanning over parameters.) (Figure 4-6 and Table 4.1)

$$SLP(H) = \frac{a \cdot 1}{1 + e^{-b \cdot (H-c)}} (a, b \text{ and } c \text{ are constants}) \tag{4.5}$$

A global maximum for preliminary MF subject to these constraints was determined for H_1 = 11.1 kA/m, H_2 = 70 kA/m, and f_1/f_2 = 10.72. From this result, AMF

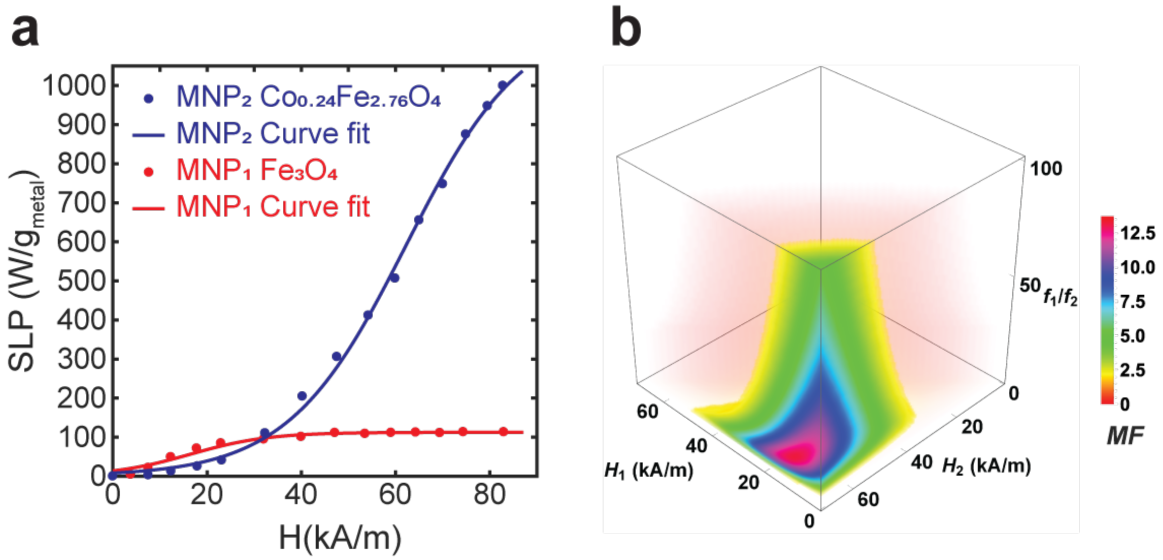

Figure 4-6: **Search for preliminary AMF conditions for magnetothermal multiplexing using analytically expressed multiplexing factor** (a) curve fit results for Fe_3O_4 16.3nm and $Co_{0.24}Fe_{2.76}O_4$ 18.6 nm MNPs. (b) Parametric scanning plot of Multiplexing Factor over field amplitudes (H_1 and H_2) and frequency ratio (f_1/f_2) to determine preliminary AMF conditions.

generator was built to have frequency pairs, 522 kHz and 50 kHz ($f_1/f_2 = 10.44$), where all chosen AMF conditions exhibit amplitude-frequency products near or below AMF safety limit. ($H \cdot f < 5 \times 10^9 Am^{-1} \cdot s^{-1}$)[82] To determine final AMF conditions for multiplexing, $MF(H_1$, 522 kHz, H_2, 50 kHz) constructed out of SLP profile from AC magnetometer was scanned over AMF amplitudes space. (H_1 and H_2) (Figure **??** and 4-7) From this scanning, final AMF conditions were set to H_1=10 kA/m, f_1=522 kHz and H_2=70 kA/m, f_2=50 kHz.

4.5 Selective heating of ferrofluid droplets alone

Before bringing the multifplexed magnetothermal system to selective cellular signaling, selectivity of magnetothermal system tested first. We verified that the MNP_1

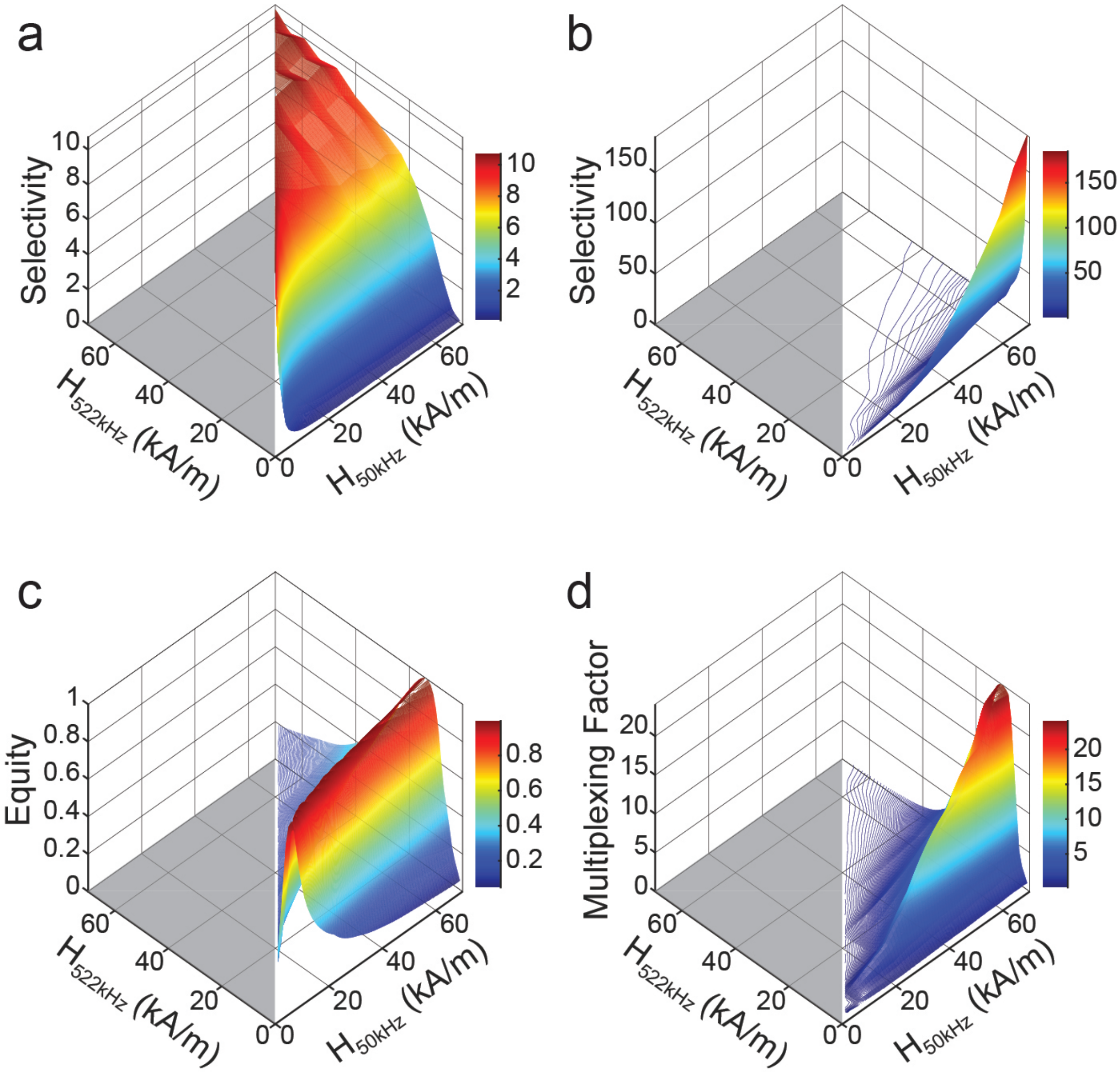

Figure 4-7: **Parameter plots scanning over AMF amplitude space to optimize magnetothermal multiplexing conditions.** Grey area corresponds to inapplicable conditions (Selectivity, $S = 0$). (a) (b) Selectivity of (a)-Fe_3O_4 16.3nm and (b)-$Co_{0.24}Fe_{2.76}O_4$ 18.6 nm MNPs. (c) Equity between these two MNP ensembles. (d) Multiplexing Factor.

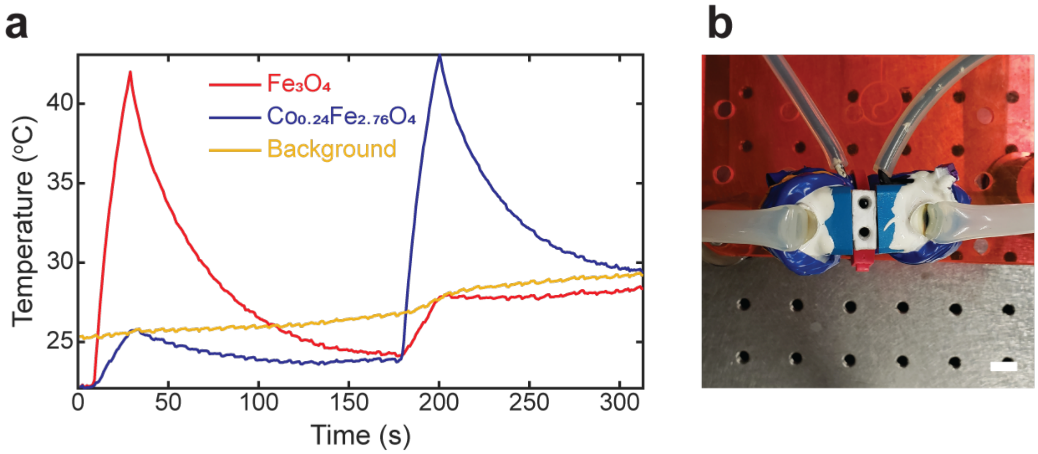

Figure 4-8: **Experiment demonstrating the selective heating of two neighboring ferrofluid droplets.** (a) Temperature profile of each droplet (Fe_3O_4 16.3nm and $Co_{0.24}Fe_{2.76}O_4$ 18.6 nm) and background (b) Top view of AMF generating torroid gap. (Scale bar 1 cm)

(20.2 mg_{Metal}/ml in water) and MNP_2 (10.5 mg_{Metal}/ml in water) could selectively respond to AMF_1 and AMF_2 by exposing their droplets (10 μl each) to either of the selected AMF conditions for 20 s. The temperatures of the solutions were recorded in real time using an infrared camera. As shown in Figure 4-9 (b), (c), Figure 4-8 1, each MNP droplet heats significantly ($\Delta T_{MNP1-AMF1} \approx 19.6\ ^oC$, $\Delta T_{MNP2-AMF2} \approx 18.6\ ^oC$) only when exposed to its paired AMF.

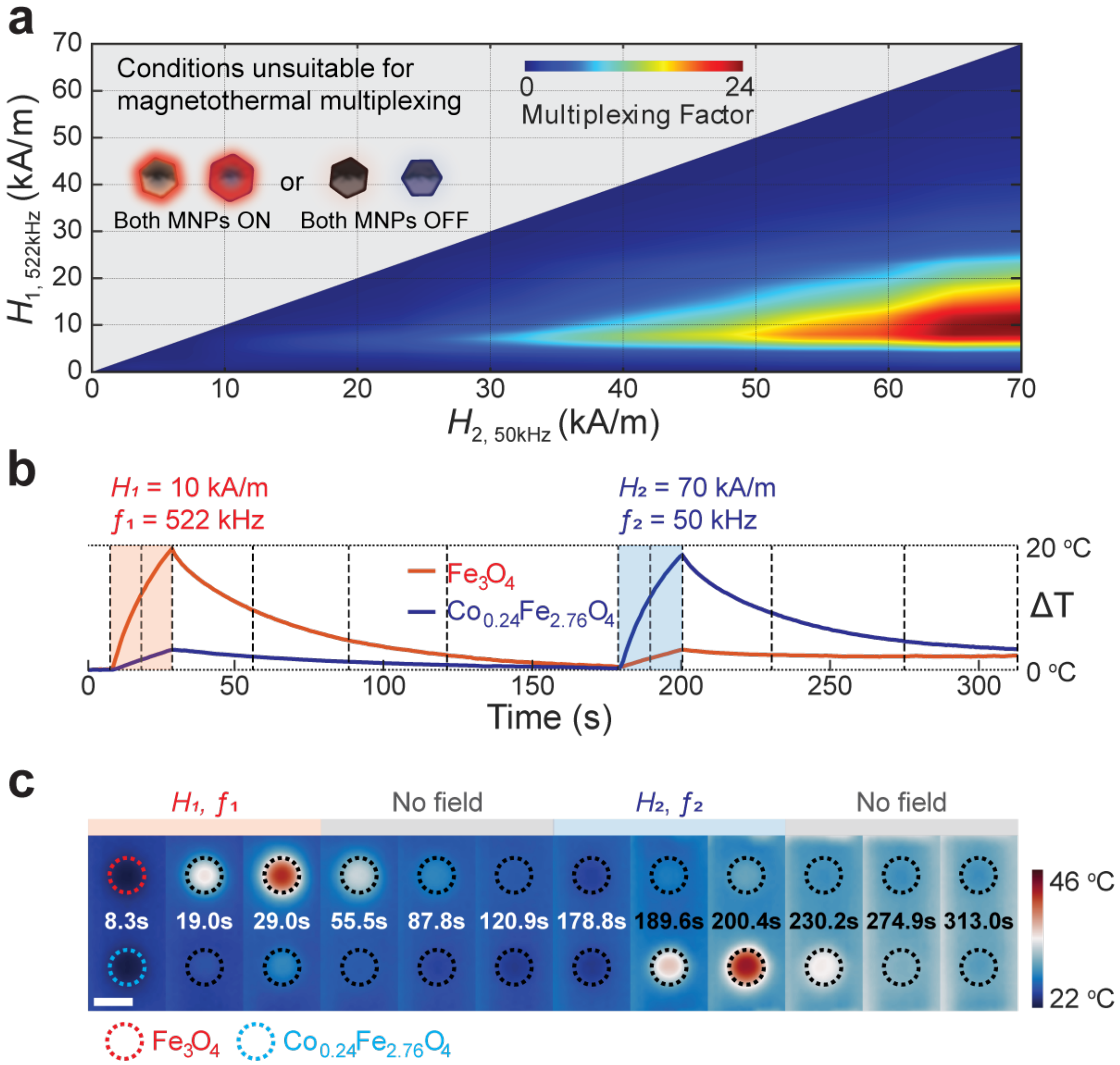

Figure 4-9: **Optimization of field conditions and thermographic verification for multiplexed thermal control** (a) Multiplexing factor as a function of AMF amplitudes H_1 and H_2, for frequencies f_1=522 kHz and f_2=50 kHz. The grey area represents excluded conditions $H_1 > H_2$; a pair of AMFs in which both the amplitude and frequency of one condition is higher than the other is unsuitable for magnetothermal multiplexing. (b) Temperature profiles and (c) Thermographic images of two 10 μl MNP solution droplets (Fe_3O_4 16.3 nm - red and $Co_{0.24}Fe_{2.76}O_4$ 18.6nm - blue) exposed sequentially to two distinct AMFs for 20 s (70 kA/m, 50 kHz and 10 kA/m, 522 kHz), at each time frame. Dashed lines in temperature profiles (b) represent the times of the thermographic frames in (c). (Scale bar = 5 mm)

4.6 Demonstration of Selective cellular signalling control on HEK cells

To evaluate the potential of magnetothermal multiplexing as a means to independently control cell signaling, we first corroborated the biocompatibility of our ferrofluids in cultures of HEK293FT cells (Figure S4-58). We then applied multiplexed magnetothermal control to HEK293FT cells co-transfected with heat-sensitive cation channel TRPV1 and a calcium indicator GCaMP6s (Figure **??**a-c). These cells, prepared on glass coverslips coated with Matrigel®, were submerged within dilute ferrofluids of MNP_1 (6.6 mg_{Metal}/ml in Tyrode's solution) or MNP_2 (3.8 mg_{Metal}/ml in Tyrode's solution) and exposed to the AMF_1 and AMF_2. To eliminate the possible influence of variability in response between different cell populations, each sample was first exposed to its unpaired AMF condition predicted to yield negligible heating of the ferrofluid, followed by exposure to the paired AMF known to produce efficient heat dissipation in the given MNP solution. GCaMP6s fluorescence dynamics within cell populations (n=100 cells from 8 coverslips per ferrofluid) were recorded over the entire experiment duration using an inverted fluorescence microscope.

Thermal triggering of TRPV1 was expected to induce intracellular Ca^{2+} influx, [27, 89] which was observed via a change in GCaMP6s fluorescence (ΔF) for each cell within a field of view normalized to its initial background fluorescence (F0). Consistent with the temperature changes in the surrounding ferrofluids, a strong response was observed only when the AMF conditions were optimized for the given MNP (Fig-

Field condition	AMF_1 (522 kHz, 10 kA/m)		AMF_2 (50 kHz, 70 kA/m)	
Particle	MNP_1	MNP_2	MNP_1	MNP_2
AC magnetometer	203 W/g_{Metal}	50 W/g_{Metal}	53 W/g_{Metal}	369 W/g_{Metal}
Thermographic recording	206 W/g_{Metal}	59 W/g_{Metal}	43 W/g_{Metal}	368 W/g_{Metal}
In vitro.	202 W/g_{Metal}	65 W/g_{Metal}	47 W/g_{Metal}	369 W/g_{Metal}

Table 4.2: The SLP summary table for multiplexed magnetothermal experiments

ure **??**d-g). When exposed to AMF_1, MNP_1 solutions increased in temperature by 6.4 ^oC, reaching T=43.6 ^oC in 20 s, triggering Ca^{2+} influx through TRPV1 and significantly increasing GCaMP6s fluorescence (Figure **??** d). In contrast, exposure of MNP_1 ferrofluid to AMF_2 increased the temperature by only 1.5 ^oC, which was insufficient to trigger TRPV1 (Figure **??** e). Conversely, MNP_2 ferrofluid exhibited negligible heating of 1.2 ^oC upon exposure to AMF_1, insufficient to excite Ca^{2+} influx within the submerged cell populations (Figure **??** f). Exposure to AMF_2 evoked a temperature increase of 6.6 ^oC (to T=43.8 ^oC in 20 s), which triggered TRPV1 opening, Ca^{2+} influx, and an increase in GCaMP6s fluorescence in 67% of analyzed cells (Figure **??** g).

While our ability to simultaneously expose two cell populations to both AMFs was limited by our experimental apparatus, our in situ measurements (Figure **??**) and modeling results (Figure 3-6) suggest that the selective response of the cells surrounded by the distinct ferrofluids to their paired AMF conditions is a viable means of multiplexed magnetothermal control of organ regions.

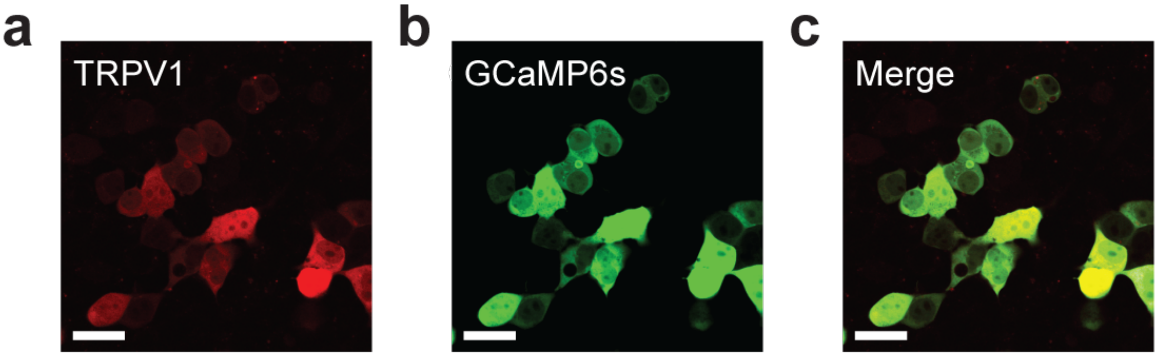

Figure 4-10: **Confocal Images of HEK293T cells** Each expression is represented by (a-c) Confocal images of HEK293T cells co-transfected with both TRPV1-p2A-mCherry (a, c) cytoplasmic mCherry expression) and GCaMP6s (b, c). (Scale bar = 25 μm).

4.7 Outlook for multiplexed magnetothermal control in biomedical applications

This work has demonstrated a nanomaterials-based approach to selectively heat MNP ensembles with distinct magnetic properties. Our strategy relied on manipulating coercivity by controlling particle size and cobalt incorporation into magnetite. A methodology to determine suitable AMF conditions was implemented, relying on a custom-designed high amplitude AC magnetometer that revealed dynamic magnetization behavior and provided a basis for empirical extrapolation. The utility of the selected materials was shown in vitro as a means to independently evoke intracellular Ca2+ influx into heat-sensitized cell populations surrounded by distinct ferrofluids with paired AMF conditions. While we chose control of cell signaling as a testbed, the approach and underlying principles are generalizable to numerous applications employing MNP ensembles as heat sources. This includes sequential release of pharmacological compounds in multiple target regions or stimulation of multiple

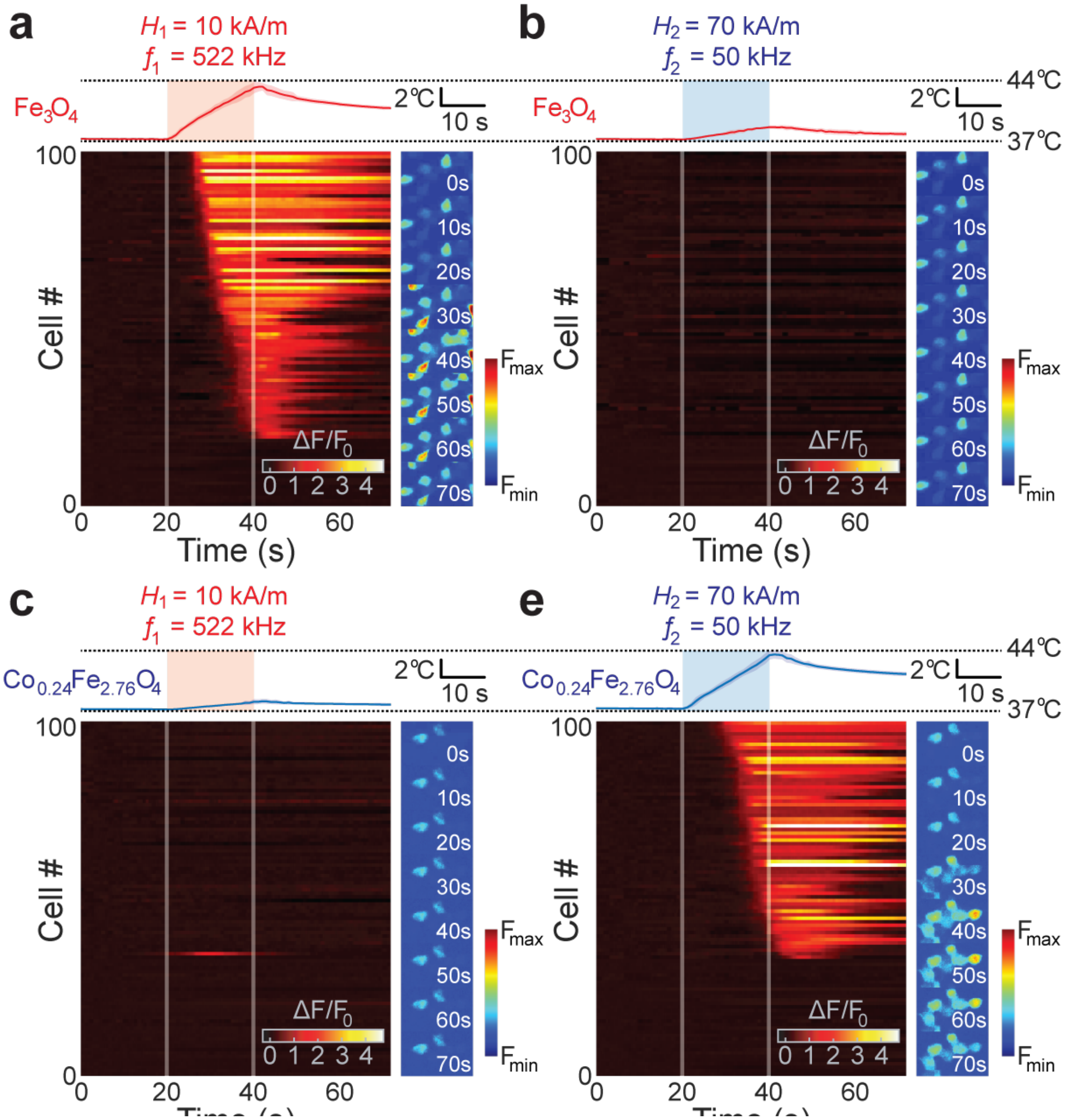

Figure 4-11: **Cellular responses selectively triggered by multiplexed magnetothermal control** (a-d) Cellular responses to multiplexed magnetothermal heating. Temperature profiles (upper plots) of the ferrofluids and the normalized GCaMP6s fluorescence ΔF/F0 (lower heat maps) of 100 randomly automatically chosen HEK239T cells plotted within the same time frame (0-70 s). Side panels indicate normalized GCaMP6s fluorescence images of the cells at different time-points during the experiments. (Scale bars = 40 m). For each ferrofluid, the non-pairing AMF was applied at first. Afterward the same field of view (FOV) was imaged when cells were exposed to the pairing AMF. Each ΔF/F0 profile is from same FOV for each cover slip. AMFs were applied for 20 s (color boxes in temperature profiles and white lines in heat maps: from 20 s to 40 s). (a) Fe_{3O4} at 10 kA/m 522 kHz AMF. (b) Fe_{3O4} with 70 kA/m 50 kHz AMF. (c) $Co_{0.24}Fe_{2.76}O_4$ with 10 kA/m 522 kHz AMF. (d) $Co_{0.24}Fe_{2.76}O_4$ with 70 kA/m 50 kHz AMF.)

sub-structures of organs including the nervous system.[90, 91] Various alternative synthetic routes to MNPs with differing coercivities are available. For instance, a recent study on magnetosomes that are ultimately converted by stem cells to smaller magnetite particles may suggest a means to selectively modulate cells based on their metabolic processes.[92] For applications in which it is challenging to superimpose a magnetostatic field to achieve spatial selectivity of thermal modulation,[93] such as in moving objects or in freely behaving subjects, magnetothermal multiplexing may offer an attractive alternative for selective heating of MNP ensembles.

Chapter 5

Selective Modulation on Cellular Signalling via Drug Releases Triggered by Multiplexed Heating of MNPs

5.1 Backgrounds and Motivation

Nanotechnology has offered novel designs and concepts for drug delivery. As drugs can sometimes be toxic or lose their functionality when they meet unintended tissues or organs, the release of encapsulated materials remotely is desired in drug delivery. Liposomes are one of the most common and well-investigated nanocarriers for targeted drug delivery. Liposomes have already been used as drug-delivering carriers, and they are the first nanoscale drugs approved for clinical use in 1995.[94] Liposomes are known to enhance drug delivery efficiency by stabilizing therapeutic compounds, dodging obstacles to cellular and tissue uptake, and improving homogenized biodistribution of drug compounds. [95] Some researchers took one step further from this and combined with gold nanoparticles or magnetic nanoparticles as heat transducers to induce active drug delivery.[96, 97, 98, 91]

In this context, we designed a chemo-magnetic drug delivery system that consisted of thermally responsive (MNP-loaded) liposomes composed of a mixture of the 1,2-dipalmitoyl-sn-glycero-3-phosphocholine (DPPC) and 1,2-distearoyl-sn-glycero-3-phosphocholine (DSPC) lipids and cholesterol in a 10:5:3 weight ratio showing a phase transition temperature at 43 ^oC.[38] Here, we demonstrated the control of specific neurons and VTA with temporal and spatial precision and optically confirmed their responses.(Figure5-1) We further applied this chemomagnetic approach to withdraw changed behavioral and social responses from mice.(Figure5-2)

Following this research, the next step was combining selective heating of MNPs to these chemomagnetic liposomes to enable explicit drug release to different (or same) targets to obtain more detailed and controlled responses from the target. This concept is well presented in Figure5-3.

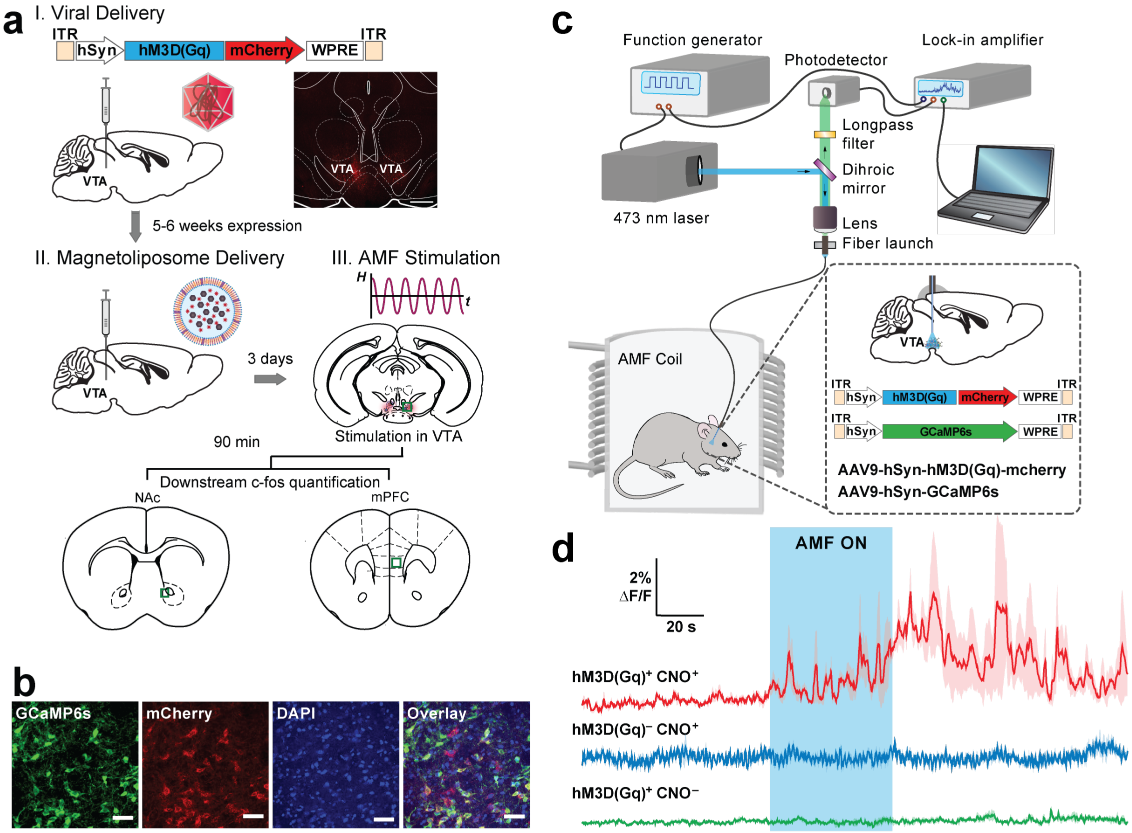

Figure 5-1: **Chemomagnetic stimulation in vivo** (a) Experimental timeline for the viral gene delivery (i), magnetoliposome injection (ii) and AMF stimulation (iii). Inset: a confocal image of the expression of hM3D(Gq)-mCherry in the mouse VTA. (b) Confocal images of the co-expression of GCaMP6s and hM3D(Gq)-mCherry in the mouse VTA. The experiment was repeated three times independently with similar results. Scale bars, $50\mu m$. (c) Photometry set-up integrated with an AMF coil. (d) Normalized dynamic fluorescence intensity change ($\Delta F/F_0$) of GCaMP6s in the VTA of mice freely moving within the AMF coil. A fluorescence increase was observed only on applying AMF stimulation in mice express hM3D(Gq) and injected with CNO-loaded magnetoliposomes (red). The blue area represents the AMF exposure. In all the experiments, $H_0 = 45 \pm 2mT, f = 164kHz$. Solid lines, mean; shaded areas, s.e.m., n = 3 mice for each test condition. ITR, inverted terminal repeat; ROI, region of interest; WPRE, woodchuck hepatitis virus posttranscriptional regulatory element. Reprinted from Rao, S. et al. [38]

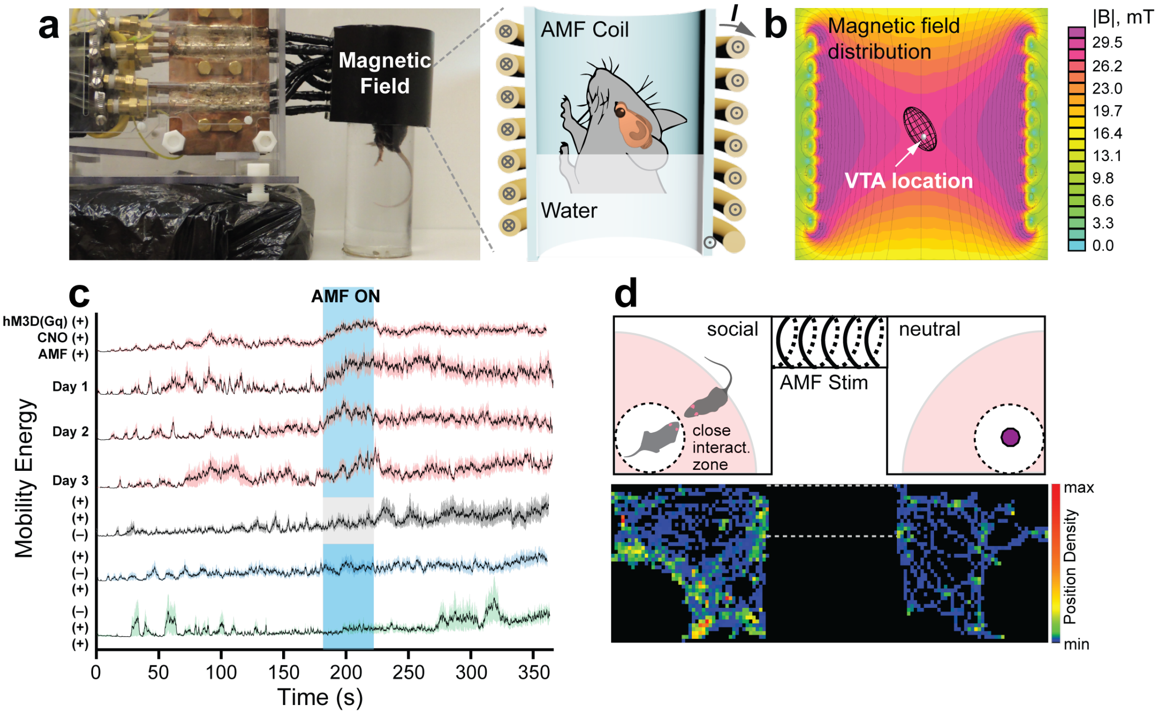

Figure 5-2: **Remote chemomagnetic modulation of mouse behaviour and social preference using chemogenetics.** (a) A photograph and schematic of the FST assay within an AMF coil. (b) The mouse VTA was situated within the region of the uniform AMF by adjusting the swimming tank water level. The colour map represents the cross-sectional view of the magnetic flux distribution as calculated by a finite element model for the AMF coil. (c) Averaged motion energy curves for mice undergoing FST. The energy was calculated from the pixel changes in each frame of the FST videos. Solid lines, mean; shaded areas, s.e.m. $H_0 = 45 \pm 2mT, f = 164kHz$. The blue area represents AMF exposure and the grey area indicates the absence of an AMF. n, number of test trials (which is the same as the number of subjects for the day 1–3 data, where one subject was tested per trial). (d)Top: the experimental scheme for the mouse social preference test with an AMF coil that encompasses the middle chamber. The shaded radial area within the test chambers (90% of the chamber length and width) was defined as the close interaction zone. Bottom: a representative heat map that traces the position of a mouse in social subject and novel object chambers during the preference test. Reprinted from Rao, S. et al. [38]

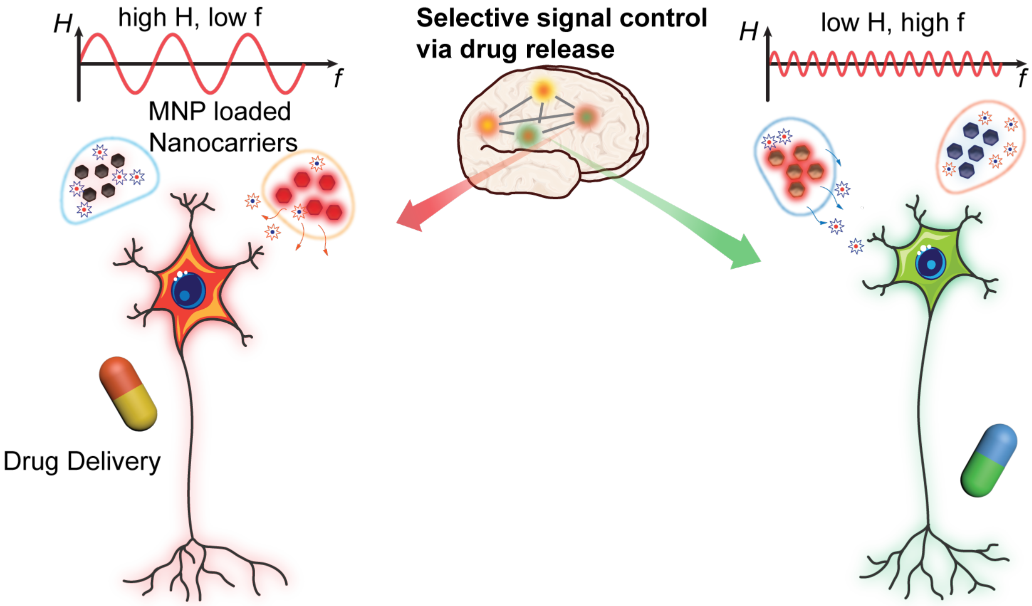

Figure 5-3: **Schematic overview of selective modulation of cell signaling using selective drug release triggered by multiplexed magnetothermal control** Two different magnetic nanoparticles are encapsulated by liposomes with different drugs. Heat dissipation from the magnetic nanoparticles loosens permeability of the liposomal membrane and initiates drugs to be release to nearby receptors. Each magnetic particles responses specifically to pairing alternative magnetic fields.

5.2 Tuning of magnetic nanoparticles for multiplexed nanoscale heating

As shown in the previous Chapter 4, two distinctive magnetic nanoparticles (high K_{eff} and low K_{eff}) were synthesized through cobalt incorporation into octahedral sites of inverse spinel ferrite. For precise control over cobalt doping concentration and particle size distribution, which both affect magnetic anisotropy significantly, the organometallic decomposition method has been revisited. Synthesized particles had size distribution of 19.653 ± 0.921 nm for Fe_3O_4 and 28.980 ± 1.126 nm for $Co_{0.13}Fe_{2.87}O_4$.(Figure5-4 a and d) MNPs were phase transferred to water then measured dynamic hysteresis using the AC magnetometer. (Figure5-4 c and f)

5.3 Chemistry of Magnetoliposome

Unlike previous research, this project used synthesized MNPs. Oleic acid ligand on particle surface was exchanged with DMSA to prepare an aqueous ferrofluid. Then PEI was attached to DMSA coated MNPs using carbodiimide crosslinker chemistry. Phase transferred nanoparticles showed strong surface charge polarity coming from carboxyl group and amine group, as shown in Figure5-6 a. The existence of PEI on particle surface could be confirmed again with the FTIR spectrum in Figure5-6 b. Unlike an amphiphilic polymeric coating, ligand exchanged aqueous ferrofluid showed strong hydrophilicity and didn't lose the coating even after the harsh sonication during the double-emulsion process. Figure5-6 c. Pentane was mixed with

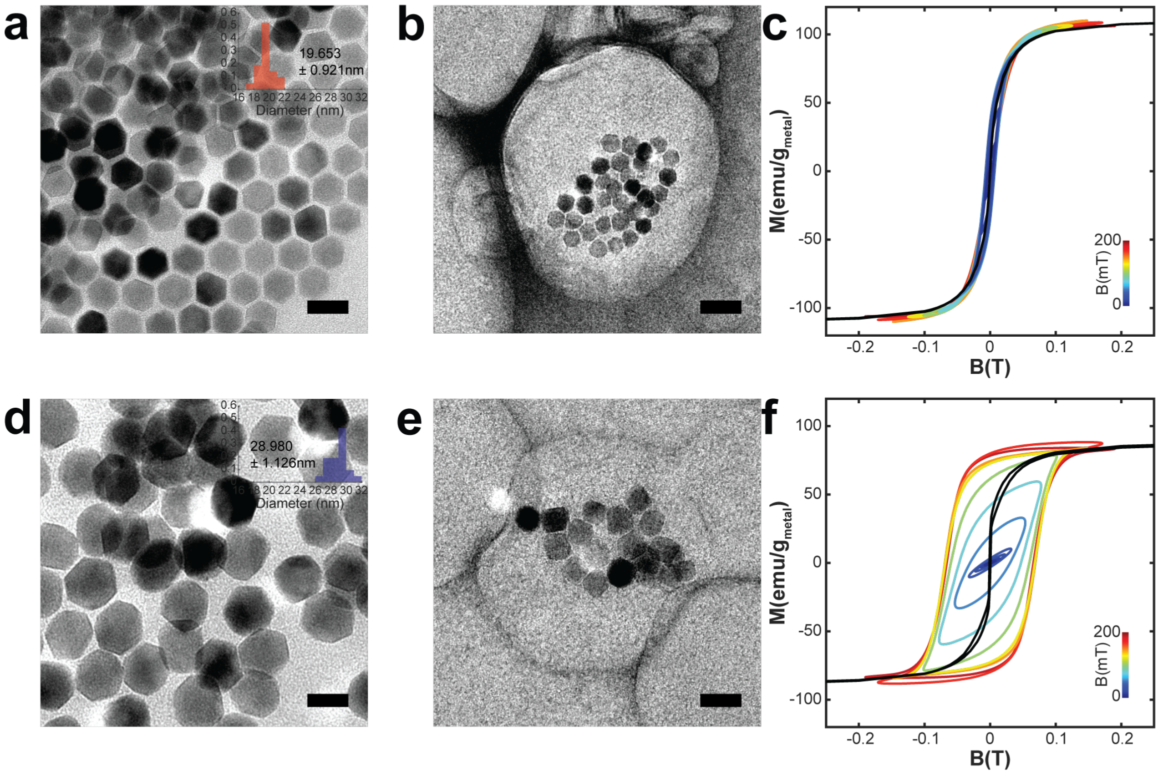

Figure 5-4: **Characterization of magnetic nanoparticles and magnetoliposomes** (a,b,d and e) TEM of Fe_3O_4 (a-d) and $Co_{0.13}Fe_{2.87}O_4$ (e-h) magnetic nanoparticles and their size distributions from TEM (inset histograms). (c and d) Dynamic hysteresis loops for ferrofluids of (c) 19.653nm Fe_3O_4 and (f) 28.980nm $Co_{0.13}Fe_{2.87}O_4$.

dichloromethane to have a density 1g/ml to enhance the emulsion's stability. The mixed organic solvent significantly reduced the emulsion's buoyant force and stabilized it much longer (30min) than the recipe that used dichloromethane alone. Later, MNPs and magnetoliposomes' size distributions were measured using DLS. (Figure5-6 d.)

To understand the dynamics and loading of drugs in the magnetoliposome cargo, two different fluorescent molecules (fluorescein sodium salt and Rhodamine B) have been used to confirm the selective release. As shown in Figure5-7 a, both molecules can emit fluorescent light near 425 nm and 585 nm. As there is overlap between the emission spectrum of fluorescein sodium and absorption spectrum of rhodamine B, the mixture intensity around 425nm becomes substantially decreased comparing to fluorescein solvent alone. However, the two peak intensity is still strong enough to detect the presence of the two molecules.

Also, a linear fitting line is drawn in Figure5-7 b and c. The deviation profile means there is a self-quenching effect. You can find the self-quenching is likely to happen for the solution having a higher concentration than 50 100 $\mu g/ml$. When the concentration goes even higher, overwhelming self-quench silences intensity even more. This self-quenching dominant regimes are marked as green and red arrows in the Figure. Fluorescent dye loaded magnetoliposomes were also aimed to have cargo concentration within this regime, and fluorescent sodium (20mg/ml) and rhodamine B (8mg/ml) stock solutions were used during the double emulsion process.

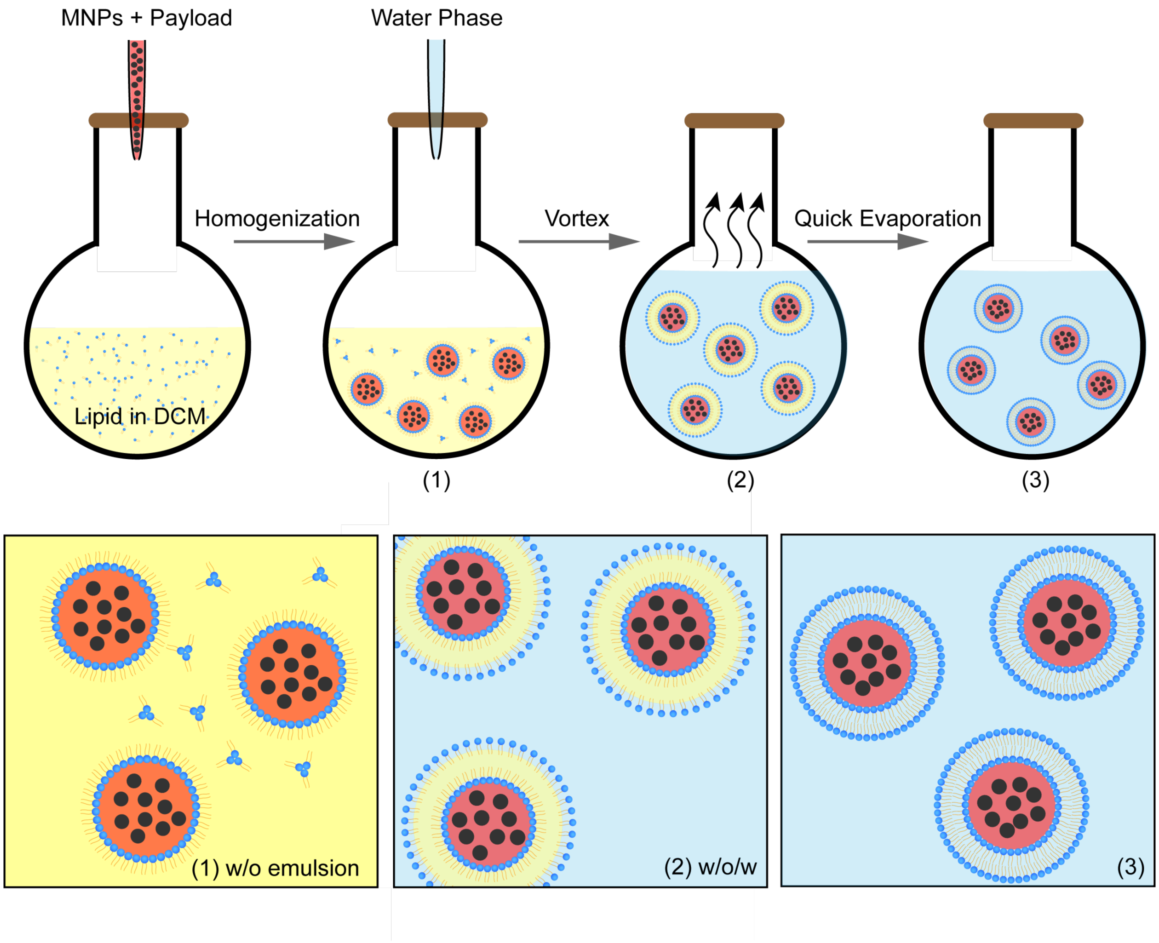

Figure 5-5: **Magnetoliposome synthesis via double-emulsion method** The aqueous solution of MNPs and payload was added into the mixtures of lipids that were dissolved in an organic solvent (dichloromethane, DCM). After homogenization, large volume of the second water phase was added, followed by vortex homogenization and rapid evaporation. Reprinted from [38]

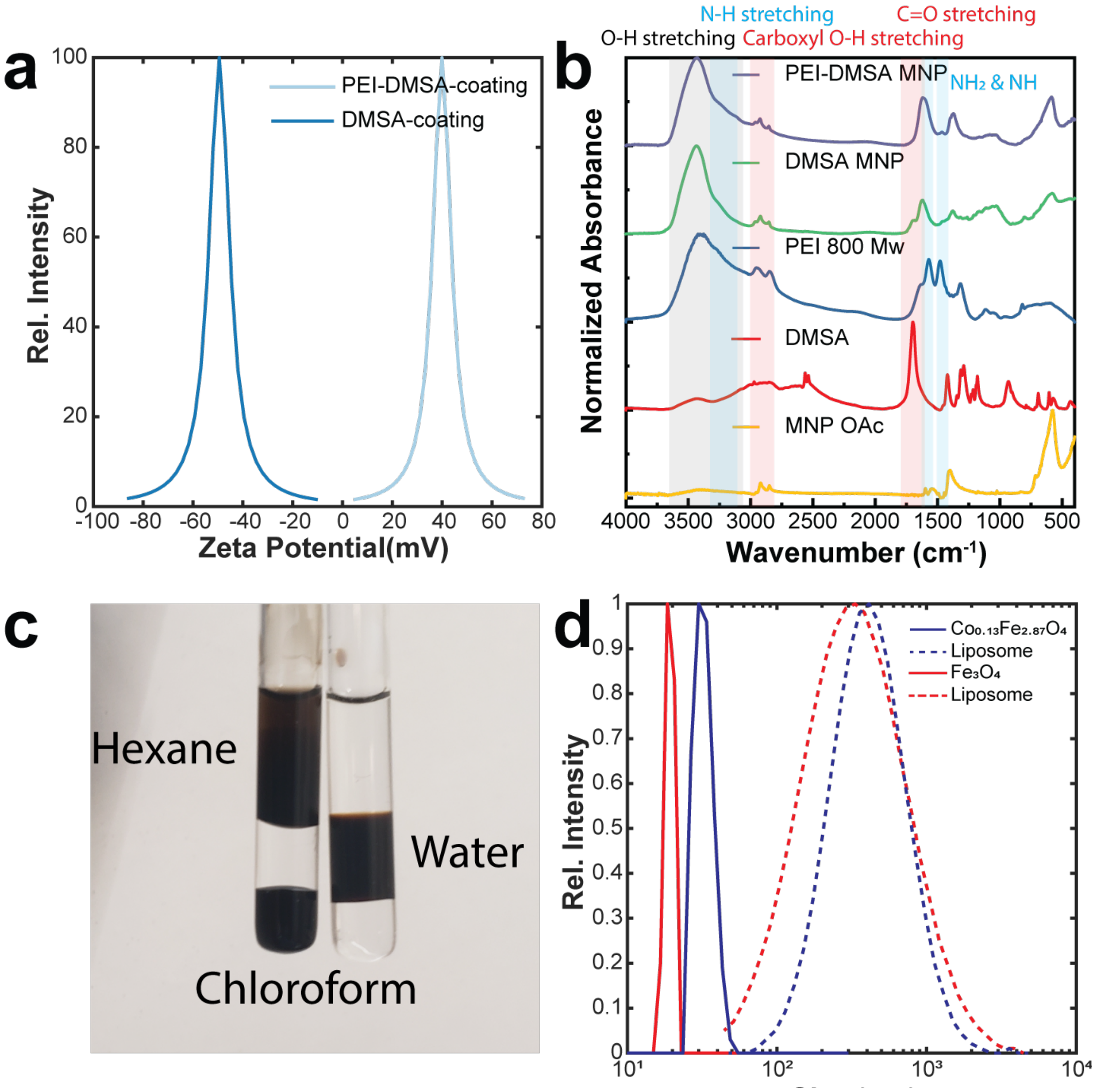

Figure 5-6: **Phase transfer of hydrophobic iron oxide nanoparticles for magnetoliposome synthesis** (a) Zetapotential of ligand exchanged iron oxide nanoparticles. (b) Fourier transform infrared spectroscopy (FTIR) of phase transferred particles, ligands and polymers sequentially exchanged and attached. (c) Before (left) and after (right) phase transfer. (d) The particle size distribution of magnetic nanoparticles and magnetoliposomes collected by Dynamic light scattering (DLS) intensity measurement

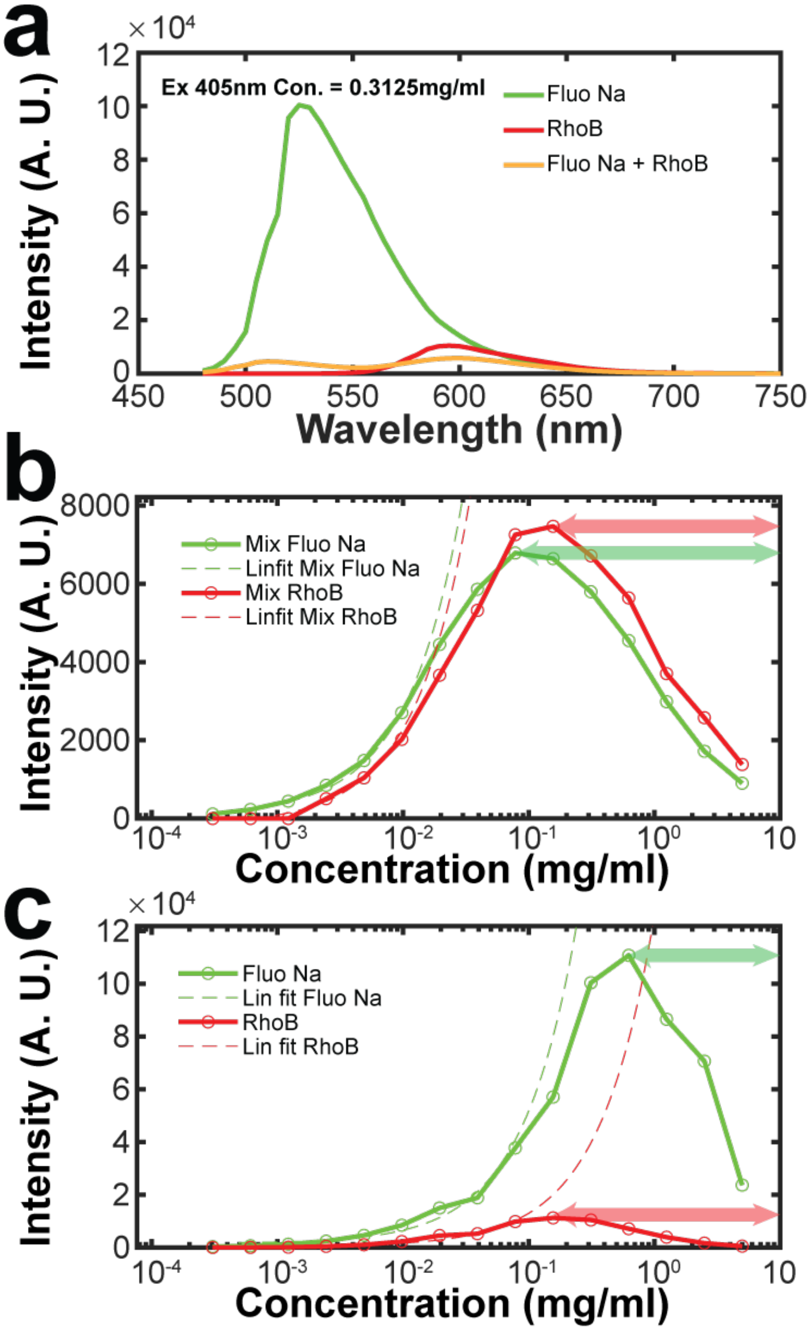

Figure 5-7: **Spectrum and intensity profile of fluorescein sodium and Rhodamine B** (a) Spectrum of fluorescein sodium, Rhodamine B and the mixure of the two dyes. In mixture, the emission of fluorescein is suppressed by Rhodamine B. (b) and (c) Intensity profile for different concentration of fluorescein sodium, Rhodamine B and the mixure. Each green and red arrows represents self quenching dominant concentration range. Linear fitting curves are drawn to have the RMSE less than 0.99. (Fluorescein sodium: Fluo Na, Rhodamine B: RhoB)

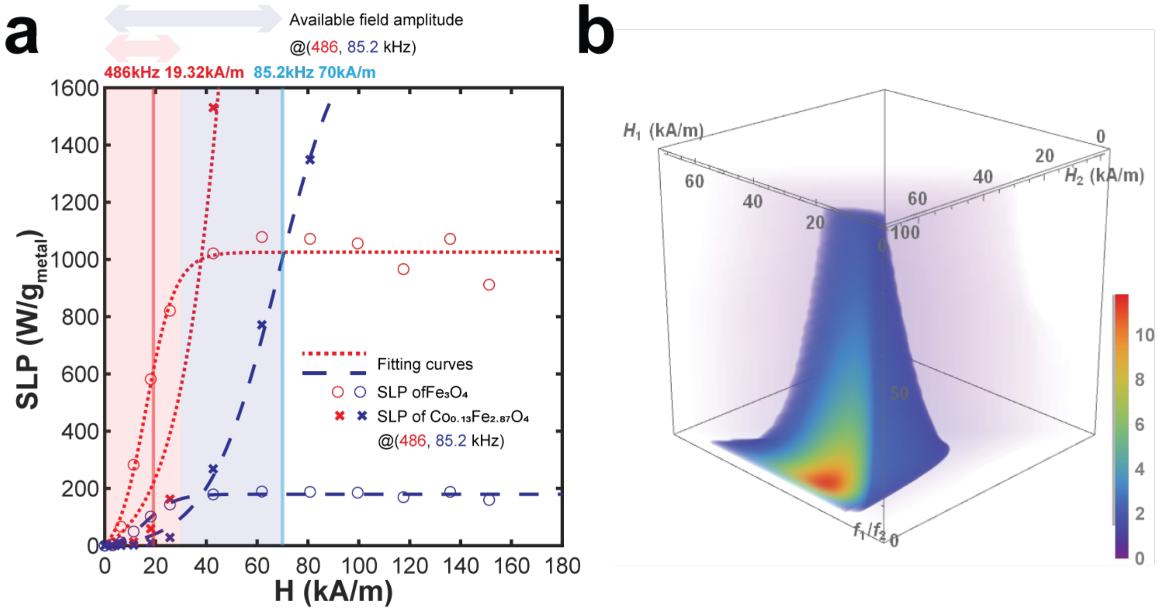

Figure 5-8: **Search for preliminary AMF conditions for magnetothermal multiplexing using analytically expressed multiplexing factor** (a) Extrapolated SLP profiles and curve fits of Fe_3O_4 19.653nm and $Co_{0.13}Fe_{2.87}O_4$ 28.980 nm MNPs at 486 kHz (red) and 85.2 kHz (blue). (b) Parametric scanning plot of Multiplexing Factor over field amplitudes (H_1 and H_2) and frequency ratio (f_1/f_2) to determine preliminary AMF conditions.

5.4 Optimization process of multiplexing

The hysteresis loops of MNPs were translated into SLP profiles and fed to Mathematica code to scan optimized field conditions for magnetothermal multiplexing. The fitting curve for SLP profiles are summarized in Table5.1. The optimized parameter was scanned using analytical curve fitting is listed in Table5.3. The frequency pair was selected to 486 kHz and 85.2 kHz. Expolated SLP profiles can read in Figure5-10 a. Each red and blue box represents accessible field amplitude range at the given frequency.

	a	**b**	**c**
Fe_3O_4	$2.23326584116345 \cdot f$	0.173769096095933	16.3598998792152
$Co_{0.13}Fe_{2.87}O_4$	$22.4242113518613 \cdot f$	0.0732640044644202	68.1674017327973

Table 5.1: Curve fitting results for SLP data of Fe_3O_4 and $Co_{0.13}Fe_{2.87}O_4$ collected using the AC magnetometer.

MF	H_{low}	H_{high}	f_{high}/f_{low}
11.8696	19.3219 kA/m	70 kA/m	5.70241

Table 5.2: Optimized Multiplexing AMF conditions and Multiplexing factor

5.5 Demonstration of Selective Drug Delivery of Magnetoliposomes

To understand the dynamics of magnetoliposomes' drug release, a computer controlled monitoring system has been installed. AMF generators and spectrometers were controlled via VISA in Matlab and optical thermometer was communicated through serial port (RS232). Also edge pass filter was placed in the middle of spectrometer and detecting optical probe in order to screen out the reflected 405nm lights. Also to exclude the effects of external heating or environmental temperature fluctuation, fiber thermometer recorded the sample solutions temperature.

First, the ratio of payload released by alternative magnetic fields and total drug loading have been characterized. Prepared magnetoliposomes were aliquoted to small glass tubes. Holding the magnetoliposome at 65^oC for 5 minutes were assumed to digest all the liposomal encapsulations. Often Triton X or ethanol are used to quan-

	Control	**486kHz 19.32kA/m**	**85.2kHz 70kA/m**	**65^oC for 5min**
Percentage of the payload Fe_3O_4	-	15.07907	-	1.2313465
Percentage of the payload $Co_{0.13}Fe_{2.87}O_4$	-	10.1677	-	2.400192

Table 5.3: Optimized Multiplexing AMF conditions and Multiplexing factor

tify the liposomal drug cargo capacity because they dissolve lipids. However, these chemicals can also react to fluorescent molecules and change the intensity substantially, we used water bath to give heat shock instead, to fully release the dye from the cargo. Fluorescein sodium has been used to characterize, due to their little intensity variation over the temperature. the results are summarized in the Table**??**

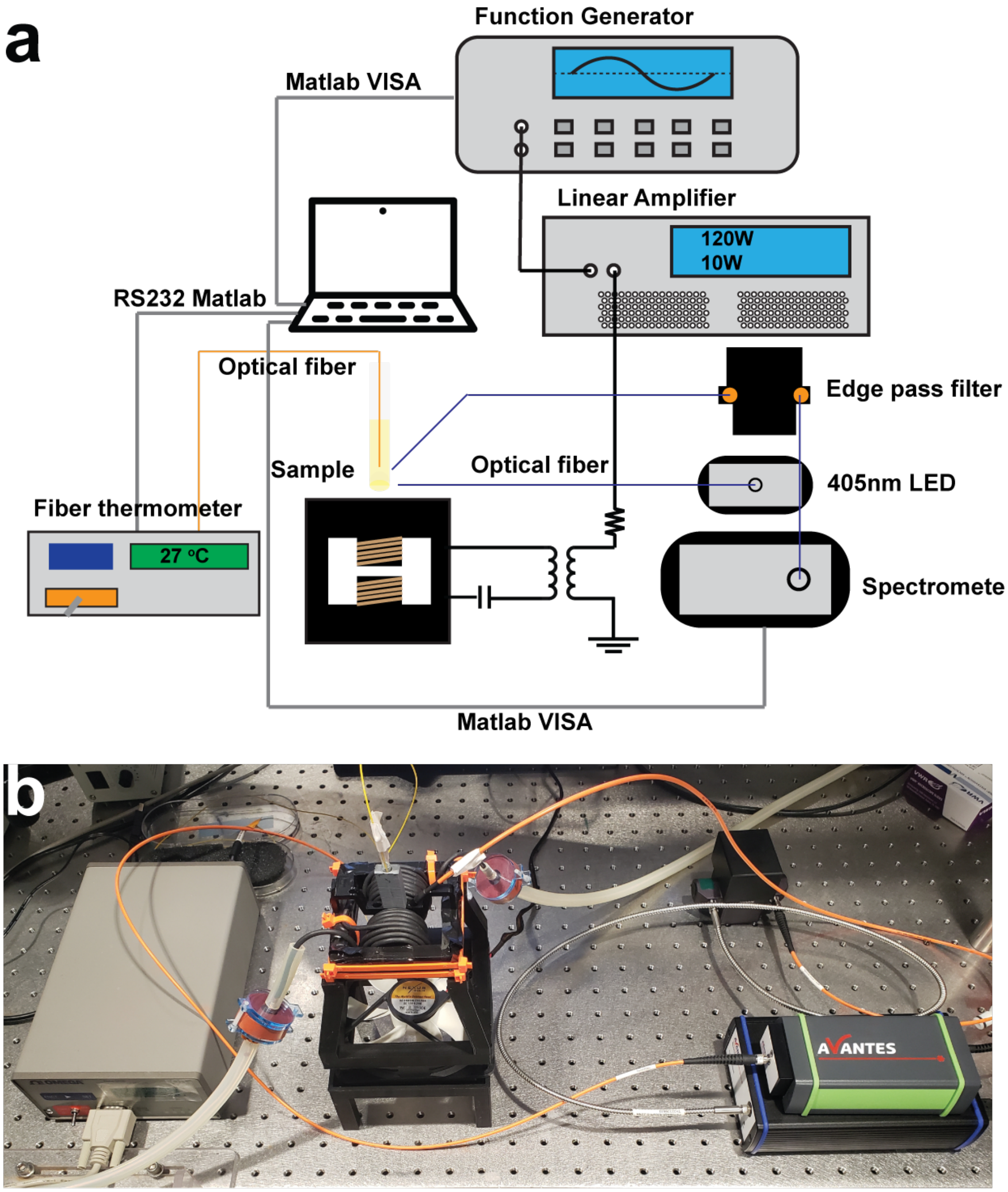

Figure 5-9: **Overview of magnetoliposome monitoring setup** (a) Schematic overview of the monitoring setup. All components are controlled by computer. (b) Actual experimental setup.

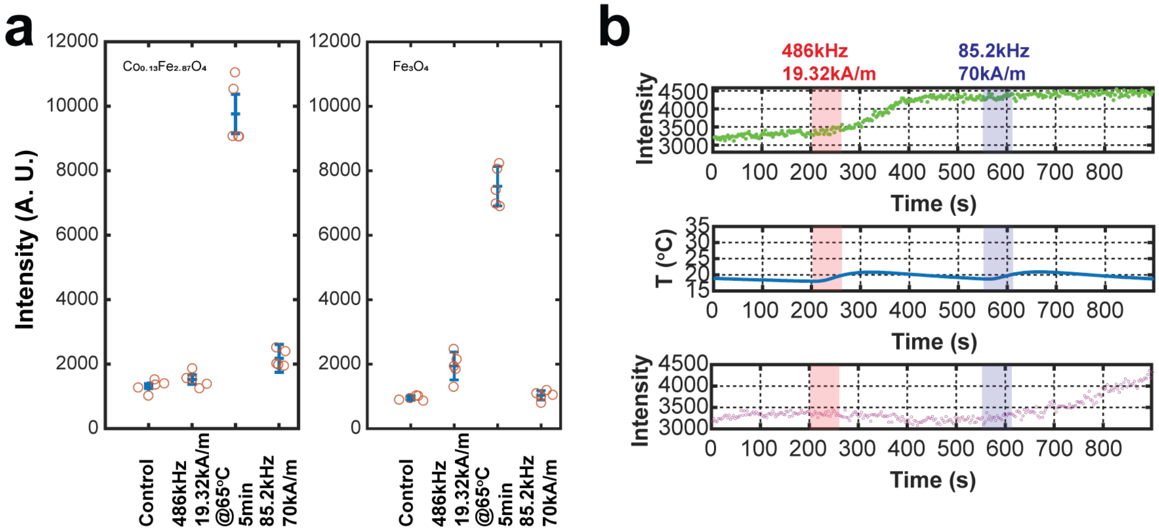

Figure 5-10: **Characterization of** (a) Extrapolated SLP profiles and curve fits of Fe_3O_4 19.653nm and $Co_{0.13}Fe_{2.87}O_4$ 28.980 nm MNPs at 486 kHz (red) and 85.2 kHz (blue). (b) Parametric scanning plot of Multiplexing Factor over field amplitudes (H_1 and H_2) and frequency ratio (f_1/f_2) to determine preliminary AMF conditions.

Chapter 6

Conclusions

6.1 Genetic engineering for ion channel control

Comprehension of neuronal network has proved that its importance is not limited to just the development of therapy for neurodegenerative diseases. A deeper understanding of the brain and the rest of the central nervous system has proved that it connects to interpreting sensation, initiating body movement, and even the origin of our intelligence. The average human brain contains 80 to 90 billion neurons with all kinds of different neurons. Scientist have endeavored to learn about the brain functions with countless various approaches, and thanks to those efforts, some of the basic anatomical circuits of a brain or synaptic interactions have been revealed.

However, there are still lots of undiscovered mysteries due to the enormous complexity of the brain. There were trials to understand brain functionality using electricity, using the fact that neurons convey their signals in electricity. However, the non-selective propagation of electricity across conductive tissue made this method inherently impossible to do completely controlled experiments. Due to this electrical method's limited resolution, it was conceived to be impossible to understand the brain completely.

Elegant advances in genetic engineering, however, opened a new chapter for the brain study. Gene engineering enabled specific cell/neuron type targeting and granted a probing system with cell-type level resolution. Optogenetics, which was first introduced only in 2006 by Deisseroth et al., is now one of the most common, popular, and robust tools to control and monitor the biological functions of cells, tissues, brains, and so on. The photo-sensitive ion channel, Channelrhodopsin 2 (ChR2), which solely responding to blue light, enabled optical control of biological events.[99, 100] Chemogenetics, which uses receptors that explicitly activated by synthetic chemicals, was developed in 1998. Still, the chemognetics at this time couldn't be used in neuroscience because the synthetic ligand caused pharmacological issues in vivo. and adverse problems of the engineered receptors in the absence of the paring ligands.[101] In later, 2011, Designer Receptors Activated by Designer Drugs (DREADD) have been developed and allowed mutated human muscarinic acetylcholine receptors to specifically respond to synthetic Clocapine N-oxide (CNO).[102] The advent of these techniques made unprecedented mysteries in biological circuits accessible.

6.2 Types of Magnetogenetics

Magnetogenetics also came out in this context but with its own advantages. In optogenetics, the blue light should shed directly onto the target receptor. Still, as light is impenetrable deep tissue, it has been limited in studying deeply placed tissues within the body. For chemogenetics, this is not an issue because it's minimally to almost zero invasive. The ligands can be delivered by injection or even drinking water, depending on the ligand type. However, as the receptor responds through binding of ligands, activating and deactivating the receptor couldn't be as rapidly modulated as optogenetics.

Magnetogenetics is a technique that selectively switches the genetically engineered receptors with magnetic field modulation. Unlike any other stimulus such as lights, electric fields, and so on, magnetic fields have negligible coupling to biological matters, allowing the magnetic fields to reach deep into the body without attenuation. As the system relies on the external magnetic field's cue, the receptor's response is also instant when compared to chemogenetics, which awaits the decay of binding ligands. For these reasons, magnetogenetics has been in the spotlight for this certain condition.

6.2.1 Magnetothermal methods

Magnetothermal methods are made of heat-sensitive ion channels such as TRPV1 expressed by genetic engineering and heat-dissipating magnetic nanoparticles that activates the TRPV1. TRPV1 is a well-studied receptor, and thorough researches have unveiled their structure, response conditions, and functionality.[89, 103] Magnetic nanoparticles were synthesized with chemistry and delivered to the TRPV1 expressed cells, neurons, and C. Elegans worms for *in vitro.* demonstrations[39, 104], and later an experiment proved the feasibility of magnetothermal methods in *in vivo.* by injecting synthesized magnetite particles into the mice brain and appplying alternative magnetic fields. [27]

6.2.2 Magnetomechanical methods

As their name, magneto-mechanical methods adopt mechanical forces exerted by magnetic nanoparticles/nanodisks and mechanosensitive ion channels. The translational forces originate from the magnetic field gradient, and the torques were generated in a uniform magnetic field. Those mechanical forces induced deformation or tensions to the membrane nearby mechanosensitive receptors or directly delivered to the receptors. [105, 106, 107]

6.2.3 Magnetic nanocomposites

In some other approaches, researchers decided to deliver the cue to the receptors indirectly. Magnetoliposomes is a nanocomposite made of thermosensitive liposomes encapsulating magnetic nanoparticles as a heat source and chemical ligands, which are designed to release the ligands to the chemogenetic receptors. [38] Also, a polymeric nanocomposite prepared by mixing poly(sebacic acid) with magnetic nanoparticles triggered pH sensitive ion channels by exuding protons produced by magnetothermally hydrolyzed polymers. [108] A study even introduced a non-transgenic approach using a piezoelectric barium titanate ($BaTiO_3$) coated magnetostrictive cobalt ferrite($CoFe_2O_4$) nanocomposite. The nanocomposite functioned as a converter and changed magnetic field input into an electrical stimulus that can trigger voltage-gated ion channels that every neuron has.[109]

6.3 Outlook

In magnetogenetics, there are several different approaches, depending on what type of receptor is a target with a stimulus and whether to deliver the cue directly or indirectly. This thesis has shown that even in the same magnetothermal method category, it can produce selective control. In addition to that, this magnetothermal multiplexed system is orthogonal to other approaches, especially to magneto-mechanical methods. The orthogonality between these two methods can create a synergy, and it can allow even more complex selective modulation for an application that requires multiple targets remotely.

In this work, it showed only bi-modal multiplexed operation. However, this can expand to a tri-modal or even higher multi-modal strategy in theory if there are appropriate magnetic nanoparticles with various coercivity and magnetic field generators to drive those new conditions. To accomplish this multi-mode, it would require significant efforts to balance those multi-paired nanoparticles and AMFs.

In the thesis, two different magnetothermal demonstrations have been introduced. The first demonstration showed selective heating of two other targets spatially separated. This system is applicable to biomedical applications that require two different inputs in separated targets for one behavioral control. One example is the rotating locomotion control of mice. Rotating behavior can be triggered by stimulating a specific spot in one hemisphere of the brain. By targeting two different hemispheres of mice, you can control the mice to make a left or right turn.[110] Another example can be the control of hunting behavior of mice. This research used two different optogenetic inputs to separate mice's hunting behavior to prey pursuit and capture. They could force the mice to only capture the prey by stimulating only reticular formation (PCRt) through central amygdala(CeA), or to only bite the prey by triggering periaqueductal gray (PAG) through CeA.[111]

At the end of this thesis, selective fluorescent dye release in the same place via the multiplexed magnetothermal approach was also demonstrated. This system is transferable to an application aiming for one shared target that responds differently to two specific applied stimuli. This can apply to an application controlling the pain of the mice. A nociceptor is a sensory neuron that sending pain signals to the spinal cord and the brain. By inducing an excitation/inhibition to this nociceptor via optogenetics, this research showed it could increase/decrease the mice's pain and change their retracting threshold lower/higher, which helps the mice avoid threats such as mechanical or thermal stimuli. [112] If the selective drug release is applied to this system, it can unload two different ligands that explicitly respond to excitatory and inhibitory DREADDs channels and control the pain level remotely just by changing alternative magnetic fields. [34]

This thesis started with the motivation to add an additional control knob to the system relying on magnetic nanoparticles' magnetothermal properties. To bring this concept to real, the project has been processed systematically, and started with the theoretical understanding of the origin of the heat dissipation and magnetic materials tuning. I prepared materials candidates' pool and then continued to develop a custom characterization tool for the nanoparticle sets. The characterized properties were then again used to find the optimized operating conditions using newly introduced equations to evaluate multiplexed magnetothermal performance. It proved the system's functionality step by step. It showed the temperature changes of the droplets, then linked that temperature change to the corresponding cellular responses. This system is transferable to any magnetothermal applications. The systematic, step-by-step approach may help other researchers to transplant this into their own magnetothermal practices.

List of Figures

List of Tables

Appendix A

Tables

A.1 Code for numerical calculation using dynamic hysteresis model

A.1.1 Code generates randomly distributed particle sets - Mathematica

This code generates 100 randomly distributed particle sets with given average and standard deviation of the particle. The automatically saved data was imported to Dynamic hysteresis model code for numerical calculation.

```
  numbers
dmean = 16.3;(*in nm*)
dsd = 0.7;(*in nm*)
gaussianSizes[mean_ : dmean, sd_ : dsd, n_ : 10] :=
 RandomVariate[NormalDistribution[mean, sd], n]
randomSizestemp = gaussianSizes[dmean, dsd, 100]
```

```
Export["C:\\Users\\junsang\\Desktop\\20181119 updated particle \
sizes\\d_distribution\\" <> ToString[dmean] <> "_dsd" <>
   ToString[dsd] <> ".dat", randomSizestemp];
```

A.1.2 Code generates Dynamic magnetization - Mathematica

This code numerically calculates dynamic magnetization of 100 particles data generated by 'Code generates randomly distributed particle sets'

```
   numbers
MsFe3O4 = 4.68*10^5;
kB = 1.38064852*10^(-23); (*in J/K*)
K1Fe3O4 = -9*10^3; (*in J/m^3 *)
KsperK1 = 20;
(* Ksurf=K1Fe3O4*KsperK1;(*in J/m^3 *) *)
T = 298;
\[Rho]FeinFe3O4 =
 5.24*10^6 *(3*55.85)/(3*55.85 +
     4*16) (*in g/m^3, Note that we want SLP in terms of W/gFe, so this \
density is adjusted by a factor that assumes stoichiometry *)
\[Alpha]p = 0.1;   (* damping constant *)
\[Gamma] = 1.75*10^11;(* unit:rad/sT, gyromagnetic ratio*)
\[Tau]N0 = (1 + \[Alpha]p^2)/(2*\[Gamma]*\[Alpha]p);
ajdR = 1;

\[Xi]0[16.3, 100]
\[Sigma][16.3]
\[Nu]0[25, 5]

Defining Functions

\[Xi]0[d_, B_] := Pi*B*MsFe3O4*d^3/(6*kB*T)*(10^(-27))*(10^(-3));

\[Nu]0[\[Xi]0_, \[Sigma]_] =
  ajdR*(2/Sqrt[\[Pi]])*\[Sigma]^(3/2)*(1/\[Tau]N0)*\[Xi]0^1/20^3;

\[Xi][t_, \[Xi]0_, \[Omega]_] := \[Xi]0*Cos[\[Omega]*t]
(*This function defines the time dependence of the driving field*)

\[Sigma][d_] :=
  Pi*Abs[K1Fe3O4]*
   d^3/(6*kB*T) (10^(-27));(*+Pi*Abs[Ksurf]*1*d^2/(6*kB*T)(10^(-27));*)
```

```
(*surface spin canting included, 1nm thickness was assumed*)

Pi*Abs[K1Fe3O4]/(6*kB*T) (10^(-27))*(2/3)
\[Sigma][15.1]
8/2.6

0.001379/0.0007635728481287463`

Ea[\[Xi]_, \[Sigma]_] := (\[Sigma] + \[Xi]^2/(4*\[Sigma]) - \[Xi]) (0.5 -
       0.5*Tanh[\[Xi] -
          2*\[Sigma]]) - (\[Sigma] + \[Xi]^2/(4*\[Sigma]) + \[Xi])*(0.5 +
       0.5*Tanh[-\[Xi] -
          2*\[Sigma]]); (*The magnitude of the energy barrier Ea is described \
by this function. Symmtery allows us to say that Eb is the same, but with \
\[Xi] inverted.*)

Ca[\[Xi]_, \[Sigma]_] :=
  NIntegrate[
    Sin[\[Theta]]*Cos[\[Theta]]*
     Exp[-(2*\[Sigma] + \[Xi])/2*\[Theta]^2 + \[Xi]], {\[Theta], 0, Pi/2}]/
   NIntegrate[
    Sin[\[Theta]]*Exp[-(2*\[Sigma] + \[Xi])/2*\[Theta]^2 + \[Xi]], {\[Theta],
     0, Pi/2}];
(*This defines the correction factor for thermal spreading in the A well, \
which is at \[Theta]=0*)

Cb[\[Xi]_, \[Sigma]_] :=
  NIntegrate[
    Sin[\[Theta]]*Cos[\[Theta]]*
     Exp[-(2*\[Sigma] - \[Xi])/2*(\[Theta] - Pi)^2 - \[Xi]], {\[Theta], Pi/2,
     Pi}]/NIntegrate[
    Sin[\[Theta]]*
     Exp[-(2*\[Sigma] - \[Xi])/2*(\[Theta] - Pi)^2 - \[Xi]], {\[Theta], Pi/2,
     Pi}];(*See the comment immediately above. This determines the correction \
factor for thermal spreading at the B well, which is at \[Theta]=Pi.*)

IPLP[A_, fin_] :=
  A*kB*T*fin*10^9*10^22.9;(*The factor of 10^9 is necessary to bring time \
units back to seconds. The factor of 10^22.9 puts the output in fW*)

V[d_] := Pi*
   d^3/6*(10^(-27));(*Output is in m^3 assuming the input is in nm. The shape \
assumed is a shpere*)

SLP[A_, fin_, V_] :=
  A*kB*T*fin*10^9/(V*\[Rho]FeinFe3O4);(*The factor of 10^9 is necessary to \
```

```
bring time units back to seconds*)

Functions that calculate loop area and keep data for drawing loops


LoopArea2[d_, Bin_, fin_, n_] := Catch[
  \[Gamma]A[t_] := \[Nu]0[d]*
    Exp[-Ea[\[Xi][t, \[Xi]0[d, Bin], fin*2*Pi], \[Sigma][d]]];
  \[Gamma]B[t_] := \[Nu]0[d]*
    Exp[-Ea[\[Xi][t, -\[Xi]0[d, Bin], fin*2*Pi], \[Sigma][d]]];
  Pa1[t_] := If[ Pa[t] <=  \[Gamma]A[t]*Pa[t], (Pa[t]),
    If[Pa[t] > \[Gamma]A[t]*Pa[t], (\[Gamma]B[t]*Pb[t] - \[Gamma]A[t]*Pa[t])]];
       Pb1[t_] := If[ Pb[t] <= \[Gamma]B[t]*Pb[t], (Pb[t]),
    If[Pb[t] > \[Gamma]B[t]*Pb[t], (\[Gamma]A[t]*Pa[t] - \[Gamma]B[t]*Pb[t])]];
  sol = NDSolve[{Pa'[t] == Pa1[t], Pb'[t] == Pb1[t], Pa[0] == 0.5,
     Pb[0] == 0.5}, {Pa, Pb}, {t, n/fin, 10^-9}];
  Ms[t_] := -Evaluate[Pa[t] /. sol] + Evaluate[Pb[t] /. sol];
  MMsvs\[Xi] =
   Table[{Bin*Cos[fin*2*Pi*t], Ms[t][[1]]}, {t, (n - 1)/fin, n/fin, 10^-9}];
  area = NIntegrate[
    fin*2*Pi*Bin*Sin[fin*2*Pi*t]*Ms[t], {t, (n - 1)/fin, n/fin},
    PrecisionGoal -> 10^-9];
  Throw[{area[[1]], MMsvs\[Xi]}]
  ]


LoopArea[d_, Bin_, fin_, n_] := Catch[
  \[Gamma]A[
    t_] := \[Nu]0[\[Xi]0[d, Bin], \[Sigma][
      d]]*(Exp[-Ea[\[Xi][t, \[Xi]0[d, Bin], fin*2*Pi], \[Sigma][d]]]);
  \[Gamma]B[
    t_] := \[Nu]0[\[Xi]0[d, Bin], \[Sigma][
      d]]*(Exp[-Ea[\[Xi][t, -\[Xi]0[d, Bin], fin*2*Pi], \[Sigma][d]]]);
  sol = NDSolve[{Pa'[t] == ((\[Gamma]B[t]*Pb[t] - \[Gamma]A[t]*Pa[t])),
     Pb'[t] == ((\[Gamma]A[t]*Pa[t] - \[Gamma]B[t]*Pb[t])), Pa[0] == 0.5,
     Pb[0] == 0.5}, {Pa, Pb}, {t, n/fin, 10^-9}];
  Ms[t_] := -Evaluate[Pa[t] /. sol] + Evaluate[Pb[t] /. sol];
  MMsvs\[Xi] =
   Table[{Bin*Cos[fin*2*Pi*t], Ms[t][[1]]}, {t, (n - 1)/fin, n/fin, 10^-9}];
  area = NIntegrate[
    fin*2*Pi*Bin*Sin[fin*2*Pi*t]*Ms[t], {t, (n - 1)/fin, n/fin},
    PrecisionGoal -> 10^-9];
  Throw[{area[[1]], MMsvs\[Xi]}]
  ]

LoopAreaWithSpreading[d_, Bin_, fin_, n_] := If[1 == 1,
```

```
  Cat = Interpolation[
    Table[{t, Ca[\[Xi][t, \[Xi]0[d, Bin], fin*2*Pi], \[Sigma][d]]}, {t, 0,
      n/fin, 10^-2/fin}]];
  Cbt = Interpolation[
    Table[{t, Cb[\[Xi][t, \[Xi]0[d, Bin], fin*2*Pi], \[Sigma][d]]}, {t, 0,
      n/fin, 10^-2/fin}]];
  Catch[
   \[Gamma]A[t_] := \[Nu]0[\[Xi]0[d, Bin], \[Sigma][d]]*
     Exp[-Ea[\[Xi][t, \[Xi]0[d, Bin], fin*2*Pi], \[Sigma][d]]];
   \[Gamma]B[t_] := \[Nu]0[\[Xi]0[d, Bin], \[Sigma][d]]*
     Exp[-Ea[\[Xi][t, -\[Xi]0[d, Bin], fin*2*Pi], \[Sigma][d]]];
   sol = NDSolve[{Pa'[t] == (\[Gamma]B[t]*Pb[t] - \[Gamma]A[t]*Pa[t]),
      Pb'[t] == (-\[Gamma]B[t]*Pb[t] + \[Gamma]A[t]*Pa[t]), Pa[0] == 0.5,
      Pb[0] == 0.5}, {Pa, Pb}, {t, n/fin, 10^-9}];
   Ms[t_] := Evaluate[Pa[t] /. sol]*Cbt[t] + Cat[t]*Evaluate[Pb[t] /. sol];
   MMsvs\[Xi] =
    Table[{-Bin*Cos[fin*2*Pi*t], -Ms[t][[1]]}, {t, (n - 1)/fin, n/fin, 10^-9}];
   area = NIntegrate[
     fin*2*Pi*Bin*Sin[fin*2*Pi*t]*Ms[t], {t, (n - 1)/fin, n/fin},
     PrecisionGoal -> 10^-9];
   Throw[{area[[1]], MMsvs\[Xi]}]
   ]]

(*BfieldRange=Range[5,100,10];*)
dmean2 = 16.3;
dsd = 0.7;
randomSizes =
  Import["C:\\Users\\junsang\\Desktop\\20181119 updated particle \
sizes\\d_distribution\\" <> ToString[dmean2] <> "_dsd" <> ToString[dsd] <>
    ".dat", "List"];

(*randomSizes={29.5};*)
BfieldRange2 = {1, 2, 5, 10, 15, 20, 25, 30, 50, 70, 100};
(*BfieldRange2={100};*)
For[i = 1, i < Length[BfieldRange2] + 1, i++,
 HysloopWS =
  Map[LoopAreaWithSpreading[#, BfieldRange2[[i]], 75*1000, 5][[2]] &,
   randomSizes];
 averageHysloop =
  Thread[{HysloopWS[[1, All, 1]],
    Mean /@ Transpose[HysloopWS[[All, All, 2]]]}];
 (*HysloopAreaWS=Map[LoopAreaWithSpreading[dmean2,#,75*1000,5][[1]]&,\
BfieldRange2];*)
 HysloopNameWS = Map[ToString[#] <> "mT With spreading" &, BfieldRange2[[i]]];
 CreateDirectory[
  "C:\\Users\\junsang\\Desktop\\20181119 updated particle \
```

```
sizes\\distributed100_dmean" <> ToString[dmean2]];
 Export["C:\\Users\\junsang\\Desktop\\20181119 updated particle \
sizes\\distributed100_dmean" <> ToString[dmean2] <> "\\" <>
   ToString[BfieldRange2[[i]]] <> "mT_raw100_dmean" <> ToString[dmean2] <>
   "_dsd_" <> ToString[dsd] <> "_Hysloop.xlsx", HysloopWS];
 Export["C:\\Users\\junsang\\Desktop\\20181119 updated particle \
sizes\\distributed100_dmean" <> ToString[dmean2] <> "\\" <>
   ToString[BfieldRange2[[i]]] <> "mT_raw100_dmean" <> ToString[dmean2] <>
   "_dsd_" <> ToString[dsd] <> "_Hysloop.dat", HysloopWS];
 Export["C:\\Users\\junsang\\Desktop\\20181119 updated particle \
sizes\\distributed100_dmean" <> ToString[dmean2] <> "\\" <>
   ToString[BfieldRange2[[i]]] <> "mT_Averaged_dmean" <> ToString[dmean2] <>
   "_dsd_" <> ToString[dsd] <> "_Hysloop.xlsx", averageHysloop];
 ]
ListLinePlot[averageHysloop, PlotLegends -> HysloopNameWS,
 AxesLabel -> {"B(mT)", "M/Ms"}]
ListLinePlot[Thread[{BfieldRange2, HysloopAreaWS}],
 PlotLegends -> HysloopNameWS, AxesLabel -> {"B(mT)", "M/Ms"}]



(*BfieldRange=Range[5,100,10];*)
dmean2 = 29.5;
dsd = 2.3;
randomSizes =
  Import["C:\\Users\\junsang\\Desktop\\20181119 updated particle \
sizes\\d_distribution\\" <> ToString[dmean2] <> "_dsd" <> ToString[dsd] <>
    ".dat", "List"];

(*randomSizes={29.5};*)
BfieldRange2 = {1, 2, 5, 10, 15, 20, 25, 30, 50, 70, 100};
(*BfieldRange2={100};*)
For[i = 1, i < Length[BfieldRange2] + 1, i++,
 HysloopWS =
  Map[LoopAreaWithSpreading[#, BfieldRange2[[i]], 75*1000, 5][[2]] &,
   randomSizes];
 averageHysloop =
  Thread[{HysloopWS[[1, All, 1]],
    Mean /@ Transpose[HysloopWS[[All, All, 2]]]}];
 (*HysloopAreaWS=Map[LoopAreaWithSpreading[dmean2,#,75*1000,5][[1]]&,\
BfieldRange2];*)
 HysloopNameWS = Map[ToString[#] <> "mT With spreading" &, BfieldRange2[[i]]];
 CreateDirectory[
  "C:\\Users\\junsang\\Desktop\\20181119 updated particle \
sizes\\distributed100_dmean" <> ToString[dmean2]];
 Export["C:\\Users\\junsang\\Desktop\\20181119 updated particle \
sizes\\distributed100_dmean" <> ToString[dmean2] <> "\\" <>
```

```
   ToString[BfieldRange2[[i]]] <> "mT_raw100_dmean" <> ToString[dmean2] <>
   "_dsd_" <> ToString[dsd] <> "_Hysloop.xlsx", HysloopWS];
 Export["C:\\Users\\junsang\\Desktop\\20181119 updated particle \
sizes\\distributed100_dmean" <> ToString[dmean2] <> "\\" <>
   ToString[BfieldRange2[[i]]] <> "mT_raw100_dmean" <> ToString[dmean2] <>
   "_dsd_" <> ToString[dsd] <> "_Hysloop.dat", HysloopWS];
 Export["C:\\Users\\junsang\\Desktop\\20181119 updated particle \
sizes\\distributed100_dmean" <> ToString[dmean2] <> "\\" <>
   ToString[BfieldRange2[[i]]] <> "mT_Averaged_dmean" <> ToString[dmean2] <>
   "_dsd_" <> ToString[dsd] <> "_Hysloop.xlsx", averageHysloop];
 ]
ListLinePlot[averageHysloop, PlotLegends -> HysloopNameWS,
 AxesLabel -> {"B(mT)", "M/Ms"}]
ListLinePlot[Thread[{BfieldRange2, HysloopAreaWS}],
 PlotLegends -> HysloopNameWS, AxesLabel -> {"B(mT)", "M/Ms"}]



(*BfieldRange=Range[5,100,10];*)
dmean2 = 20.5;
dsd = 1.3;
randomSizes =
  Import["C:\\Users\\junsang\\Desktop\\20181119 updated particle \
sizes\\d_distribution\\" <> ToString[dmean2] <> "_dsd" <> ToString[dsd] <>
    ".dat", "List"];

(*randomSizes={29.5};*)
BfieldRange2 = {1, 2, 5, 10, 15, 20, 25, 30, 50, 70, 100};
(*BfieldRange2={100};*)
For[i = 1, i < Length[BfieldRange2] + 1, i++,
 HysloopWS =
  Map[LoopAreaWithSpreading[#, BfieldRange2[[i]], 75*1000, 5][[2]] &,
   randomSizes];
 averageHysloop =
  Thread[{HysloopWS[[1, All, 1]],
    Mean /@ Transpose[HysloopWS[[All, All, 2]]]}];
 (*HysloopAreaWS=Map[LoopAreaWithSpreading[dmean2,#,75*1000,5][[1]]&,\
BfieldRange2];*)
 HysloopNameWS = Map[ToString[#] <> "mT With spreading" &, BfieldRange2[[i]]];
 CreateDirectory[
  "C:\\Users\\junsang\\Desktop\\20181119 updated particle \
sizes\\distributed100_dmean" <> ToString[dmean2]];
 Export["C:\\Users\\junsang\\Desktop\\20181119 updated particle \
sizes\\distributed100_dmean" <> ToString[dmean2] <> "\\" <>
   ToString[BfieldRange2[[i]]] <> "mT_raw100_dmean" <> ToString[dmean2] <>
   "_dsd_" <> ToString[dsd] <> "_Hysloop.xlsx", HysloopWS];
 Export["C:\\Users\\junsang\\Desktop\\20181119 updated particle \
```

```
sizes\\distributed100_dmean" <> ToString[dmean2] <> "\\" <>
   ToString[BfieldRange2[[i]]] <> "mT_raw100_dmean" <> ToString[dmean2] <>
   "_dsd_" <> ToString[dsd] <> "_Hysloop.dat", HysloopWS];
 Export["C:\\Users\\junsang\\Desktop\\20181119 updated particle \
sizes\\distributed100_dmean" <> ToString[dmean2] <> "\\" <>
   ToString[BfieldRange2[[i]]] <> "mT_Averaged_dmean" <> ToString[dmean2] <>
   "_dsd_" <> ToString[dsd] <> "_Hysloop.xlsx", averageHysloop];
 ]
ListLinePlot[averageHysloop, PlotLegends -> HysloopNameWS,
 AxesLabel -> {"B(mT)", "M/Ms"}]
ListLinePlot[Thread[{BfieldRange2, HysloopAreaWS}],
 PlotLegends -> HysloopNameWS, AxesLabel -> {"B(mT)", "M/Ms"}]



(*BfieldRange=Range[5,100,10];*)
dmean2 = 24.7;
dsd = 1.4;
randomSizes =
  Import["C:\\Users\\junsang\\Desktop\\20181119 updated particle \
sizes\\d_distribution\\" <> ToString[dmean2] <> "_dsd" <> ToString[dsd] <>
    ".dat", "List"];

(*randomSizes={29.5};*)
BfieldRange2 = {1, 2, 5, 10, 15, 20, 25, 30, 50, 70, 100};
(*BfieldRange2={100};*)
For[i = 1, i < Length[BfieldRange2] + 1, i++,
 HysloopWS =
  Map[LoopAreaWithSpreading[#, BfieldRange2[[i]], 75*1000, 5][[2]] &,
   randomSizes];
 averageHysloop =
  Thread[{HysloopWS[[1, All, 1]],
    Mean /@ Transpose[HysloopWS[[All, All, 2]]]}];
 (*HysloopAreaWS=Map[LoopAreaWithSpreading[dmean2,#,75*1000,5][[1]]&,\
BfieldRange2];*)
 HysloopNameWS = Map[ToString[#] <> "mT With spreading" &, BfieldRange2[[i]]];
 CreateDirectory[
  "C:\\Users\\junsang\\Desktop\\20181119 updated particle \
sizes\\distributed100_dmean" <> ToString[dmean2]];
 Export["C:\\Users\\junsang\\Desktop\\20181119 updated particle \
sizes\\distributed100_dmean" <> ToString[dmean2] <> "\\" <>
   ToString[BfieldRange2[[i]]] <> "mT_raw100_dmean" <> ToString[dmean2] <>
   "_dsd_" <> ToString[dsd] <> "_Hysloop.xlsx", HysloopWS];
 Export["C:\\Users\\junsang\\Desktop\\20181119 updated particle \
sizes\\distributed100_dmean" <> ToString[dmean2] <> "\\" <>
   ToString[BfieldRange2[[i]]] <> "mT_raw100_dmean" <> ToString[dmean2] <>
   "_dsd_" <> ToString[dsd] <> "_Hysloop.dat", HysloopWS];
```

```
 Export["C:\\Users\\junsang\\Desktop\\20181119 updated particle \
sizes\\distributed100_dmean" <> ToString[dmean2] <> "\\" <>
   ToString[BfieldRange2[[i]]] <> "mT_Averaged_dmean" <> ToString[dmean2] <>
   "_dsd_" <> ToString[dsd] <> "_Hysloop.xlsx", averageHysloop];
 ]
ListLinePlot[averageHysloop, PlotLegends -> HysloopNameWS,
 AxesLabel -> {"B(mT)", "M/Ms"}]
ListLinePlot[Thread[{BfieldRange2, HysloopAreaWS}],
 PlotLegends -> HysloopNameWS, AxesLabel -> {"B(mT)", "M/Ms"}]
```

```
<< JLink`;
InstallJava[];
ReinstallJava[JVMArguments -> "-Xmx6144m"]
```

```
CreateDirectory[
 "C:\\Users\\Junsang Moon\\Dropbox\\Experiment\\Multiplexing\\Junsang\\d \
dependant\\180820Xi0power-1_dmean" <> ToString[dmean2]]
Export["C:\\Users\\Junsang \
Moon\\Dropbox\\Experiment\\Multiplexing\\Junsang\\d \
dependant\\180820Xi0power-1_dmean" <> ToString[dmean2] <> "\\v0_" <>
  ToString[v0] <> "_KsperK1_" <> ToString[KsperK1] <> "_dmean" <>
  ToString[dmean2] <> "_dsd_" <> ToString[dsd] <> "_Hysloop.xlsx", HysloopWS]
```

```
Clear["Global'*"]
```

```
listv0 = Map[\[Nu]0[\[Xi]0[dmean2, #], \[Sigma][dmean2]] &, BfieldRange2]
```

```
HysloopAreaWS
```

```
Length[BfieldRange2]
```

```
BfieldRange2[[4]]
```

AC magnetometer

numbers

```
clear
clear all
clc
close
close all

% Close connections to any previously connected instruments

% Read measure files
prompt = 'What frequency will you operated? (in kHz)';
freq = input(prompt);
freq = freq*1000; %change into Hz

prompt = 'What is your sample name?(Sample_holdertype)';
rawName = input(prompt,'s');



%Choose folder to save
Address_save = uigetdir('C:\Users\junsang\Dropbox\Experiment\MATLAB coding for function generator and oscilloscope','Choose folder to save your figure');

%Choose file to load
[OpList, PathName] = uigetfile({'*xls';'*csv'},'Select Operational condition list *.csv or *xls');
[Condition ,junk1] = xlsread(fullfile(PathName, OpList));
Frequency = Condition(1,2);
Frequency = Frequency*1000; %kHz to Hz
List_inputVpp = Condition(3:numel(Condition(:,1)-2),1);
List_Chan3 = Condition(3:numel(Condition(:,2)-2),2);
List_Chan4 = Condition(3:numel(Condition(:,3)-2),3);
%mV to V
List_inputVpp = List_inputVpp/1000;
List_Chan3 = List_Chan3/1000;
List_Chan4 = List_Chan4/1000;


newobjs = instrfind;
if ~isempty(newobjs);
    fclose(newobjs);
    delete(newobjs);
end
```

```
% Copy the VISA address from Agilent Connection Expert and paste it in
% place of the one below

% MSOX3054A:
%scope = visa('agilent','USB0::0x0957::0x179A::MY51450668::0::INSTR');
% DSO-x 3014T
scope = visa('agilent','USB0::0x2A8D::0x1768::MY55280423::0::INSTR');

% MSO7104B:
% scope = visa('agilent','USB0::0x0957::0x175D::MY50340735::0::INSTR');
% 3321A
fgen = visa('agilent','USB0::0x0957::0x1507::MY48007672::0::INSTR');
fopen(scope); % Connect to the scope

fopen(fgen); % Connect to the function generator

fprintf(scope,'*idn?'); % Get scope's ID string
idn = scanstr(scope,','); % Read response and parse into an array

% Determine which channel to digitize.  Select the lowest-numbered channel
% that is on.

fprintf(scope,':chan1:disp?'); % Is channel 1 turned on?
chan1 = scanstr(scope,'%d8');
chan1 = chan1{1,1};
fprintf(scope,':chan2:disp?'); % Is channel 2 turned on?
chan2 = scanstr(scope,'%d8');
chan2 = chan2{1,1};
fprintf(scope,':chan3:disp?'); % Is channel 3 turned on?
chan3 = scanstr(scope,'%d8');
chan3 = chan3{1,1};
fprintf(scope,':chan4:disp?'); % Is channel 4 turned on?
chan4 = scanstr(scope,'%d8');
chan4 = chan4{1,1};

if chan1 == 1
    chanToDigitize = 'chan1';
elseif chan2 == 1
    chanToDigitize = 'chan2';
elseif chan3 == 1
    chanToDigitize = 'chan3';
elseif chan4 == 1
    chanToDigitize = 'chan4';
else
    delete(scope);
```

```
    clear scope;
    clear fid  screenImage outFile
    clear all
    error('At least one channel must be turned on!')
end

chanToDigitize = 'chan3'; %Set chan3 for Sample probe
chanToDigitize2 = 'chan4'; %Set chan4 for Field proble
for ii = 1:numel(List_inputVpp);

fprintf(scope,[':wav:sour' ' ' chanToDigitize]); % Select the channel with
                                                 % the data we want

fprintf(scope, sprintf(':CHANnel3:SCALe %g', List_Chan3(ii)));
fprintf(fgen, sprintf(':APPLy:SINusoid %g,%g', freq, List_inputVpp(ii)));
pause (0.5);
% fprintf(scope,':wav:poin:mode max'); % Make it possible to get the max
                                      % number of points
 fprintf(scope,':wav:poin max'); % Set the max number of points
%fprintf(scope,':wav:poin 5000'); % Set an explicit number of points
fprintf(scope,':wav:uns 0'); % Use unsigned integer format for the raw data
fprintf(scope,':wav:form word'); % 16-bit WORD format is the most accurate
                                 % binary format
fprintf(scope,':wav:byt lsbf'); % Set the byte order to Least Significant
                                % Byte First
fprintf(scope,':wav:pre?'); % The preamble contains the scaling data we
                            % need to convert the raw data into voltage
                            % values
pre = scanstr(scope,','); % Read the comma-separated preamble values into
                          % an array
fprintf(scope,':tim:rang?'); % Query the range of time displayed on screen
timeRange = scanstr(scope,',','%f');
fprintf(scope,':tim:pos?'); % Query the time value at the reference point
                            % default is center screen)
timePosition = scanstr(scope,',','%f');

fprintf(scope,[':',chanToDigitize,':rang?']); % Query the range of voltage
                                              % displayed on screen
chRange = scanstr(scope,',','%f');

fprintf(scope,[':',chanToDigitize,':offs?']); % Query the voltage value at
                                              % the reference point
                                              % (default is 0V)
chOffset = scanstr(scope,',','%f');

% Scale the plot to match the scope's display
```

```
plotStartTime = timePosition - timeRange/2;
plotEndTime = timePosition + timeRange/2;
plotLowVoltage = chOffset - chRange/2;
plotHighVoltage = chOffset + chRange/2;

if iscell(pre) % The preamble contains alphanumeric values, resulting in a
               % cell array instead of a matrix
    pre = pre(1:10); % Disregards all preamble except for first 10 values
    pre = cell2mat(pre); % Converts preamble from cell to matrix
end

fclose(scope); % Temporarily close scope connection to set buffer size
scope.inputbuffersize = pre(3)*13; % Sets the buffer size to slightly
                                   % larger than the incoming waveform data
fopen(scope); % Reconnect to scope

fprintf(scope,':wav:data?'); % Query instrument for waveform data
wavin = binblockread(scope,'int16');% Reads the waveform data into an array
fread(scope,1); % Read the termination character since binblockread does
                % not do this

% Check for scope errors and display for the user

fprintf(scope,':syst:err?');
disp(scanstr(scope,','))

wavData = ((wavin-pre(10))*pre(8))+pre(9); % Scales the amplitude

time = (0:1:(length(wavData)-1))'; % Creates time axis
time = ((time-pre(7))*pre(5))+pre(6); % Scales times
%fprintf(fgen, ':OUTPUT:STATe 0'); %Field is off - changed to keep turned
%on 20171122

%Data set 1 (Field probe) plot
subplot(1, 2, 1);
plot(time,wavData,'-b') %Plot waveform points
axis([plotStartTime plotEndTime plotLowVoltage plotHighVoltage]);

% Set plot title and axis labels

title([idn(1),idn(2),...
    strcat(chanToDigitize,' data'),strcat(int2str(pre(3)),' points'),]);
xlabel('Time (s)') % Set axis labels
ylabel('Voltage (V)')
```

```
%%%%%%%%%%%%%%%%%%%%%%%%%%%%%%%%%%%%%%%%%%%%%%%%%%%%%%%%%%%%%%%%%%%%%%
fprintf(scope,[':wav:sour' ' ' chanToDigitize2]); % Select the channel with
                                                   % the data we want
fprintf(scope, sprintf(':CHANnel4:SCALe %g', List_Chan4(ii)));
%fprintf(fgen, sprintf(':APPLy:SINusoid %g,%g', freq, List_inputVpp(ii)));
%20171122 it's already turned on
% fprintf(scope,':wav:poin:mode max'); % Make it possible to get the max
                                        % number of points
 fprintf(scope,':wav:poin max'); % Set the max number of points
%fprintf(scope,':wav:poin 5000'); % Set an explicit number of points
fprintf(scope,':wav:uns 0'); % Use unsigned integer format for the raw data
fprintf(scope,':wav:form word'); % 16-bit WORD format is the most accurate
                                  % binary format
fprintf(scope,':wav:byt lsbf'); % Set the byte order to Least Significant
                                 % Byte First
fprintf(scope,':wav:pre?'); % The preamble contains the scaling data we
                            % need to convert the raw data into voltage
                            % values
pre2 = scanstr(scope,','); % Read the comma-separated preamble values into
                          % an array
fprintf(scope,':tim:rang?'); % Query the range of time displayed on screen
timeRange2 = scanstr(scope,',','%f');
fprintf(scope,':tim:pos?'); % Query the time value at the reference point
                            % default is center screen)
timePosition2 = scanstr(scope,',','%f');

fprintf(scope,[':',chanToDigitize2,':rang?']); % Query the range of voltage
                                               % displayed on screen
chRange2 = scanstr(scope,',','%f');

fprintf(scope,[':',chanToDigitize2,':offs?']); % Query the voltage value at
                                               % the reference point
                                               % (default is 0V)
chOffset2 = scanstr(scope,',','%f');

% Scale the plot to match the scope's display


plotStartTime2 = timePosition2 - timeRange2/2;
plotEndTime2 = timePosition2 + timeRange2/2;
plotLowVoltage2 = chOffset2 - chRange2/2;
plotHighVoltage2 = chOffset2 + chRange2/2;


if iscell(pre2) % The preamble contains alphanumeric values, resulting in a
                % cell array instead of a matrix
    pre2 = pre2(1:10); % Disregards all preamble except for first 10 values
    pre2 = cell2mat(pre2); % Converts preamble from cell to matrix
```

```
end

fclose(scope); % Temporarily close scope connection to set buffer size
scope.inputbuffersize = pre2(3)*13; % Sets the buffer size to slightly
                                    % larger than the incoming waveform data
fopen(scope); % Reconnect to scope

fprintf(scope,':wav:data?'); % Query instrument for waveform data
wavin2 = binblockread(scope,'int16');% Reads the waveform data into an array
fread(scope,1); % Read the termination character since binblockread does
                % not do this

% Check for scope errors and display for the user

fprintf(scope,':syst:err?');
disp(scanstr(scope,','))

wavData2 = ((wavin2-pre2(10))*pre2(8))+pre2(9); % Scales the amplitude

time2 = (0:1:(length(wavData2)-1))'; % Creates time axis
time2 = ((time2-pre2(7))*pre2(5))+pre2(6); % Scales times
fprintf(fgen, ':OUTPUT:STATe 0'); %Field is off
%%%%%%%%%%%%%%%%%%%%


%Data set 2 (Sample probe) plot
subplot(1, 2, 2);
plot(time2,wavData2,'-b') %Plot waveform points
axis([plotStartTime2 plotEndTime2 plotLowVoltage2 plotHighVoltage2]);

% Set plot title and axis labels

title([idn(1),idn(2),...
    strcat(chanToDigitize2,' data'),strcat(int2str(pre2(3)),' points'),]);

% Save the data to a CSV file (CAUTION: Generates errors for large
% waveforms. Recommended for smaller waveforms, e.g. 32K and below.)

% xlswrite('C:\Users\Junsang Moon\Desktop\InfiniiVision.xls',[time,wavData]);

% Delete objects and clear them
FigName = strcat(rawName,'_input_',num2str(List_inputVpp(ii)),'V_Chan3_',num2str(List_Chan3(ii)),'
    V_Chan4_',num2str(List_Chan4(ii)),'V.fig');
savefig(fullfile(Address_save,FigName));
pause(4);
close gcf
```

```
Ampchan3(ii)=0.29*max(abs(wavData));
Ampchan4(ii)=0.29*max(abs(wavData2));

end
freq = freq/1000; %(Hz to kHz)
Ampchan3 = Ampchan3'*1000; %(V to mV) and transpose
Ampchan4 = Ampchan4'*1000;
List_inputVpp = List_inputVpp*1000;

col_header1_1={'Frequency'}; %Column header (1,1) A1
col_header1_3={'kHz'}; %Column header (1,3) C1

col_header2={'inputVpp(mV)','CH3(mV)','CH4(mV)'}; %Column header 2nd
xlsname = strcat('ACM_condition_',rawName,'.xls');
outname = fullfile(Address_save, xlsname);

xlswrite(outname, Frequency, 'Sheet1', 'B1');
xlswrite(outname, List_inputVpp, 'Sheet1', 'A3');
xlswrite(outname, Ampchan3, 'Sheet1', 'B3');
xlswrite(outname, Ampchan4, 'Sheet1', 'C3');
xlswrite(outname, col_header1_1, 'Sheet1', 'A1');
xlswrite(outname, col_header1_3, 'Sheet1', 'C1');
xlswrite(outname, col_header2, 'Sheet1', 'A2');


fclose(fgen);
delete(fgen);
delete(scope);



clear
clear all
clc
close
close all

%clear scope;
%clear fid  screenImage outFile
%clear all
```

Bibliography

[1]

[2] Ritchie Chen, Andres Canales, and Polina Anikeeva. Neural recording and modulation technologies. *Nature Reviews Materials*, 2(2):16093, 2017.

[3] Matthew I. Brier and Jonathan S. Dordick. Remote activation of cellular signaling. *Science*, 368(6494):936–937, 2020.

[4] Seongjun Park, Gabriel Loke, Yoel Fink, and Polina Anikeeva. Flexible fiber-based optoelectronics for neural interfaces. *Chem. Soc. Rev.*, 48:1826–1852, 2019.

[5] Dae-Hyeong Kim, Roozbeh Ghaffari, Nanshu Lu, and John A. Rogers. Flexible and stretchable electronics for biointegrated devices. *Annual Review of Biomedical Engineering*, 14(1):113–128, 2012. PMID: 22524391.

[6] Sung Il Park, Gunchul Shin, Jordan G. McCall, Ream Al-Hasani, Aaron Norris, Li Xia, Daniel S. Brenner, Kyung Nim Noh, Sang Yun Bang, Dionnet L. Bhatti, Kyung-In Jang, Seung-Kyun Kang, Aaron D. Mickle, Gregory Dussor, Theodore J. Price, Robert W. Gereau, Michael R. Bruchas, and John A. Rogers. Stretchable multichannel antennas in soft wireless optoelectronic implants for optogenetics. *Proceedings of the National Academy of Sciences*, 113(50):E8169–E8177, 2016.

[7] Elon Musk and . An integrated brain-machine interface platform with thousands of channels. *bioRxiv*, 2019.

[8] Dena Shahriari, Dekel Rosenfeld, and Polina Anikeeva. Emerging frontier of peripheral nerve and organ interfaces. *Neuron*, 108(2):270 – 285, 2020.

[9] Lisa A. Urry. *Campbell Biology (11th Edition)*. Pearson, oct 2016.

[10] Janet L Stringer. *Basic concepts in pharmacology: What you need to know for each drug class*. McGraw Hill Professional, 2017.

[11] Erhu Cao, Julio F. Cordero-Morales, Beiying Liu, Feng Qin, and David Julius.

TRPV1 Channels Are Intrinsically Heat Sensitive and Negatively Regulated by Phosphoinositide Lipids. *Neuron*, 2013.

[12] A S French and P H Torkkeli. Mechanoreceptors. pages 689–695. Academic Press, Oxford, 2009.

[13] Yuan Ren Cheng, Bo Yang Jiang, and Chih Cheng Chen. Acid-sensing ion channels: Dual function proteins for chemo-sensing and mechano-sensing. *Journal of Biomedical Science*, 25(1):1–14, 2018.

[14] John A Wemmie, Rebecca J Taugher, and Collin J Kreple. Acid-sensing ion channels in pain and disease. *Nature reviews. Neuroscience*, 14(7):461–471, jul 2013.

[15] Franziska Schneider, Christiane Grimm, and Peter Hegemann. Biophysics of Channelrhodopsin. *Annual Review of Biophysics*, 44:167–186, 2015.

[16] Christopher Engelhard, Igor Chizhov, Friedrich Siebert, and Martin Engelhard. Microbial Halorhodopsins: Light-Driven Chloride Pumps. *Chemical Reviews*, 118(21):10629–10645, 2018.

[17] Edward A Dennis, Sue Goo Rhee, M Motasim Billah, and Yusuf A Hannun. Role of phospholipases in generating lipid second messengers in signal transduction1. *The FASEB Journal*, 5(7):2068–2077, apr 1991.

[18] Martin R McAinsh, Colin Brownlee, and Alistair M Hetherington. Calcium ions as second messengers in guard cell signal transduction. *Physiologia Plantarum*, 100(1):16–29, may 1997.

[19] Jean M Lauder. Neurotransmitters as growth regulatory signals: role of receptors and second messengers. *Trends in Neurosciences*, 16(6):233–240, 1993.

[20] Diane C. Slusarski and Francisco Pelegri. Calcium signaling in vertebrate embryonic patterning and morphogenesis. *Developmental Biology*, 307(1):1–13, 2007.

[21] Jinhao Gao, Hongwei Gu, and Bing Xu. Multifunctional Magnetic Nanoparticles: Design, Synthesis, and Biomedical Applications. *Accounts of Chemical Research*, 42(8):1097–1107, aug 2009.

[22] Nohyun Lee, Dongwon Yoo, Daishun Ling, Mi Hyeon Cho, Taeghwan Hyeon, and Jinwoo Cheon. Iron Oxide Based Nanoparticles for Multimodal Imaging and Magnetoresponsive Therapy. *Chemical Reviews*, 115(19):10637–10689, oct 2015.

[23] Daishun Ling, Nohyun Lee, and Taeghwan Hyeon. Chemical Synthesis and Assembly of Uniformly Sized Iron Oxide Nanoparticles for Medical Applications.

Accounts of Chemical Research, 48(5):1276–1285, may 2015.

[24] Gang Liu, Jinhao Gao, Hua Ai, and Xiaoyuan Chen. Applications and Potential Toxicity of Magnetic Iron Oxide Nanoparticles. *Small*, 9(9-10):1533–1545, may 2013.

[25] P A Bottomley and E R Andrew. RF magnetic field penetration, phase shift and power dissipation in biological tissue: implications for NMR imaging. *Physics in Medicine and Biology*, 23(4):630–643, 1978.

[26] J H Young, M T Wang, and I A Brezovich. Frequency/depth-penetration considerations in hyperthermia by magnetically induced currents, 1980.

[27] Ritchie Chen, Gabriela Romero, Michael G Christiansen, Alan Mohr, and Polina Anikeeva. Wireless magnetothermal deep brain stimulation. *Science*, 347(6229):1477 LP – 1480, mar 2015.

[28] Nohyun Lee and Taeghwan Hyeon. Designed synthesis of uniformly sized iron oxide nanoparticles for efficient magnetic resonance imaging contrast agents. *Chemical Society Reviews*, 41(7):2575–2589, 2012.

[29] Hong Yu Yang, Yi Li, and Doo Sung Lee. Multifunctional and Stimuli-Responsive Magnetic Nanoparticle-Based Delivery Systems for Biomedical Applications. *Advanced Therapeutics*, 1(2):1800011, jun 2018.

[30] Arathi Nair, Prashant Chauhan, Bhaskar Saha, and Katharina F. Kubatzky. Conceptual Evolution of Cell Signaling. *International Journal of Molecular Sciences*, 20(13):3292, jul 2019.

[31] Danielle S. Bassett and Michael S. Gazzaniga. Understanding complexity in the human brain. *Trends in Cognitive Sciences*, 15(5):200–209, may 2011.

[32] Chris Towne and Kimberly R. Thompson. Overview on Research and Clinical Applications of Optogenetics. *Current Protocols in Pharmacology*, 75(1), dec 2016.

[33] Anthony C. Bishop, Kavita Shah, Yi Liu, Laurie Witucki, Chi-yun Kung, and Kevan M. Shokat. Design of allele-specific inhibitors to probe protein kinase signaling. *Current Biology*, 8(5):257–266, feb 1998.

[34] Bryan L. Roth. DREADDs for Neuroscientists. *Neuron*, 89(4):683–694, feb 2016.

[35] Edward S Boyden, Feng Zhang, Ernst Bamberg, Georg Nagel, and Karl Deisseroth. Millisecond-timescale, genetically targeted optical control of neural activity. *Nature Neuroscience*, 8(9):1263–1268, sep 2005.

[36] Lief Fenno, Ofer Yizhar, and Karl Deisseroth. The Development and Application of Optogenetics. *Annual Review of Neuroscience*, 34(1):389–412, jun 2011.

[37] Jia Liu, Yoon Seok Kim, Claire E Richardson, Ariane Tom, Charu Ramakrishnan, Fikri Birey, Toru Katsumata, Shucheng Chen, Cheng Wang, Xiao Wang, Lydia-Marie Joubert, Yuanwen Jiang, Huiliang Wang, Lief E Fenno, Jeffrey B.-H. Tok, Sergiu P Pașca, Kang Shen, Zhenan Bao, and Karl Deisseroth. Genetically targeted chemical assembly of functional materials in living cells, tissues, and animals. *Science*, 367(6484):1372 LP – 1376, mar 2020.

[38] Siyuan Rao, Ritchie Chen, Ava A LaRocca, Michael G Christiansen, Alexander W Senko, Cindy H Shi, Po-Han Chiang, Georgios Varnavides, Jian Xue, Yang Zhou, Seongjun Park, Ruihua Ding, Junsang Moon, Guoping Feng, and Polina Anikeeva. Remotely controlled chemomagnetic modulation of targeted neural circuits. *Nature Nanotechnology*, 14(10):967–973, 2019.

[39] Heng Huang, Savas Delikanli, Hao Zeng, Denise M Ferkey, and Arnd Pralle. Remote control of ion channels and neurons through magnetic-field heating of nanoparticles. *Nat Nano*, 5(8):602–606, aug 2010.

[40] Tapan K Jain, Maram K Reddy, Marco A Morales, Diandra L Leslie-Pelecky, and Vinod Labhasetwar. Biodistribution, Clearance, and Biocompatibility of Iron Oxide Magnetic Nanoparticles in Rats. *Molecular Pharmaceutics*, 5(2):316–327, apr 2008.

[41] R C O'Handley. *Modern Magnetic Materials: Principles and Applications*. Wiley, 1999.

[42] Alexandra Navrotsky and O J Kleppa. The thermodynamics of cation distributions in simple spinels. *Journal of Inorganic and nuclear Chemistry*, 29(11):2701–2714, 1967.

[43] R F Pearson. The Magnetocrystalline Anisotropy of Cobalt-Substituted Manganese Ferrite. *Proceedings of the Physical Society*, 74(5):505–512, 1959.

[44] J. C. Slonczewski. Origin of magnetic anisotropy in cobalt-substituted magnetite. *Phys. Rev.*, 110:1341–1348, Jun 1958.

[45] R.E. E Rosensweig. Heating magnetic fluid with alternating magnetic field. *Journal of Magnetism and Magnetic Materials*, 252(0):370–374, 2002.

[46] J. Carrey, B. Mehdaoui, and M. Respaud. Simple models for dynamic hysteresis loop calculations of magnetic single-domain nanoparticles: Application to magnetic hyperthermia optimization. *Journal of Applied Physics*, 109(8), 2011.

[47] Jean Paul Fortin, Claire Wilhelm, Jacques Servais, Christine Ménager,

Jean Claude Bacri, and Florence Gazeau. Size-sorted anionic iron oxide nanomagnets as colloidal mediators for magnetic hyperthermia. *Journal of the American Chemical Society*, 129(9):2628–2635, 2007.

[48] Jae-Hyun Lee, Jung-Tak Jang, Jin-Sil Choi, Seung Ho Moon, Seung-Hyun Noh, Jin-Gyu Ji-Wook Jin-Gyu Ji-Wook Kim, Jin-Gyu Ji-Wook Jin-Gyu Ji-Wook Kim, Il-Sun Kim, Kook In Park, and Jinwoo Cheon. Exchange-coupled magnetic nanoparticles for efficient heat induction. *Nature nanotechnology*, 6(7):418–422, 2011.

[49] Jing Ju Lu, Huei Li Huang, and I. Klik. Field orientations and sweep rate effects on magnetic switching of Stoner-Wohlfarth particles. *Journal of Applied Physics*, 76(3):1726–1732, 1994.

[50] J Garcıa-Otero, a.J Garcıa-Bastida, and J Rivas. Influence of temperature on the coercive field of non-interacting fine magnetic particles. *Journal of Magnetism and Magnetic Materials*, 189(3):377–383, 1998.

[51] N. A. Usov and Yu B. Grebenshchikov. Hysteresis loops of an assembly of superparamagnetic nanoparticles with uniaxial anisotropy. *Journal of Applied Physics*, 106(2), 2009.

[52] M. G. Christiansen, A. W. Senko, R. Chen, G. Romero, and P. Anikeeva. Magnetically multiplexed heating of single domain nanoparticles. *Applied Physics Letters*, 104(21):213103, may 2014.

[53] V M Chakka, B Altuncevahir, Z Q Jin, Y Li, and J P Liu. Magnetic nanoparticles produced by surfactant-assisted ball milling. *Journal of Applied Physics*, 99(8):08E912, apr 2006.

[54] M Carmen Bautista, Oscar Bomati-Miguel, María del Puerto Morales, Carlos J Serna, and Sabino Veintemillas-Verdaguer. Surface characterisation of dextran-coated iron oxide nanoparticles prepared by laser pyrolysis and coprecipitation. *Journal of Magnetism and Magnetic Materials*, 293(1):20–27, 2005.

[55] Jin Xie, Kai Chen, and Xiaoyuan Chen. Production, Modification and Bio-Applications of Magnetic Nanoparticles Gestated by Magnetotactic Bacteria. *Nano research*, 2(4):261–278, apr 2009.

[56] Ji-Won Moon, Claudia J Rawn, Adam J Rondinone, Lonnie J Love, Yul Roh, S Michelle Everett, Robert J Lauf, and Tommy J Phelps. Large-scale production of magnetic nanoparticles using bacterial fermentation. *Journal of Industrial Microbiology & Biotechnology*, 37(10):1023–1031, 2010.

[57] Saima Gul, Sher Bahadar Khan, Inayat Ur Rehman, Murad Ali Khan, and M I Khan. A Comprehensive Review of Magnetic Nanomaterials Modern Day

Theranostics. *Frontiers in Materials*, 6:179, 2019.

[58] Nohyun Lee and Taeghwan Hyeon. Designed synthesis of uniformly sized iron oxide nanoparticles for efficient magnetic resonance imaging contrast agents. *Chem. Soc. Rev.*, 41(7):2575–2589, 2012.

[59] Sheva Naahidi, Mousa Jafari, Faramarz Edalat, Kevin Raymond, Ali Khademhosseini, and P Chen. Biocompatibility of engineered nanoparticles for drug delivery. *Journal of Controlled Release*, 166(2):182–194, 2013.

[60] A Gessner, R Waicz, A Lieske, B.-R Paulke, K Mäder, and R H Müller. Nanoparticles with decreasing surface hydrophobicities: influence on plasma protein adsorption. *International Journal of Pharmaceutics*, 196(2):245–249, 2000.

[61] Fumiaki Shima, Takami Akagi, Tomofumi Uto, and Mitsuru Akashi. Manipulating the antigen-specific immune response by the hydrophobicity of amphiphilic poly(γ-glutamic acid) nanoparticles. *Biomaterials*, 34(37):9709–9716, 2013.

[62] Apiwat Chompoosor, Krishnendu Saha, Partha S Ghosh, Dylan J Macarthy, Oscar R Miranda, Zheng-Jiang Zhu, Kathleen F Arcaro, and Vincent M Rotello. The role of surface functionality on acute cytotoxicity, ROS generation and DNA damage by cationic gold nanoparticles. *Small (Weinheim an der Bergstrasse, Germany)*, 6(20):2246–2249, oct 2010.

[63] Zheng-Jiang Zhu, Tamara Posati, Daniel F Moyano, Rui Tang, Bo Yan, Richard W Vachet, and Vincent M Rotello. The interplay of monolayer structure and serum protein interactions on the cellular uptake of gold nanoparticles. *Small (Weinheim an der Bergstrasse, Germany)*, 8(17):2659–2663, sep 2012.

[64] Daniel F Moyano, Meir Goldsmith, David J Solfiell, Dalit Landesman-Milo, Oscar R Miranda, Dan Peer, and Vincent M Rotello. Nanoparticle Hydrophobicity Dictates Immune Response. *Journal of the American Chemical Society*, 134(9):3965–3967, mar 2012.

[65] Krishnendu Saha, Daniel F Moyano, and Vincent M Rotello. Protein coronas suppress the hemolytic activity of hydrophilic and hydrophobic nanoparticles. *Materials Horizons*, 1(1):102–105, 2014.

[66] Jianfeng Zeng, Lihong Jing, Yi Hou, Mingxia Jiao, Ruirui Qiao, Qiaojuan Jia, Chunyan Liu, Fang Fang, Hao Lei, and Mingyuan Gao. Anchoring Group Effects of Surface Ligands on Magnetic Properties of Fe3O4 Nanoparticles: Towards High Performance MRI Contrast Agents. *Advanced Materials*, 26(17):2694–2698, may 2014.

[67] W W Yu, E Chang, J C Falkner, J Zhang, a M Al-Somali, C M Sayes, J Johns,

R Drezek, and V L Colvin. Forming biocompatible & nonaggregated nanocrystal FeNP in water using amphiphilic polymer. *J. Am. Chem. Soc.*, 129(10):2871–2879, 2007.

[68] Susana I C J Palma, Marzia Marciello, Alexandra Carvalho, Sabino Veintemillas-Verdaguer, Maria del Puerto Morales, and Ana C A Roque. Effects of phase transfer ligands on monodisperse iron oxide magnetic nanoparticles. *Journal of Colloid and Interface Science*, 437:147–155, 2015.

[69] Guido Ketteler, Werner Weiss, Wolfgang Ranke, and Robert Schlögl. Bulk and surface phases of iron oxides in an oxygen and water atmosphere at low pressure. *Physical Chemistry Chemical Physics*, 3(6):1114–1122, 2001.

[70] E. Garaio, J. M. Collantes, F. Plazaola, J. A. Garcia, and I. Castellanos-Rubio. A multifrequency eletromagnetic applicator with an integrated AC magnetometer for magnetic hyperthermia experiments. *Measurement Science and Technology*, 25(11):115702, nov 2014.

[71] E. Garaio, J. M. Collantes, F. Plazaola, J. A. Garcia, and I. Castellanos-Rubio. A multifrequency eletromagnetic applicator with an integrated AC magnetometer for magnetic hyperthermia experiments. *Measurement Science and Technology*, 25(11), 2014.

[72] Philip Lenox, L Kenyon Plummer, Partha Paul, James E Hutchison, Albrecht Jander, and Pallavi Dhagat. High-Frequency and High-Field Hysteresis Loop Tracer for Magnetic Nanoparticle Characterization. *IEEE Magnetics Letters*, 9:1–5, 2018.

[73] Clément Guibert, Jérôme Fresnais, Véronique Peyre, and Vincent Dupuis. Magnetic fluid hyperthermia probed by both calorimetric and dynamic hysteresis measurements. *Journal of Magnetism and Magnetic Materials*, 421:384–392, 2017.

[74] V. Connord, B. Mehdaoui, R. P. Tan, J. Carrey, and M. Respaud. An air-cooled Litz wire coil for measuring the high frequency hysteresis loops of magnetic samples - A useful setup for magnetic hyperthermia applications. *Review of Scientific Instruments*, 85(9), 2014.

[75] T Nakamura, T Tsutaoka, and K Hatakeyama. Frequency dispersion of permeability in ferrite composite materials. *Journal of Magnetism and Magnetic Materials*, 138(3):319–328, 1994.

[76] Michael G. Christiansen, Christina M. Howe, David C. Bono, David J. Perreault, and Polina Anikeeva. Practical methods for generating alternating magnetic fields for biomedical research. *Review of Scientific Instruments*, 88(8), 2017.

[77] Robert J Deissler, Yong Wu, and Michael A Martens. Dependence of Brownian and Néel relaxation times on magnetic field strength. *Medical Physics*, 41(1):12301, jan 2014.

[78] Daniel B Reeves and John B Weaver. Nonlinear simulations to optimize magnetic nanoparticle hyperthermia. *Applied Physics Letters*, 104(10):102403, mar 2014.

[79] J Leliaert, A Coene, G Crevecoeur, A Vansteenkiste, D Eberbeck, F Wiekhorst, B Van Waeyenberge, and L Dupré. Regarding the Néel relaxation time constant in magnetorelaxometry. *Journal of Applied Physics*, 116(16):163914, oct 2014.

[80] Eric R Muir, Qiang Shen, and Timothy Q Duong. Cerebral blood flow MRI in mice using the cardiac-spin-labeling technique. *Magnetic resonance in medicine*, 60(3):744–748, sep 2008.

[81] Dongwon Yoo, Heeyeong Jeong, Seung-Hyun Noh, Jae-Hyun Lee, and Jinwoo Cheon. Magnetically Triggered Dual Functional Nanoparticles for Resistance-Free Apoptotic Hyperthermia. *Angewandte Chemie International Edition*, 52(49):13047–13051, dec 2013.

[82] Rudolf Hergt and Silvio Dutz. Magnetic particle hyperthermia-biophysical limitations of a visionary tumour therapy. *Journal of Magnetism and Magnetic Materials*, 311(1 SPEC. ISS.):187–192, 2007.

[83] Qing Song and Z John Zhang. Correlation between SpinOrbital Coupling and the Superparamagnetic Properties in Magnetite and Cobalt Ferrite Spinel Nanocrystals. *The Journal of Physical Chemistry B*, 110(23):11205–11209, jun 2006.

[84] J. C. Slonczewski. Origin of magnetic anisotropy in cobalt-substituted magnetite. *Physical Review*, 110(6):1341–1348, 1958.

[85] Masashi Tachiki. Origin of the Magnetic Anisotropy Energy of Cobalt Ferrite. *Progress of Theoretical Physics*, 23(6):1055–1072, jun 1960.

[86] Erhu Cao, Julio F. Cordero-Morales, Beiying Liu, Feng Qin, and David Julius. TRPV1 Channels Are Intrinsically Heat Sensitive and Negatively Regulated by Phosphoinositide Lipids. *Neuron*, 77(4):667–679, 2013.

[87] Ritchie Chen, Michael G Christiansen, and Polina Anikeeva. Maximizing hysteretic losses in magnetic ferrite nanoparticles via model-driven synthesis and materials optimization. *ACS Nano*, 7(10):8990–9000, 2013.

[88] H Kobayashi, K Ueda, A Tomitaka, T Yamada, and Y Takemura. Self-Heating Property of Magnetite Nanoparticles Dispersed in Solution. *IEEE Transactions on Magnetics*, 47(10):4151–4154, 2011.

[89] Michael J Caterina, Mark A Schumacher, Makoto Tominaga, Tobias A Rosen, Jon D Levine, and David Julius. The capsaicin receptor: a heat-activated ion channel in the pain pathway. *Nature*, 389:816, oct 1997.

[90] Gabriela Romero, Michael G Christiansen, Ligia Stocche Barbosa, Francisco Garcia, and Polina Anikeeva. Localized Excitation of Neural Activity via Rapid Magnetothermal Drug Release. *Advanced Functional Materials*, 26(35):6471–6478, 2016.

[91] Simone Schuerle, Jaideep S Dudani, Michael G Christiansen, Polina Anikeeva, and Sangeeta N Bhatia. Magnetically Actuated Protease Sensors for in Vivo Tumor Profiling. *Nano Letters*, 16(10):6303–6310, oct 2016.

[92] Alberto Curcio, Aurore Van de Walle, Aida Serrano, Sandra Preveral, Christine Péchoux, David Pignol, Nicolas Menguy, Christopher T Lefevre, Ana Espinosa, and Claire Wilhelm. Transformation Cycle of Magnetosomes in Human Stem Cells: From Degradation to Biosynthesis of Magnetic Nanoparticles Anew. *ACS Nano*, 14(2):1406–1417, feb 2020.

[93] Jessica F Liu, Nishant Neel, Phillip Dang, Max Lamb, Jaime McKenna, Lauren Rodgers, Brian Litt, Zhiliang Cheng, Andrew Tsourkas, and David Issadore. Radiofrequency-Triggered Drug Release from Nanoliposomes with Millimeter-Scale Resolution Using a Superimposed Static Gating Field. *Small*, 14(44):1802563, nov 2018.

[94] Yechezkel Barenholz. Doxil®–the first FDA-approved nano-drug: lessons learned. *Journal of controlled release : official journal of the Controlled Release Society*, 160(2):117–134, jun 2012.

[95] Lisa Sercombe, Tejaswi Veerati, Fatemeh Moheimani, Sherry Y Wu, Anil K Sood, and Susan Hua. Advances and Challenges of Liposome Assisted Drug Delivery. *Frontiers in pharmacology*, 6:286, dec 2015.

[96] DmitryV. Volodkin, AndreG. Skirtach, and Helmuth Möhwald. Near-IR Remote Release from Assemblies of Liposomes and Nanoparticles. *Angewandte Chemie International Edition*, 48(10):1807–1809, feb 2009.

[97] Behzad Shirmardi Shaghasemi, Mudassar Mumtaz Virk, and Erik Reimhult. Optimization of Magneto-thermally Controlled Release Kinetics by Tuning of Magnetoliposome Composition and Structure. *Scientific Reports*, 7(1):7474, 2017.

[98] George Podaru, Saralyn Ogden, Amanda Baxter, Tej Shrestha, Shenqiang Ren, Prem Thapa, Raj Kumar Dani, Hongwang Wang, Matthew T Basel, Punit Prakash, Stefan H Bossmann, and Viktor Chikan. Pulsed Magnetic Field Induced Fast Drug Release from Magneto Liposomes via Ultrasound Generation.

The Journal of Physical Chemistry B, 118(40):11715–11722, oct 2014.

[99] Karl Deisseroth, Guoping Feng, Ania K Majewska, Gero Miesenböck, Alice Ting, and Mark J Schnitzer. Next-Generation Optical Technologies for Illuminating Genetically Targeted Brain Circuits. *The Journal of Neuroscience*, 26(41):10380 LP – 10386, oct 2006.

[100] Karl Deisseroth. Optogenetics. *Nature Methods*, 8(1):26–29, 2011.

[101] P Coward, H G Wada, M S Falk, S D Chan, F Meng, H Akil, and B R Conklin. Controlling signaling with a specifically designed Gi-coupled receptor. *Proceedings of the National Academy of Sciences of the United States of America*, 95(1):352–357, jan 1998.

[102] Christopher J Magnus, Peter H Lee, Deniz Atasoy, Helen H Su, Loren L Looger, and Scott M Sternson. Chemical and genetic engineering of selective ion channel-ligand interactions. *Science (New York, N.Y.)*, 333(6047):1292–1296, sep 2011.

[103] Maofu Liao, Erhu Cao, David Julius, and Yifan Cheng. Structure of the TRPV1 ion channel determined by electron cryo-microscopy. *Nature*, 504(7478):107–112, 2013.

[104] Ritchie Chen, Michael G. Christiansen, Alexandra Sourakov, Alan Mohr, Yuri Matsumoto, Satoshi Okada, Alan Jasanoff, and Polina Anikeeva. High-Performance Ferrite Nanoparticles through Nonaqueous Redox Phase Tuning. *Nano Letters*, 16(2):1345–1351, feb 2016.

[105] Jae-Hyun Lee, Ji-wook Kim, Michael Levy, Albert Kao, Seung-hyun Noh, Dolores Bozovic, and Jinwoo Cheon. Magnetic Nanoparticles for Ultrafast Mechanical Control of Inner Ear Hair Cells. *ACS Nano*, 8(7):6590–6598, jul 2014.

[106] Steven Hughes, Stuart McBain, Jon Dobson, and Alicia J El Haj. Selective activation of mechanosensitive ion channels using magnetic particles. *Journal of The Royal Society Interface*, 5(25):855–863, aug 2008.

[107] Danijela Gregurec, Alexander W Senko, Andrey Chuvilin, Pooja D Reddy, Ashwin Sankararaman, Dekel Rosenfeld, Po-Han Chiang, Francisco Garcia, Ian Tafel, Georgios Varnavides, Eugenia Ciocan, and Polina Anikeeva. Magnetic Vortex Nanodiscs Enable Remote Magnetomechanical Neural Stimulation. *ACS Nano*, 14(7):8036–8045, jul 2020.

[108] Jimin Park, Anthony Tabet, Junsang Moon, Po-Han Chiang, Florian Koehler, Atharva Sahasrabudhe, and Polina Anikeeva. Remotely Controlled Proton Generation for Neuromodulation. *Nano Letters*, aug 2020.

[109] Rakesh Guduru, Ping Liang, J Hong, Alexandra Rodzinski, Ali Hadjikhani,

Jeffrey Horstmyer, Ernest Levister, and Sakhrat Khizroev. Magnetoelectric 'spin' on stimulating the brain. *Nanomedicine*, 10(13):2051–2061, may 2015.

[110] Viviana Gradinaru, Kimberly R Thompson, Feng Zhang, Murtaza Mogri, Kenneth Kay, M Bret Schneider, and Karl Deisseroth. Targeting and Readout Strategies for Fast Optical Neural Control In Vitro and In Vivo. *The Journal of Neuroscience*, 27(52):14231 LP – 14238, dec 2007.

[111] Wenfei Han, Luis A Tellez, Miguel J Rangel Jr., Simone C Motta, Xiaobing Zhang, Isaac O Perez, Newton S Canteras, Sara J Shammah-Lagnado, Anthony N van den Pol, and Ivan E de Araujo. Integrated Control of Predatory Hunting by the Central Nucleus of the Amygdala. *Cell*, 168(1):311–324.e18, jan 2017.

[112] Shrivats Mohan Iyer, Kate L Montgomery, Chris Towne, Soo Yeun Lee, Charu Ramakrishnan, Karl Deisseroth, and Scott L Delp. Virally mediated optogenetic excitation and inhibition of pain in freely moving nontransgenic mice. *Nature Biotechnology*, 32(3):274–278, 2014.